

Proposal for JLab PAC47

Strange Hadron Spectroscopy with Secondary K_L Beam in Hall D

Experimental Support:

S. Adhikari³⁵, M. J. Amarian (**Contact Person, Spokesperson**)³⁵, A. Austregesilo³⁹,
M. Baalouch⁴², M. Bashkanov (**Spokesperson**)⁵⁷, V. Baturin³⁵, V. V. Berdnikov^{52,32}, T. Black⁵⁵,
W. Boeglin³⁰, W. J. Briscoe⁵³, V. D. Burkert³³, E. Chudakov³³, P. L. Cole³, O. Cortes-Becerra⁵³,
V. Crede⁴⁵, D. Day¹², P. Degtyarenko³³, S. Dobbs (**Spokesperson**)⁴⁵, G. Dodge³⁵,
A. G. Dolgolenko³¹, H. Egiyan³³, P. Eugenio⁴⁵, S. Fegan⁵¹, A. Filippi⁴⁹, S. Furletov³³, L. Gan⁵⁵,
A. Gasparyan²⁰, G. Gavalian³³, D. I. Glazier¹⁹, V. S. Goryachev³¹, L. Guo³⁰, A. Hayrapetyan¹⁸,
A. Hurley⁵⁴, C. E. Hyde³⁵, I. Illari⁵¹, D. G. Ireland¹⁹, K. Joo⁴⁴, V. Kakoyan⁵⁶, G. Kalicy⁵²,
M. Kamel³⁰, C. D. Keith³³, C. W. Kim⁵¹, G. Krafft³³, S. Kuhn³⁵, S. Kuleshov⁴³, A. B. Laptev²⁸,
I. Larin¹, D. Lawrence³³, D. I. Lersch⁴⁵, W. Li⁵⁴, V. E. Lyubovitskij^{49,46,47,51}, D. Mack³³,
D. M. Manley²⁷, H. Marukyan⁵⁶, V. Matveev³¹, M. McCaughan³³, B. McKinnon¹⁹,
C. A. Meyer³⁹, F. Nerling^{16,14}, G. Niculescu²², A. Ostrovidov⁴⁵, Z. Papandreou⁴⁰, K. Park³³,
E. Pasyuk³³, L. Pentchev³³, W. Phelps⁵³, J. W. Price¹¹, J. Reinhold³⁰,
J. Ritman (**Spokesperson**)^{7,25}, D. Romanov³², C. Salgado³⁴, T. Satogata³³, A. M. Schertz⁵⁴,
S. Schadmand²⁵, D. I. Sober⁵², A. Somov³³, S. Somov³², J. R. Stevens (**Spokesperson**)⁵⁴,
I. I. Strakovsky (**Spokesperson**)⁵³, V. Tarasov³¹, S. Taylor³³, A. Thiel¹⁹, D. Watts⁵⁷,
L. Weinstein³⁵, D. Werthmüller⁵⁷, T. Whitlatch³³, N. Wickramaarachchi³⁵, B. Wojtsekhowski³³,
N. Zachariou⁵⁷, J. Zhang¹²

Theoretical Support:

A. V. Anisovich^{8,15}, A. Bazavov¹³, R. Bellwied²⁴, V. Bernard³⁸, G. Colangelo⁴, A. Cieply⁴¹,
M. Döring⁵³, S. Eidelman^{36,37}, A. Eskandarian⁵³, J. Goity^{33,21}, H. Haberzettl⁵³,
M. Hadžimehmedović⁵⁰, R. L. Jaffe¹⁰, B. Z. Kopeliovich⁵¹, H. Leutwyler⁴, M. Mai⁵³,
V. Mathieu²⁹, M. Matveev¹⁵, U.-G. Meißner^{8,26}, V. Mokeev³³, C. Morningstar³⁹,
B. Moussallam³⁸, K. Nakayama², V. Nikonov^{8,15}, Y. Oh⁵⁹, R. Omerović⁵⁰, H. Osmanović⁵⁰,
J. R. Pelaez²⁹, A. Pilloni³³, D. Richards³³, D.-O. Riska²³, A. Rodas²⁹, J. Ruiz de Elvira⁴,
H.-Y. Ryu⁹, E. Santopinto¹⁷, A. V. Sarantsev^{8,15}, J. Stahov⁵⁰, A. Švarc⁵⁸, A. Szczepaniak^{6,33},
R. L. Workman⁵⁰, B. Zou⁵,

¹ University of Massachusetts, Amherst, MA 01003, USA

² University of Georgia (UGA), Athens, GA 30602, USA

³ Lamar University, Beaumont, TX 77710, USA

⁴ University of Bern, CH-3012 Bern, Switzerland

- ⁵ Institute of Theoretical Physics, CAS, Beijing 100190, People's Republic of China
- ⁶ Indiana University (IU), Bloomington, IN 47403, USA
- ⁷ Institut für Experimentalphysik I - Ruhr-Universität, Bochum 44780, Germany
- ⁸ Helmholtz-Institut für Strahlen- und Kernphysik, Universität Bonn, Bonn 53115, Germany
- ⁹ Pusan National University, Busan 46241, Republic of Korea
- ¹⁰ Massachusetts Institute of Technology (MIT), Cambridge, MA 02139, USA
- ¹¹ California State University, Dominguez Hills, Carson, CA 90747, USA
- ¹² University of Virginia (UVa), Charlottesville, VA 22904, USA
- ¹³ Michigan State University (MSU), East Lansing, MI 48824, USA
- ¹⁴ Goethe University Frankfurt, Frankfurt 60323, Germany
- ¹⁵ National Research Centre "Kurchatov Institute", Petersburg Nuclear Physics Institute (PNPI), Gatchina 188300, Russia
- ¹⁶ GSI Helmholtzzentrum für Schwerionenforschung GmbH, Darmstadt 64291, Germany
- ¹⁷ I.N.F.N. Sezione di Genova, Genova 16146, Italy
- ¹⁸ Justus Liebig-University of Giessen, Giessen 35392, Germany
- ¹⁹ University of Glasgow, Glasgow G12 8QQ, UK
- ²⁰ North Carolina A&T State University (N.C.A&T), Greensboro, NC 27411, USA
- ²¹ Hampton University, Hampton, VA 23668, USA
- ²² James Madison University (JMU), Harrisonburg, VA 22807, USA
- ²³ Finnish Society of Science and Letters, Helsinki 00130, Finland
- ²⁴ University of Houston, Houston, TX 77204, USA
- ²⁵ Institute für Kernphysik & Jülich Center für Hadron Physics, Jülich 52425, Germany
- ²⁶ Institute for Advanced Simulation, Institut für Kernphysik and Jülich Center for Hadron Physics, Jülich 52425, Germany
- ²⁷ Kent State University (KSU), Kent, OH 44242, USA
- ²⁸ Los Alamos National Laboratory (LANL), Los Alamos, NM 87545, USA
- ²⁹ Universidad Complutense de Madrid, 28040 Madrid, Spain
- ³⁰ Florida International University (FIU), Miami, FL 33199, USA
- ³¹ National Research Centre "Kurchatov Institute", Institute for Theoretical and Experimental Physics (ITEP), Moscow 117218, Russia
- ³² National Research Nuclear University Moscow Engineering Physics Institute (MEPhI), Moscow 115409, Russia
- ³³ Thomas Jefferson National Accelerator Facility (JLab), Newport News, VA 23606, USA
- ³⁴ Norfolk State University, Norfolk, VA 23504, USA
- ³⁵ Old Dominion University (ODU), Norfolk, VA 23529, USA
- ³⁶ Budker Institute of Nuclear Physics SB RAS, Novosibirsk 630090, Russia
- ³⁷ Novosibirsk State University, Novosibirsk 630090, Russia
- ³⁸ Universite Paris-Sud 11, 91400 Orsay, France
- ³⁹ Carnegie Mellon University (CMU), Pittsburgh, PA 15213, USA
- ⁴⁰ University of Regina (UR), Regina, SA S4S 0A2, Canada
- ⁴¹ Nuclear Physics Institute, Rez 250 68, Czech Republic
- ⁴² C.E.A. L'energie Atomique Et Aux Energies Alternatives, 91190 Saclay, France
- ⁴³ Universidad Andres Bello, Sazie 2212, Piso 7, Santiago, Chile
- ⁴⁴ University of Connecticut (UConn), Storrs, CO 06269, USA
- ⁴⁵ Florida State University (FSU), Tallahassee, FL 32306, USA

- ⁴⁶ Tomsk State University, Tomsk 634050, Russia
⁴⁷ Tomsk Polytechnic University, Tomsk 634050, Russia
⁴⁸ I.N.F.N. Sezione di Torino, Torino 10125, Italy
⁴⁹ Institute of Theoretical Physics, University of Tübingen, Tübingen 72076, Germany
⁵⁰ University of Tuzla, Tuzla 75000, Bosnia and Herzegovina
⁵¹ Universidad Técnica Federico Santa María, Casilla 110-V Valparaíso, Chile
⁵² The Catholic University of America (CUA), Washington, DC 20064, USA
⁵³ The George Washington University (GW), Washington, DC 20052, USA
⁵⁴ College of William and Mary (W&M), Williamsburg, VA 23185, USA
⁵⁵ University of North Carolina at Wilmington (UNCW), Wilmington, NC 28403, USA
⁵⁶ A. I. Alikhanian National Science Laboratory (Yerevan Physics Institute (YerPhi)), Yerevan 0036, Armenia
⁵⁷ University of York, Heslington, York YO10 5DD, UK
⁵⁸ Rudjer Bošković Institute, Zagreb 10002, Croatia
⁵⁹ Kyungpook National University, Daegu 41566, Republic of Korea

(The KLF Collaboration)



Abstract

We propose to create a secondary beam of neutral kaons in Hall D at Jefferson Lab to be used with the GlueX experimental setup for strange hadron spectroscopy. The superior CEBAF electron beam will enable a flux on the order of $1 \times 10^4 K_L/s$, which exceeds the flux of that previously attained at SLAC by three orders of magnitude. It will allow a broad range of measurements that will correspondingly improve the statistics of earlier data obtained on a hydrogen target likewise by three orders of magnitude. The use of a deuteron target will provide first measurements ever with neutral kaons on neutrons.

The experiment will measure both differential cross sections and self-analyzed polarizations of the produced Λ , Σ , Ξ , and Ω hyperons using the GlueX detector at the Jefferson Lab Hall D. The measurements will span $\text{CM } \cos \theta$ from -0.95 to 0.95 in the range $W = 1490 \text{ MeV}$ to 2500 MeV . The new data will significantly constrain the partial wave analyses and reduce model-dependent uncertainties in the extraction of the properties and pole positions of the strange hyperon resonances, and establish the orbitally excited multiplets in the spectra of the Ξ and Ω hyperons. Comparison with the corresponding multiplets in the spectra of the charm and bottom hyperons will illuminate the approach to heavy flavor symmetry and the accuracy of QCD based calculations.

The proposed facility will have a defining impact in the strange meson sector through measurements of the final state $K\pi$ system up to 2 GeV invariant mass. This will allow the determination of pole positions and widths of all $K^*(K\pi)$ P-wave resonances and finally settle the question of the existence or nonexistence of scalar meson $\kappa(800)$ and subsequently of the low-lying scalar nonet in general.

Contents

1	Executive Summary	1
2	Scope of the Proposal	2
3	The Case for Strange Hyperon Spectroscopy	4
3.1	Heavy Quark Symmetry and the Hyperons	4
3.2	Strange Hadrons from the Lattice	4
3.3	Highlights of the KLF Hyperon Program	6
4	Phenomenology / Partial-Wave Analysis	7
4.1	The $\Lambda(1405)1/2^- - \Lambda(1520)3/2^-$ Doublet	8
4.2	The Low-Lying Positive-Parity Resonances	9
4.3	The Negative-Parity Hyperon Resonances	9
4.4	KN and $\bar{K}N$ Final States	10
4.5	$\pi\Lambda$ Final States	10
4.6	$\pi\Sigma$ Final States	10
4.7	$K\Xi$ Final States	11
4.8	Excited $S = -2$ and $S = -3$ baryons	11
4.9	Theory for “Neutron” Target Measurements	12
4.10	Summary for PWA	14
5	πK Scattering Amplitudes and Strange Meson Resonances	15
5.1	Note on the Strange Meson Spectrum	15
5.2	Strange Exotics	15
5.3	Status of πK Scattering Measurements	17
5.4	Theory	18
5.5	Highlights of the Strange Meson Program	20
6	Proposed KL Beam Facility	21
6.1	K_L Beam at Hall D	21

6.1.1	Beamline Delivery for Secondary K_L Beam	24
6.1.2	K_L Beam Parameters	26
6.1.3	K_L Beam Background: Muons, Neutrons, and Gammas	27
6.1.4	K_L Momentum Determination and Beam Resolution	29
6.2	LH ₂ /LD ₂ Cryogenic Target for Neutral Kaon Beam at Hall D	31
7	Expected Results and Beam Time Requirements	33
7.1	Hyperon spectroscopy	33
7.2	Expectations for Λ^* and Σ^* Spectroscopy via a $K^+\Xi$ PWA	36
7.3	Expected results in Strange Meson Spectroscopy	39
7.3.1	Impact on P -Wave Phase-Shift Study	39
7.3.2	$K\pi$ S -Wave and Kappa Investigation	40
7.4	Expected Statistical Accuracy	44
7.5	Expected Systematic Uncertainties	45
8	Summary and Beam Time Request	46
	Appendices	48
A1	The Interest of the RHIC/LHC Community in Excited Hyperon Measurements	48
A2	Previous Measurements for Hyperons	51
A3	Determination of Pole Positions	53
A4	Neutron and Gamma Background	57
A5	Hyperon Spectroscopy: Details of Monte Carlo Study	62
A5.1	K_L Beam	62
A5.2	The GlueX Detector	62
A5.3	Particle Identification	63
A5.4	Details of MC study for $K_L p \rightarrow K_S p$	65
A5.5	Details of MC study for $K_L p \rightarrow \pi^+ \Lambda$	66

A5.6 Details of MC study for $K_L p \rightarrow K^+ \Xi^0$ and $K_L n \rightarrow K^+ \Xi^-$	70
A5.6.1 $K_L p \rightarrow K^+ \Xi^0$:	71
A5.6.2 $K_L p \rightarrow K^+ \Xi^-$:	76
A5.7 $K_L n \rightarrow K^+ \Xi^-$:	78
A5.8 Details of MC study for $K_L p \rightarrow K^+ n$	79
A6 $K\pi$ Study	85
A6.1 Simulation Study of $K_L p \rightarrow K^{*0} p \rightarrow K^+ \pi^- p$	85
A6.2 $K^*(892)$ Production in KLF	85
A7 Current Hadronic Projects	89
A7.1 Project X, USA	89
A7.2 J-PARC, Japan	89
A7.3 Belle, Japan	90
A7.4 BaBar, USA	90
A7.5 \overline{P} ANDA, Germany	91
A7.6 COMPASS, CERN	91
A8 Additional Physics Potential with a K_L Beam	92

1 Executive Summary

We propose to establish a secondary K_L beamline at JLab Hall D for scattering experiments on both proton and neutron (for the first time) targets in order to determine the differential cross sections and the self-polarization of strange hyperons with the GlueX detector. These data will allow for precise partial wave analysis (PWA) for the determination of all resonances up to 2500 MeV in the spectra of the Λ , Σ , Ξ , and Ω hyperons, the knowledge of which is very poor compared to the nucleon.

The firm establishment of the lowest hyperon multiplets will allow for a stringent test of heavy quark spin symmetry, and provide clear benchmarks for forthcoming Lattice QCD calculations. Together with the progress made in understanding the spectrum of baryons containing charm and beauty quarks by experiments such as LHCb and Belle II, these hyperon measurements will provide new insight into the behavior of QCD over a wide range of mass scales.

In addition, this facility provides a unique environment to study strange meson spectroscopy through the $K\pi$ interaction, to locate the pole positions in S -, P - and D -waves. The experiment will provide further support of the existence of the low-lying strange scalar meson $\kappa(800)$ and significantly improve on the uncertainties of determination of its mass and the width.

The K_L beam will be generated by directing a high energy, high intensity photon beam onto a Be-target upstream of the GlueX detector. The flux of the K_L beam will be $\sim 1 \times 10^4$ K_L /s on a liquid hydrogen/deuterium (LH_2/LD_2) cryogenic target within the GlueX detector, which has a large acceptance with coverage of both charged and neutral particles. This flux will allow statistics in the case of the hydrogen target to exceed that of earlier experiments by almost three orders of magnitude. The main components of the experimental setup related to the K_L beamline are the Compact Photon Source, the Be-target assembly with a beam plug, the sweeping magnet and the Flux Monitor.

At the first stage the KLF program will focus on two-body and quasi-two-body reactions: elastic $K_L p \rightarrow K_S p$ and charge-exchange $K_L p \rightarrow K^+ n$ reactions, then on two-body reactions producing $S = -1$ ($S = -2$) hyperons as $K_L p \rightarrow \pi^+ \Lambda$, $K_L p \rightarrow \pi^+ \Sigma^0$, and $K_L p \rightarrow \pi^0 \Sigma^+$ ($K_L p \rightarrow K^+ \Xi^0$), as well as three body $K_L p \rightarrow K^+ K^+ \Omega^-$.

A coupled channel PWA of the KLF data can be performed standalone and in conjunction with an analysis of the data from the J-PARC $K^- p$ measurements, if available. The best fit will determine the partial wave amplitudes and the resonance pole positions, residues and Breit-Wigner (BW) parameters. These will provide a benchmark for results of forthcoming Lattice QCD calculations and elucidate the structure of the strange hyperons.

Recently, the GlueX collaboration organized broad discussions on the future physics opportunities with the GlueX setup at Hall D summarized in a White Paper, where there is a considerable interest in KLF as a potential new direction. Based on the technical requirements and minimum construction timelines, we expect that experiments with the K_L beam in Hall D could begin in 4 years, consistent with the completion of the currently approved GlueX physics program. This time scale would allow the KLF program to begin prior to competitive and complementary experiments at upcoming international facilities.

2 Scope of the Proposal

The nature of QCD confinement continues to provide a challenge to our understanding of soft QCD. Experimental investigation of the baryon spectrum provides the obvious avenue to understand QCD in this region since the location and properties of the excited states depend on the confining interaction and the relevant hadronic degrees of freedom.

Through analyses of decades worth of data, from both hadronic and electromagnetic scattering experiments, numerous baryon resonances have been observed, many of which with masses, widths, and quantum numbers fully determined. There are 109 baryons in the PDG2018 listings, but only 58 of them with 4* or 3* quality [3]. Many more states are predicted by quark models (QMs). For example, in the case of $SU(6)_F \times O(3)$ symmetry, 434 resonances would be required, if all partly revealed multiplets were completed (three 70-plets and four 56-plets).

The light and strange quarks can be arranged in six baryonic families, N^* , Δ^* , Λ^* , Σ^* , Ξ^* , and Ω^* . The possible number of members in a family is not arbitrary [4]. Under the $SU(3)_F$ symmetry these are the octet: N^* , Λ^* , and Σ^* , and the decuplet: Δ^* , Σ^* , Ξ^* , and Ω^* . The number of experimentally identified resonances in each baryon family in PDG2018 summary tables is 17 N^* , 24 Δ^* , 14 Λ^* , 12 Σ^* , 7 Ξ^* , and 2 Ω^* . Constituent QMs, for instance, predict the existence of no fewer than 64 N^* and 22 Δ^* states with masses less than 3 GeV. The “missing-states” problem [5] is obvious from these numbers. To complete $SU(3)_F$ multiplets, one needs no fewer than 17 Λ^* s, 41 Σ^* s, 41 Ξ^* s, and 24 Ω^* s.

If these “missing resonances” exist, they have either eluded detection or have produced only weak signals in the existing data sets. The search for those resonances provides a most natural motivation for future measurements at Jefferson Lab. As stated in the *2015 Long Range Plan for Nuclear Science* [2]: *For many years, there were both theoretical and experimental reasons to believe that the strange sea-quarks might play a significant role in the nucleon’s structure; a better understanding of the role of strange quarks became an important priority.*

The JLab 12 GeV energy upgrade, with the new Hall D, provides an ideal tool for extensive studies of both non-strange and, specifically, strange baryon resonances [6, 7]. Our plan is to take advantage of the existing high-quality photon beamline and the experimental area in the Hall D complex at Jefferson Lab to deliver a beam of K_L particles onto a LH_2/LD_2 target within the GlueX detector. The recently constructed GlueX detector is a large-acceptance spectrometer with good coverage for both charged and neutral particles that can be adapted to this purpose. Obviously, a K_L beam facility with good momentum resolution is crucial for providing the data needed to identify and characterize the properties of hyperon resonances. The masses and widths of the lowest Λ and Σ baryons were determined mainly with kaon beam experiments in the 1970s [3]. The first determinations of the pole position in the complex-energy plane for a hyperon, for instance, for the $\Lambda(1520)3/2^-$, have been made only recently [8]. An intense K_L beam would open a new window of opportunity, not only to locate “missing resonances”, but also to establish their properties by studying different decay channels systematically.

A recent white paper, dedicated to the physics with meson beams and endorsed by a broad physics community, summarized unresolved issues in hadron physics, and outlined the vast opportunities

and advances that only become possible with a “secondary beam facility” [9]. The Hall D K-long Facility (KLF) measurements will allow studies of very poorly known multiplets of Λ^* , Σ^* , Ξ^* , and even Ω^* hyperons with unprecedented statistical precision. These measurements also have the potential to observe dozens of predicted (but heretofore unobserved) states and to establish the quantum numbers of already observed hyperon resonances listed in PDG2018 [3]. Interesting puzzles exist for PDG-listed excited hyperons that do not fit into any of the low-lying excited multiplets, and these need to be further revisited and investigated. Excited Ξ s, for instance, are very poorly known. Establishing and discovering new states is important, in particular, for determination of the multiplet structure of excited baryons.

We have organized four Workshops: *Physics with Neutral Kaon Beam at JLab* (KL2016) (February 2016) [10], *Excited Hyperons in QCD Thermodynamics at Freeze-Out* (YSTAR2016) (November 2016) [11], *New Opportunities with High-Intensity Photon Sources* (HIPS2017) (February 2017) [12], and *Pion-Kaon Interactions* (PKI2018) (February 2018) [13]. They were dedicated to the physics of hyperons produced by the neutral kaon beam. The KL2016 Workshop [14] followed our LoI-12-15-001 [15] to help address the comments made by PAC43 and to prepare the full proposal for PAC45 [16]. The proposed KLF program is complementary, for instance, to the CLAS12 baryon spectroscopy experiments [17, 18] and would operate at Hall D for several years. The YSTAR2016 Workshop [19] was a successor to the recent KL2016 Workshop and considered the influence of possible “missing” hyperon resonances on QCD thermodynamics, on freeze-out in heavy ion collisions and in the early universe, and in spectroscopy. Then, the HIPS2017 Workshop [20] aimed at producing an optimized photon source concept with potential increase of scientific output at Jefferson Lab, and at refining the science for hadron physics experiments benefitting from such a high-intensity photon source. Finally, the PKI2018 Workshop is dedicated to the physics of strange mesons produced by the neutral kaon beam [21].

Additionally, the proposed facility will also have great impact in the strange meson sector by measurements of the final-state $K\pi$ system from threshold up to 2 GeV in invariant mass to establish and improve on pole positions and widths of all $K^*(K\pi)$ P -wave states and the S -wave scalar mesons $K_0^*(800)$ or $\kappa(800)$. In particular, the $\kappa(800)$ meson has been under discussion for decades and still remains to be unequivocally confirmed with corresponding quantum numbers by detailed phase-shift analysis with high statistics data [22, 24].

The proposal is organized in the following manner. The case of hyperon spectroscopy is given in Sec. 3, followed by a discussion of partial-wave phenomenology and previous measurements in Sec. 4. A short overview for strange meson spectroscopy is given in Sec. 5. Our proposed K_L beam facility is described in Sec. 6 including: K_L production and properties of the secondary K_L beam, measurements of K_L flux, and cryogenic target. Expected results and beam time requirements are described in Sec. 7 while summary and a beam time request is given in Sec. 8. The Appendices contain many technical details for our proposal.

3 The Case for Strange Hyperon Spectroscopy

The present experimental knowledge of the spectra of strange hyperons remains remarkably incomplete. For example, only the lowest negative-parity doublet and the positive parity singlet of the Λ hyperon are well established. In the case of the Σ and Ξ hyperons, only the lowest decuplet resonance states $\Sigma(1385)$ and $\Xi(1530)$ are well established. In this section, we discuss this context for the proposed hyperon spectroscopy program and a few highlights of proposed measurements which will address the outstanding questions in the field.

3.1 Heavy Quark Symmetry and the Hyperons

Heavy quark symmetry [25] provides a powerful tool for comparing the structure of hyperons with heavy (charm and bottom) flavor quarks to those with strange quarks. This symmetry follows from the fact that the strength of quark spin-orbit couplings scale with the inverse of the constituent mass. In the case of hyperons with light and heavy quarks this implies that the heavy quark spin decouples from those of the light quarks. Heavy quark symmetry suggests, that the ratio of the sizes of such spin-orbit splittings in the corresponding multiplets in the spectra of the strange, charm and beauty hyperons should approximately correspond to the ratio of the inverses of the corresponding constituent quark (or approximately) meson (K , D , B) masses. Where the spin-orbit splittings conform to this scaling law the implication is that the structure of the corresponding hyperon resonances in the different flavor sectors are similar.

This symmetry can be tested experimentally by comparing the spin-orbit splittings between the Ξ hyperons in the different flavor sectors. Hitherto the comparable splittings are only known for the lowest negative parity doublets in the strange, charm and beauty hyperon spectra, with two light-flavor and only one single heavy quark. The recent observation of a rich spectrum of narrow Ξ_{cc} [26, 27], Ξ_b [28] and Ω_c [29] states has yielded significant theoretical developments in heavy quark spectroscopy. The determination of the mass spectrum and quantum numbers of the $S = -2$ Cascade resonances beyond the $\Xi(1530)$ at KLF will be essential to test these developments to the strange quark sector and compare with recent and forthcoming LQCD calculations [30]. This is *a fortiori* the case for the spectrum of the Ω hyperons.

3.2 Strange Hadrons from the Lattice

Our knowledge of the excited-state spectrum of QCD through the solution of the theory on a Euclidean-space lattice has undergone tremendous advances over the past several year. What we characterize as excited states are resonances that are unstable under the strong interaction, and their properties are encapsulated in momentum-dependent scattering amplitudes.

The methodology for obtaining momentum-dependent phase shifts for elastic scattering from the shifts in energy levels on a Euclidean lattice at finite volume was provided many years ago [31] and extended to systems in motion [32], but its implementation for QCD remained computationally elusive until recently. A combination of theoretical, algorithmic, and computational advances has

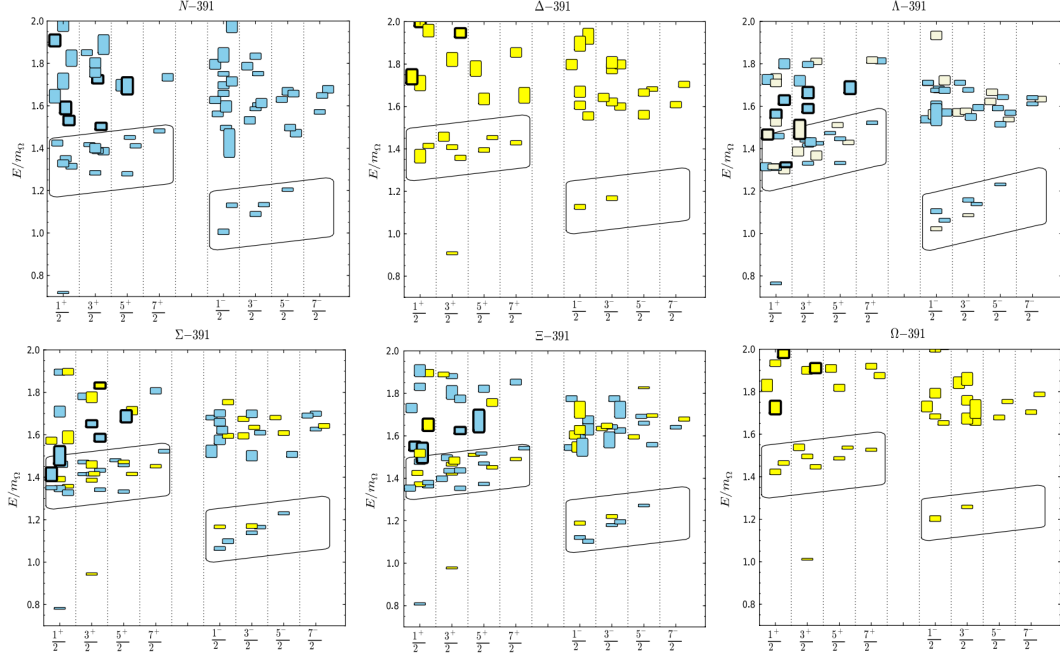


Figure 1: Results for baryon excited states using an ensemble with $m_\pi = 391$ MeV are shown versus J^P [30]. Colors are used to display the flavor symmetry of dominant operators as follows: blue for 8_F in N , Λ , Σ , and Ξ ; beige for 1_F for Λ ; yellow for 10_F in Δ , Σ , Ξ , and Ω . The lowest bands of positive- and negative-parity states are highlighted within slanted boxes. Hybrid states, in which the gluons play a substantive role, are shown for positive parity by symbols with thick borders.

changed this situation dramatically, notably in the case of mesons. There have been several lattice calculations of the momentum-dependent phase shift of the ρ mesons [33–39]. This has now been extended to $K\pi$ scattering [40] in both P - and S -wave.

The formulation to extract amplitude information has been extended to the coupled-channel case [41–49], and applied to the case of the coupled $K\bar{K} - \pi\pi$ [50] system describing the ρ resonance to the $\eta K - \eta\pi$ system [51, 52], and to the emblematic isoscalar sector [53, 54]. Most recently, a calculation of coupled isoscalar $\pi\pi$, $K\bar{K}$, and $\eta\eta$ scattering for both S and D wave has been performed [53], revealing a qualitative interpretation of σ , f_0 , and f_2 mesons similar to that seen in experiment. Collectively, these papers provide a comprehensive picture of $SU(3)$ nonets both in the tensor and scalar sectors, albeit at unphysically large pion mass.

The application to baryons is far more limited but, nonetheless, important insights have been gained. In an approach in which the excited-state hadrons are treated as stable particles, a spectrum of baryons at least as rich as that of the quark model is revealed [55, 56], and evidence has been presented for “hybrid” baryon states, beyond those of the quark model, in which gluon degrees of freedom are essential [57]. Notably, this picture extends to the spectrum of Λ , Σ , Ξ , and Ω states where the counting of states reflects $SU(6) \times O(3)$ symmetry, and the presence of hybrids is common across the spectrum. In Fig. 1, baryon spectra from [30] are presented in units of Ω mass from LQCD calculations with ensemble $m_\pi = 391$ MeV (not yet at physical m_π).

The calculations for the baryon sector are incomplete, in that the momentum-dependent scattering

amplitudes characterizing multi-hadron states have not been extracted. In comparison with the calculations for mesons cited above, the challenges are more computational than theoretical or conceptual. Nonetheless, the first direct calculation of the $I = 3/2$ $N\pi$ system in P -wave has now been performed [58], revealing a Breit-Wigner description of the amplitude commensurate with a phenomenological description of the Δ resonance. Thus we can be confident that the progress made in the meson sector will be reflected for the case of baryons in the coming years. Indeed, many of the algorithmic and computational challenges, notably the need to perform calculations at physical quark masses, and the increasing complexity of the Wick contractions as the number of hadrons, and therefore quarks, is increased, are being addressed with the recently launched Exascale Computing Project of the DOE and NNSA, whose application to lattice QCD is described in Ref. [59].

3.3 Highlights of the KLF Hyperon Program

Lattice QCD and quark model calculations predict a rich spectrum of Λ^* and Σ^* states, many of which have large widths that can be studied at KLF but are not easily accessible in other reactions. As a typical example in Fig. 2 we demonstrate a complete PWA extraction of a fairly low lying but already broad Σ^* resonance in the reaction $K_{Lp} \rightarrow \Xi^0 K^+$ assuming 20 (100) days of running shown in green (yellow), see Sec. 7.2 for details. A clean discrimination of broad excited states on top of many overlapping resonances with various different quantum numbers is a key feature of the KLF, unmatched by comparable experiments. The precision of KLF data clearly allows for the identification of these excited states in a mass range not accessible with previous measurements, and determination of their quantum numbers and pole positions to be compared with calculations from Lattice QCD [30].

The spectrum of Ξ hyperons also clearly has significant discovery potential with implications for heavy quark symmetry and relationships to mass splittings in charm and beauty hyperons. The bottom panel of Fig. 2 demonstrates the branching ratio sensitivity for several excited $\Xi^* \rightarrow \Lambda K$ as a function of running days for the experiment (see Sec. 7.1 for details). These states are expected to be narrow and can be directly compared to the spectrum predicted by Lattice QCD [30].

In summary, this proposal aims to address many of the key open questions in strange hyperon spectroscopy discussed in this section. The highlights shown here demonstrate the ability to determine the pole positions and decay modes of many resonances using rigorous PWA methods, beyond naive “bump hunting” assignments listed by in the Particle Data Group [3]. The KLF experiment will settle the spectrum of Λ^* , Σ^* , Ξ^* and even Ω^* spectra in the mass range up to 2500 MeV. More details about the theoretical and experimental techniques to be employed in KLF experiments can be found in following sections and supplementary materials.

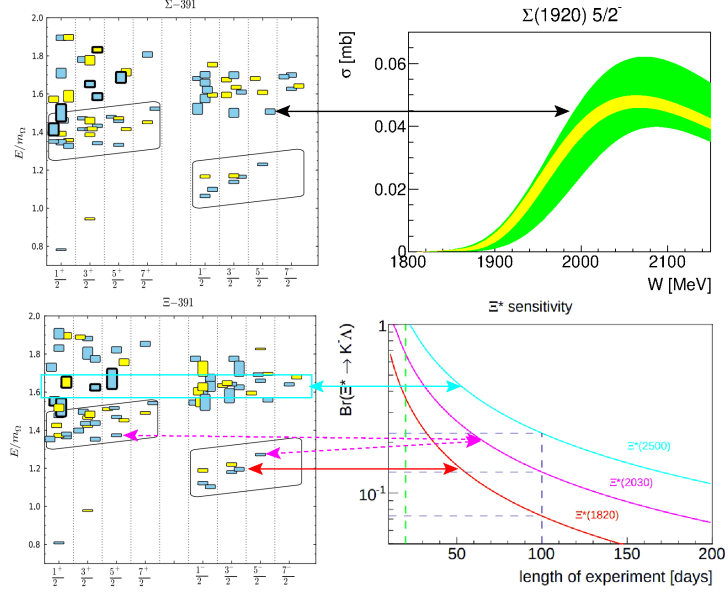


Figure 2: Example of comparison between expected KLF measurements (right) and Lattice QCD predictions for the hyperon spectrum [30] (left), see Sections 7.2 and 7.1 of the text for details.

4 Phenomenology / Partial-Wave Analysis

Here, we summarize some of the physics issues involved with K_L scattering processes. Following Ref. [60], the differential cross section and polarization for $K_L p$ scattering are given by

$$\frac{d\sigma}{d\Omega} = \lambda^2(|f|^2 + |g|^2) \quad \text{and} \quad P \frac{d\sigma}{d\Omega} = 2\lambda^2 \text{Im}(fg^*), \quad (1)$$

where $\lambda = \hbar/k$, with k the magnitude of CM momentum for the incoming meson. Here $f = f(W, \theta)$ and $g = g(W, \theta)$ are the usual spin-nonflip and spin-flip amplitudes at CM energy W and meson CM production angle θ . In terms of partial waves, f and g can be expanded as

$$f(W, \theta) = \sum_{l=0}^{\infty} [(l+1)T_{l+} + lT_{l-}] P_l(\cos \theta), \quad (2)$$

$$g(W, \theta) = \sum_{l=1}^{\infty} [T_{l+} - T_{l-}] P_l^1(\cos \theta), \quad (3)$$

where l is the initial orbital angular momentum, $P_l(\cos \theta)$ is a Legendre polynomial, and $P_l^1(\cos \theta)$ is an associated Legendre function. The total angular momentum for the amplitude T_{l+} is $J = l + \frac{1}{2}$, while that for the amplitude T_{l-} is $J = l - \frac{1}{2}$. For hadronic scattering reactions, we may ignore small CP-violating terms and write

$$K_L = \frac{1}{\sqrt{2}}(K^0 - \bar{K}^0) \quad \text{and} \quad K_S = \frac{1}{\sqrt{2}}(K^0 + \bar{K}^0). \quad (4)$$

We may generally have both $I = 0$ and $I = 1$ amplitudes for KN and $\bar{K}N$ scattering, so that the amplitudes $T_{l\pm}$ can be expanded in terms of isospin amplitudes as

$$T_{l\pm} = C_0 T_{l\pm}^0 + C_1 T_{l\pm}^1, \quad (5)$$

where $T_{l\pm}^I$ are partial-wave amplitudes with isospin I and total angular momentum $J = l \pm \frac{1}{2}$, with C_I the appropriate isospin Clebsch-Gordan coefficients.

We plan to do a coupled-channel PWA with new KLF data in combination with available new J-PARC K^- measurements when they will come. Then the best fit will allow to determine model-independent (data-driven) partial-wave amplitudes and associated resonance parameters (pole positions, residues, BW parameters, etc.) as the SAID group does, for instance, for the analysis of πN -elastic, charge-exchange, and $\pi^- p \rightarrow \eta n$ data [61].

In the following sections we outline some of the outstanding questions in the hyperon spectrum, overview the available data on KN scattering and introduce theoretical predictions for the unexplored domain of measurements with “neutron” targets.

4.1 The $\Lambda(1405)1/2^- - \Lambda(1520)3/2^-$ Doublet

In the quark model, the $\Lambda(1405)1/2^- - \Lambda(1520)3/2^-$ doublet is a flavor singlet of three quarks (uds). Dynamical versions of this model, with two-body interactions between the quarks can describe the low mean energy of this multiplet, but not the 115 MeV splitting between them. This has led to suggestions that there may even be two different $1/2^-$ states – one dynamical low $\bar{K}N$ resonance at 1405 MeV, and an unresolved higher state close to 1520 MeV [62]. A two pole structure of $\Lambda(1405)$ was indeed found in Ref. [63]. The narrow pole lies slightly below $\bar{K}N$ threshold, and is fixed by the scattering data rather well, see Ref. [64] for the comparison of different coupled-channel approaches. However, the position of the second pole is determined less precisely, and may lie much further below $\bar{K}N$ threshold and deeper in the complex plane. Recent photoproduction data on $\pi\Sigma$ by CLAS [65] may be used to reduce the theoretical ambiguity on this (second) pole of $\Lambda(1405)$ [66]. Modern lattice QCD (LQCD) calculations also support the view that its structure is a $\bar{K}N$ state [67,68]. In Skyrme’s topological soliton model for the baryons, the low-lying $\Lambda(1405)$ state also appears naturally as a mainly 5-quark state [69,70]. Lattice calculations based on the sequential Bayesian do, however, indicate that the multiplet may have a mainly 3-quark structure [71].

In the case of those lowest energy flavor-singlet $1/2^- - 3/2^-$ parity doublets in the strange, charm and bottom hyperon spectra: $\Lambda(1405) - \Lambda(1520)$, $\Lambda_c(2595) - \Lambda_c(2625)$, $\Xi_c(2790) - \Xi_c(2815)$, and $\Lambda_b(5912) - \Lambda_b(5920)$ [3] the ratio between the splittings in these three doublets are 14.4:3.7:3.1:1. These ratios agree qualitatively and within 30% with the corresponding inverse ratios of the K , D , and B meson masses: 10.7:2.8:1. As these resonances all contain one light quark pair the latter is what one should expect from the gradual approach to heavy-quark symmetry with increasing meson (or constituent quark) mass if the quark structure of these three multiplets is similar. As described in Sec. 4.9, data on neutron targets described in this proposal have the potential to provide key insights into settling the nature of the $\Lambda(1405)$.

4.2 The Low-Lying Positive-Parity Resonances

In the spectra of the nucleon and the Λ and Σ hyperons, the lowest positive-parity resonances all lie below the lowest negative-parity multiplets except for the flavor singlet doublet $\Lambda(1405)1/2^- - \Lambda(1520)3/2^-$. This reversal of normal ordering cannot be achieved in the constituent quark model with purely color-spin dependent quark interactions. These low-lying positive-parity resonances are the $N(1440)$, $\Lambda(1600)$, and $\Sigma(1660)1/2^+$ states. Their low masses do however appear naturally, if the interactions between the quarks are flavor dependent [72]. Present day LQCD calculations have not yet converged on whether these low-lying states can be described as having a mainly three-quark structure [71, 73].

In the spectrum of the Ξ , the $\Xi(1690)$ may be such a $1/2^+$ state as well, although the quantum numbers of that state are yet to be determined.

In the corresponding decuplet spectra, a similar low-lying positive-parity state has so far only been definitely identified in the $\Delta(1232)$ spectrum: namely, the $\Delta(1600)3/2^+$. The $\Sigma(1840)3/2^+$ resonance very likely represents the corresponding positive-parity Σ^* state. It should be important to identify the corresponding $3/2^+$ state in the spectrum of the Ξ^* .

4.3 The Negative-Parity Hyperon Resonances

In the spectrum of the nucleon, two well-separated groups of negative-parity resonances appear above the $1/2^+$ state $N(1440)$. This lowest energy group consists of the $N(1535)1/2^-$ and the $N(1520)3/2^-$ resonances. There is a direct correspondence in the $\Lambda(1670)1/2^-$ and the $\Lambda(1690)3/2^-$ resonances. There is also a repeat of this group in the spectrum of the Σ hyperon in the two resonances $\Sigma(1620)1/2^-$ (tentative) and $\Sigma(1670)3/2^-$.

The $N(1535)$ resonance has a large (32–52 %) decay branch to ηN , even though its energy lies very close to the ηN threshold. This pattern repeats in the case of the $\Lambda(1670)$, which also has a substantial (10–25 %) decay branch to the corresponding $\eta\Lambda$ state. As the still uncertain $\Sigma(1620)1/2^-$ resonance is located almost exactly at the threshold for $\eta\Sigma$, there is naturally no signal for an $\eta\Sigma$ decay from it.

In the spectrum of the Ξ hyperon, none of the hitherto determined negative-parity multiplets is complete. The state $\Xi(1820)3/2^-$ may be the analog in the Ξ spectrum of the states $N(1520)$, $\Lambda(1670)$, and $\Sigma(1670)$. It should be important to identify the lowest $1/2^-$ resonance in the Ξ spectrum. If that resonance lacks an η decay branch, it would demonstrate that the η decay of the $1/2^-$ resonances in the spectra of the nucleon, Λ and Σ involves two quarks.

It should also be important to determine whether the uncertain “bumps” referred to in the Particle Data Tables labelled $\Sigma(1480)$, $\Sigma(1560)$, and $\Xi(1620)$ represent true resonances [3].

About 120 MeV above the $1/2^- - 3/2^-$ pair of nucleon resonances $N(1535)$ and $N(1520)$, the nucleon spectrum has three negative-parity resonances close in energy to one another. This multiplet is formed of the $N(1650)1/2^-$, $N(1700)3/2^-$, and $N(1675)5/2^-$ resonances.

The analogs in the spectrum of the Λ of the first and last of these nucleon resonances are the

$\Lambda(1800)1/2^-$ and the $\Lambda(1830)5/2^-$ resonances. The missing $3/2^-$ state in this Λ resonance multiplet has not yet been identified.

A common feature of all the $1/2^-$ resonances in these multiplets is their substantial η decay branch.

4.4 KN and $\bar{K}N$ Final States

A fair amount of data are available for the reaction, $K^+n \rightarrow K^0p$, measured on a deuterium target. Figure 3 shows a sample of available differential cross sections for $K_L p \rightarrow K_S p$ compared with predictions determined from a recent PWA of $\bar{K}N \rightarrow \bar{K}N$ data [74, 75], combined with $KN \rightarrow KN$ amplitudes from the SAID database [76]. The predictions at lower and higher energies tend to agree less well with the data.

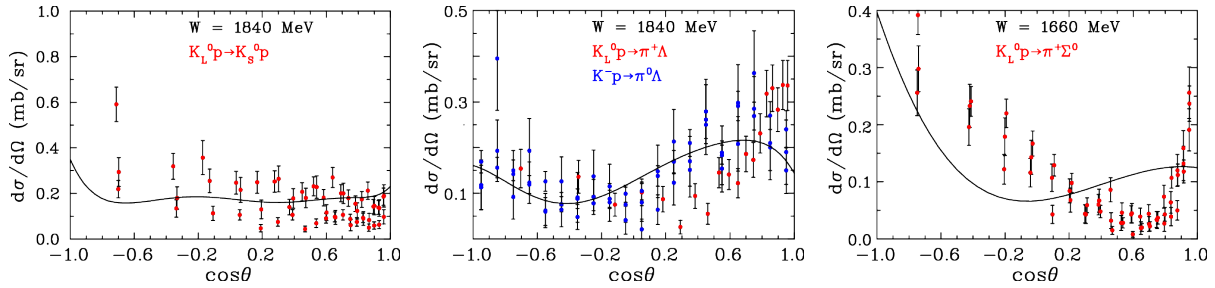


Figure 3: Selected differential cross section data for $K_L p \rightarrow K_S p$ (left), $K_L p \rightarrow \pi^+ \Lambda$ (middle) at $W = 1840$ MeV and $K_L p \rightarrow \pi^0 \Sigma^+$ at $W = 1660$ MeV (right) from Ref. [77]. The plotted data from previously published experimental data are those data points within 20 MeV of the kaon CM energy indicated on each panel [76]. Plotted uncertainties are statistical only. The curves are predictions using amplitudes from a recent PWA [74, 75], combined with $KN \rightarrow KN$ amplitudes from the SAID database [76].

4.5 $\pi\Lambda$ Final States

The $K^- p \rightarrow \pi^0 \Lambda$ and $K_L p \rightarrow \pi^+ \Lambda$ amplitudes imply that observables for these reactions measured at the same energy should be the same except for small differences due to the isospin-violating mass differences in the hadrons. No differential cross section data for $K^- p \rightarrow \pi^0 \Lambda$ are available at CM energies $W < 1540$ MeV, although data for $K_L p \rightarrow \pi^+ \Lambda$ are available at such energies. At 1540 MeV and higher energies, differential cross section and polarization data for the two reactions are in fair agreement, as shown in Figs. 3 and 4. It should be stressed that polarized measurements are tolerable for any PWA solutions (Fig. 4).

4.6 $\pi\Sigma$ Final States

Figure 3 shows a comparison of differential cross section data for $K^- p$ and $K_L p$ reactions leading to $\pi\Sigma$ final states at $W = 1660$ MeV (or $P_{\text{lab}} = 716$ MeV/c). The curves are based on energy-

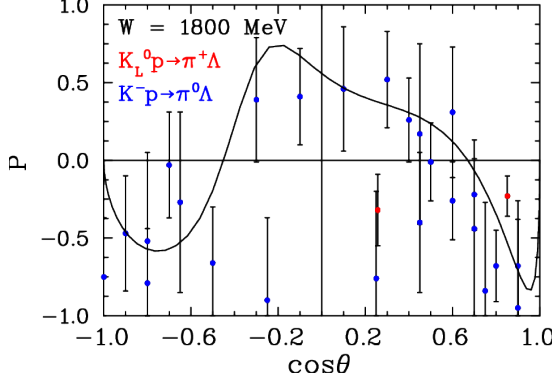


Figure 4: Comparison of selected polarization data for $K^-p \rightarrow \pi^0\Lambda$ and $K_L p \rightarrow \pi^+\Lambda$ at $W = 1880$ MeV, from Ref. [77]. The plotted data from previously published experimental data are those data points within 20 MeV of the kaon CM energy indicated on each panel [76]. The curves are from a recent PWA of $K^-p \rightarrow \pi^0\Lambda$ data [74, 75].

dependent isospin amplitudes from a recent PWA [74, 75]. No differential cross section data are available for $K_L p \rightarrow \pi^0\Sigma^+$. As this example shows, the quality of the $K_L p$ data is comparable to that for the K^-p data. It would, therefore, be advantageous to combine the $K_L p$ data in a new coupled-channel PWA with available K^-p data. Note that the reactions $K_L p \rightarrow \pi^+\Sigma^0$ and $K_L p \rightarrow \pi^0\Sigma^+$ are isospin selective (only $I = 1$ amplitudes are involved) whereas the reactions $K^-p \rightarrow \pi^-\Sigma^+$ and $K^-p \rightarrow \pi^+\Sigma^-$ are not. New measurements with a K_L beam would lead to a better understanding of Σ^* states and would help constrain the amplitudes for K^-p scattering to $\pi\Sigma$ final states

4.7 $K\Xi$ Final States

The threshold for K^-p and $K_L p$ reactions leading to $K\Xi$ final states is fairly high ($W_{\text{thresh}} = 1816$ MeV). There are no differential cross section data available for $K_L p \rightarrow K^+\Xi^0$ and very few (none recent) for $K^-p \rightarrow K^0\Xi^0$ or $K^-p \rightarrow K^+\Xi^-$. Measurements for these reactions would be very helpful, especially for comparing with predictions from dynamical coupled-channel (DCC) models [78, 79] and other effective Lagrangian approaches [80]. The *Review of Particle Physics* [3] lists only two states with branching ratios (Br) to $K\Xi$, namely, $\Lambda(2100)7/2^-$ (Br < 3 %) and $\Sigma(2030)7/2^+$ (Br < 2 %)

4.8 Excited $S = -2$ and $S = -3$ baryons

$SU(3)$ flavor symmetry allows as many $S = -2$ baryon resonances as there are N and Δ resonances combined (~ 27); however, until now only three states, $\Xi(1322)1/2^+$, $\Xi(1530)3/2^+$, and $\Xi(1820)3/2^-$, have their quantum numbers assigned and only a few more states have been observed [3]. For the discovery of excited cascade baryons, we envision a PWA similar to the $S = -1$ sector but more complicated as one is dealing with a three-body final state.

The experimental situation with Ω^{*-} s is even worse than for the Ξ^* case – there are very few data for excited states [81]. The main reason for such a scarce dataset is the very low cross section for their indirect production with pion or photon beams.

A major effort in LQCD calculations involves the determination of inelastic and multi-hadron

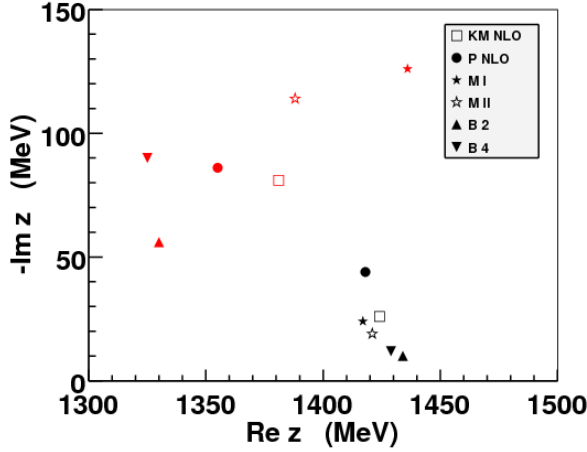


Figure 5: Pole positions of $\Lambda(1405)$ in chiral unitary approaches - KM from Ref. [84], B from Ref. [66], M from Ref. [85], and P from Ref. [86] as compared in Ref. [64]. Each symbol represents the position of the first (black) and second (red) pole in each model.

scattering amplitudes, and the first calculation to study an inelastic channel was recently performed [51,52]. For lattice calculations involving baryons that contain one or more strange quarks an advantage is that the number of open decay channels is generally smaller than for baryons comprised only of the light u and d quarks.

4.9 Theory for “Neutron” Target Measurements

The so-called coupled-channel Chiral Unitary approaches (UChPT) implement unitarity exactly via a re-summation of a chiral potential to a certain chiral order. They successfully describe all available antikaon-nucleon scattering data and predict the mass and width of the sub-threshold resonance in the Isospin $I = 0$ channel, the $\Lambda(1405)1/2^-$. Furthermore, such models lead to the prediction of the second pole in the complex energy plane with the same quantum numbers as $\Lambda(1405)1/2^-$. This is usually referred to as the two-pole structure of the $\Lambda(1405)$, see the current review by the Particle Data Group [3] for more details.

In the most advanced formulation, such a UChPT approach relies on a chiral amplitude for meson-baryon scattering up to next-to-leading chiral order. The unitarity constraint is imposed via the Bethe-Salpeter equation either in the full off-shell formulation [82,83] or in the so-called on-shell approximation [66,84]. For the analysis of data the former is quite intricate, while as it was shown in Ref. [82] the off-shell effects are rather small. Recently, a direct quantitative comparison of the on-shell models [66,84–86] was performed in Ref. [64]. It was found there that various models, which typically have many free parameters, adjusted to the same experimental data, predict very different behavior of the scattering amplitude on and off the real energy-axis. This systematic uncertainty becomes evident, when comparing the pole positions of the $\Lambda(1405)$ in these models (see Fig. 5). The position of the narrow (first) pole seems to be constraint at least in the real part rather well, while the predictions for the position broad (second) pole cover a very wide region of the complex energy-plane. This uncertainty is present even within models of the same type. This ambiguity can be traced back to the fact that the experimental data used to fix the parameters of the models is rather old and imprecise.

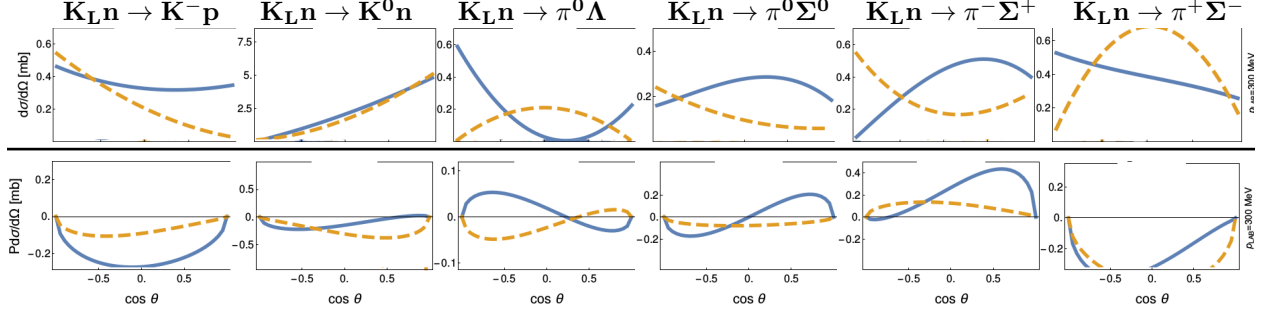


Figure 6: Theoretical predictions for $d\sigma/d\Omega$ (top) and $Pd\sigma/d\Omega$ (bottom) as a function of CM \cos of a meson production angle for kaon lab-momentum of 300 MeV/c of initial neutral kaon beam. Orange dashed and blue solid lines show predictions within Model-B2 and Model-B4, respectively.

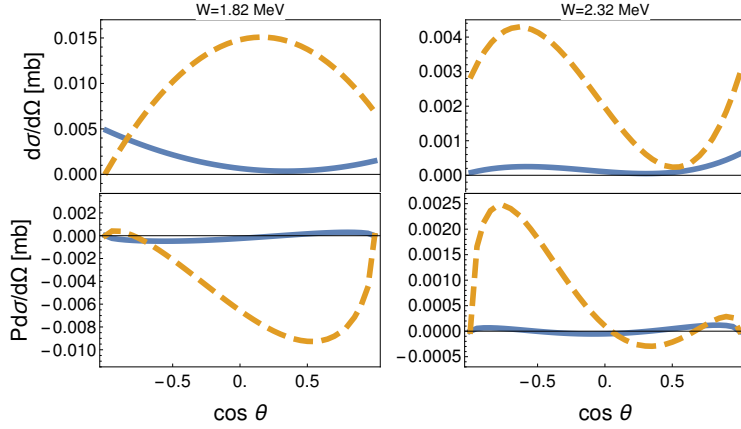


Figure 7: Predictions for $d\sigma/d\Omega$ and $Pd\sigma/d\Omega$ as a function of CM \cos of a meson production angle, θ , for the reaction $K_L n \rightarrow K^+ \Xi^-$. Each column is associated with kaon laboratory momentum of 300 and 700 MeV/c of initial neutral kaon beam. Orange (dashed) and blue lines show predictions within Model-B2 and Model-B4, respectively.

The K_L beam can be scattered on a neutron target, while measuring the strangeness $S = -1$ final meson-baryon states. In such a setup, the proposed experiment will become a new and very strongly desired source of experimental data to pinpoint the properties of the antikaon-nucleon scattering amplitude. To make this statement more quantitative, we compare predictions of both solutions of the model from Ref. [66]. These solutions agree with all scattering, threshold as well as the photoproduction data for the $\Sigma\pi$ line shapes by the CLAS Collaboration [65]. The predicted differential cross sections ($d\sigma/d\Omega$) as well as polarized ones ($Pd\sigma/d\Omega$) for the $K_L n$ scattering with the final states $K^- p, \bar{K}^0 n, \pi^0 \Lambda, \pi^{0/+/-} \Sigma^{0/-/+}$ are presented in Fig. 6. There is no clear agreement between both prediction of these observables in the energy range aimed to study in the proposed K_L experiment. The latter is very encouraging in the sense that the actual data can sort out one (or maybe both) solutions as unphysical, which was not possible by the present experimental data. As for the $K\Xi$ final states being measured at KLF, both solutions of the here presented model can be used for a theoretical estimate. The reason of being able to do so is that $K^+ \Xi^-$ and $K^0 \Xi^0$ channels are part of the channel space of ground state octet mesons-baryon channels dynamically implemented into the present model. The result of such a prediction is depicted and addressed further in Fig. 7.

4.10 Summary for PWA

The pole positions have been determined (no uncertainties) for several Λ^* s and Σ^* s but the information about the pole positions have not been determined for Ξ or Ω hyperons [3]. Our plan is to do a coupled-channel PWA with new KLF data in combination with available and new J-PARC K^-p measurements when they will be available. Then the best fit will allow the determination of data-driven (model independent) partial-wave amplitudes and associated resonance parameters (pole positions, residues, BW parameters, and so on). See Appendix A3 for a more detailed discussion. Additionally, PWAs with new KLF data will allow a search for “missing” hyperons via looking for new poles in complex plane positions. It will provide a new benchmark for comparisons with QCD-inspired models and LQCD calculations.

5 πK Scattering Amplitudes and Strange Meson Resonances

5.1 Note on the Strange Meson Spectrum

It is instructive to compare the spectrum of the kaons to the corresponding spectra of the D and the D_s mesons (see Ref. [87]). With exception of the still uncertain spin 0 state κ or $K_0^*(800)$ the known parts of the kaon, the D and the D_s mesons are qualitatively very similar, but with somewhat different orderings [3].

The established part of the strange meson spectrum [3, 87] begins with the 0^- ground state, followed by the 1^- $K^*(892)$ vector meson state, which is followed by the two 1^+ states $K_1(1270)$, $K_1(1400)$, and then the recurrence $K^*(1410)$ of the 1^- vector meson state and the scalar meson state $K_0^*(1430)$. The spectrum of the D meson differs only in that the corresponding scalar meson state $D_0^*(2400)$ slightly below, rather than slightly above the two 1^+ states $D_1(2420)$ and $D_1(2430)$.

This comparison of the spectra of the K , D and D_s mesons reveals the importance of settling the existence of the κ or $K_0^*(800)$, as its existence would settle the existence of a light scalar nonet below 1 GeV. This would imply the existence of corresponding low-lying scalar meson states in the spectra of the charm and charm-strange mesons. In all these spectra, the first recurrence of that low scalar meson is well established by the states $K_0^*(1430)$, $D_0^*(2400)$, and $D_{s0}^*(2317)$. Given the very large width of the non-strange scalar meson $f_0(500)$ (or σ), it may be expected that the κ and the lowest charm strange, charm and charm-strange mesons will have similar large widths and threshold effects. Moreover, establishing firmly the existence of the $\kappa/K_0^*(800)$, with similar characteristics to the $\sigma/f_0(500)$, would also kill the glueball interpretations of the latter [88] or the dilatonic interpretation [89].

5.2 Strange Exotics

Two important motivations for new measurements of πK scattering amplitudes, are the attention received by Chiral Perturbation Theory [90–93], resonance and unitarized models [94–98], and the need to confirm the existence of the exotic κ meson (or $K_0^*(800)$) in the $I = 1/2$ S -wave. This state would be the strange counterpart of the σ (or $f_0(500)$) meson which is now rather well established from $\pi\pi$ scattering (see the review [99]).

For spectroscopy, the relevance of this state, which according to the Review of Particle Physics [3] still “needs confirmation”, is twofold: First, establishing firmly its existence will settle the long-standing debate on whether there is a low-lying scalar nonet, with the $\sigma/f_0(500)$, the $f_0(980)$ and $a_0(980)$ as partners. But, second, because there is mounting evidence that such a nonet is actually exotic, i.e., not an ordinary quark-antiquark state [100–109]. Knowing with precision the κ features, particularly its pole position, mass, width, and $K\pi$ coupling will support, or not, such scenario.

For Chiral Perturbation Theory the interest is on the low energy parameters, particularly the scalar scattering lengths. Below, we discuss the existing tension between dispersive analyses of experi-

mental data [110,111], theoretical predictions from Chiral Perturbation Theory [92,93], and lattice calculations [112–115]. One of the main difficulties for extracting reliable values from experiment is that the existing πK data starts at 750 MeV, and one needs an extrapolation down to the threshold at ~ 635 MeV. Thus, the new KLF input at low energies, together with the general improvement in statistics, will settle this issue.

At this point, it is worth noting the decisive role that the precise low-energy data from the NA48/2 experiment [116] played for the revision of the $\sigma/f_0(500)$ in the RPP. In this regard, improved measurements of the S -wave πK phase-shifts at low energy ($E \lesssim 1$ GeV) would be highly desirable in order to play a similar role for the $\kappa/K_0^*(800)$. On the one hand, the existence of this type of resonance is linked to the fact that the phase-shift passes through 45° sufficiently close to the threshold. This is in contrast with the case of an ordinary resonance which corresponds to a fast increase of the phase-shift passing through 90° . Fig. 8 illustrates how these phase behaviors on the real axis are related to the presence of a zero of the S matrix on the first Riemann sheet (corresponding to a resonance pole on the second Riemann sheet). The figure, which is based on amplitudes generated from the Roy-Steiner equations (to be discussed below) suggests that the $I = 1/2$ S -wave displays both an exotic resonance and an ordinary one. On a more quantitative side precision measurements of the S -wave phase-shifts would allow application of the Padé approximant method for determining the positions of the resonances (see, e.g., [117]. This method has been recently applied to πK scattering, and a κ pole has been found in Ref. [118] using as an input the fit to data constrained with Forward Dispersion Relations obtained in Ref. [111].

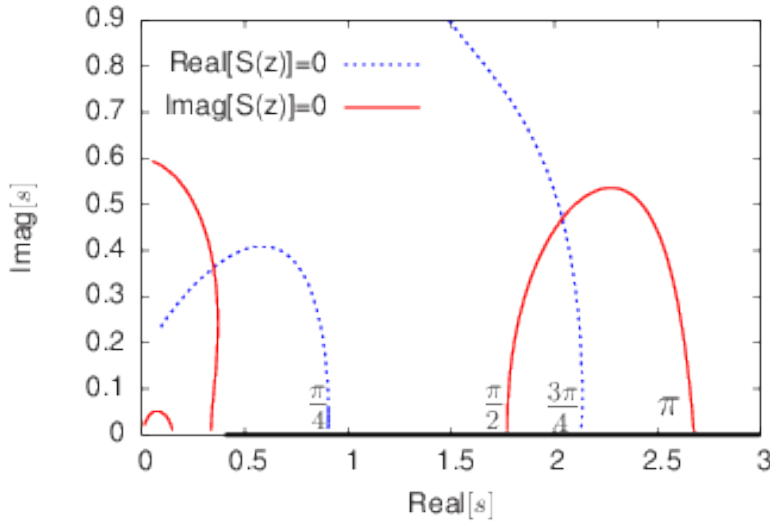


Figure 8: Zeros of the S -matrix, for the $I = 1/2, J = 0$ πK partial-wave on the first Riemann sheet. The figure shows the lines which correspond to $Re[S] = 0$ and $Im[S] = 0$ (intersection of the two lines, obviously, corresponds to a zero of S) and some important phase-shift values on the real axis.

Alternatively, the most rigorous way to determine this resonance pole is using Roy-Steiner (RS) type equations [119, 120]. These equations rely on the first principles like analyticity, crossing as well as data. They provide a suitable framework for performing extrapolations in the low energy region, $E < 1$ GeV, of the S and P partial waves given sufficiently precise inputs at higher energies, essentially in the range (1 – 2) GeV. Extrapolations to complex values of the energies can be

performed with the same accuracy as on the real axis. Unlike the Padé approximant approach, the extrapolation of the $I = 1/2$ S -wave from the RS equations requires inputs from other partial waves as well since the equations form a coupled system. Based on the existing data set, an estimate of the κ pole position from the RS equations was performed in Ref. [24]. Note that no input on πK scattering in the scalar partial waves below 1 GeV was used for this estimate. Using this Roy-Steiner equations with the data produced in KLF would produce an actual experimental and rigorous determination of the κ pole.

In the P -wave, finally, the studies by the LASS Collaboration [121, 122] have identified besides the well known $K^*(892)$ a new meson, the $K^*(1410)$. This meson has an unexpectedly low mass as it appears to be essentially degenerate with the non-strange $\rho(1450)$ or $\omega(1420)$ vector mesons. Its properties are not very precisely known at present.

5.3 Status of πK Scattering Measurements

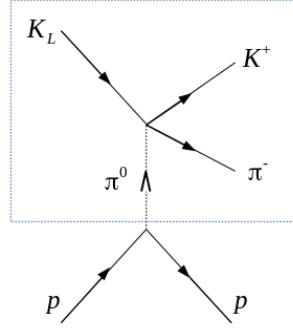


Figure 9: Illustration of the contribution from one-pion exchange, which is dominant at small momentum transfer, to the production amplitude $K_L p \rightarrow K^+ \pi^- p$.

The traditional method for measuring $\pi K \rightarrow \pi K$ amplitudes is from production measurements

$$Kp \rightarrow K\pi p, \quad Kp \rightarrow K\pi n, \quad Kp \rightarrow K\pi \Delta \quad (6)$$

focusing on the region of small momentum transfers $|t| < 0.1 - 0.2 \text{ GeV}^2$, which is accessible with kaon beams of a few GeV. In this region, the amplitude is dominated by the one pion exchange contribution, see Fig. 9. The same method was used for measuring $\pi\pi \rightarrow \pi\pi$ amplitudes, details can be found in the book [123]. The two experiments performed at SLAC [122, 124] have the largest statistics and provide the best determinations of the πK scattering amplitudes at present. They cover the energy ranges $0.73 \leq E \leq 1.85 \text{ GeV}$ (Ref. [124]) and $0.83 \leq E \leq 2.52 \text{ GeV}$ (Ref. [122]), respectively. References to earlier work can be found in the review [125].

A completely different approach to measuring the πK phase-shifts makes use of Watson's theorem for weak decay form factors. In this manner, the phase-shift difference $\delta_S - \delta_P$ was determined by analyzing the $D^+ \rightarrow K^- \pi^+ e^+ \nu$ by the BaBar Collaboration [126]. The results are in agreement with the LASS determination but more statistics are needed before one reaches a comparable precision. Similarly, from the measurement of the energy distribution in the decay $\tau^- \rightarrow K_S \pi^- \nu$ by the

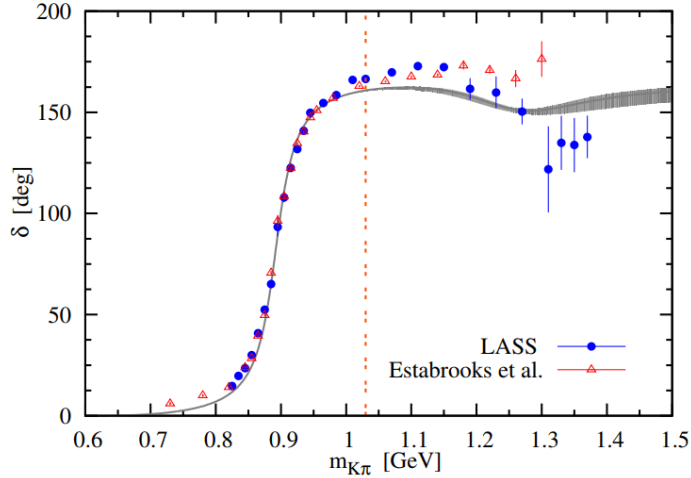


Figure 10: Phase of the πK vector form factor as determined in Ref. [128] and compared with the P-wave phase shifts from Refs. [122, 124]. The two phases should be identical, by Watson’s theorem, in the elastic scattering energy region.

Belle Collaboration [127] the P -wave phase has been determined [128], relying on the analyticity properties of the form factor. Their result is shown in Fig. 10. Since Watson’s theorem is valid in the energy region of elastic scattering, these alternative phase determinations provide important information on the effective onset of inelastic scattering in the various partial waves. The figure also shows that the determination of the phase shift in the region of the $K^*(1410)$ resonance is not very precise and could be improved.

The same form factors which appear in the $\tau \rightarrow K\pi\nu$ decays are also involved in the K_{l3} decay amplitudes: $K \rightarrow \pi e\nu$, $K \rightarrow \pi\mu\nu$. A series of new K_{l3} experiments were undertaken recently in order to improve the determination of V_{us} (see Ref. [129]). As shown in Ref. [129], an optimal analysis of the K_{l3} data is achieved by using a description of the two form factors involved based on phase dispersive representations rather than phenomenological polynomial or pole forms as done previously.

πK scattering also plays an important role in a number of three-body decays, like $D \rightarrow K\pi\pi$. Recently, a method was developed [130] which allows to compute the effect of the three-body rescattering in terms of the known two-body $\pi\pi$ and πK T -matrices. This could be useful for identifying small CP violating effects in the charm sector.

5.4 Theory

Pions and kaons are QCD pseudo-Goldstone bosons, therefore the πK amplitudes at low energy can be expressed as a chiral expansion. The NLO calculation was performed in Ref. [92] who predict the following results for the scattering lengths,

$$a_0^{1/2} = 0.19 \pm 0.02, \quad a_0^{3/2} = -0.05 \pm 0.02 \quad (7)$$

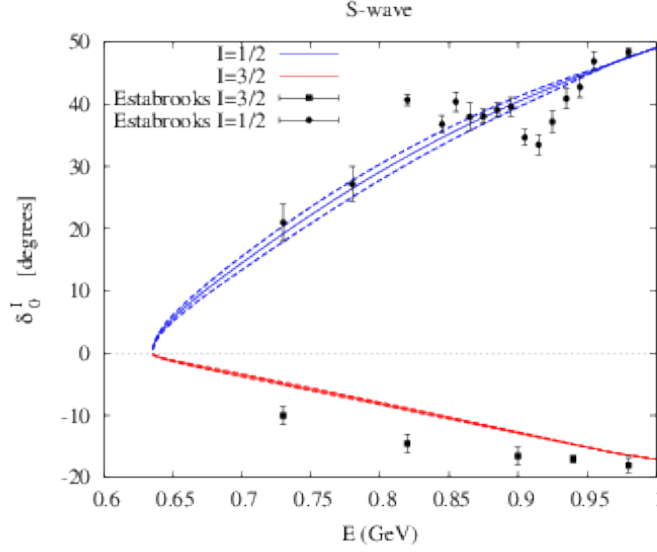


Figure 11: Results for the S -wave phase shifts extrapolated below 1 GeV based on the Roy-Steiner dispersive equations (from Ref. [110]) compared with the experimental data from Ref. [124].

(in units of m_π^{-1}). Verifying these predictions would provide an important check of the three-flavor chiral expansion. Based on experimental phase-shift measurements this is possible, in principle, using dispersion relations for extrapolating down to the threshold. The Roy-Steiner equations provide a suitable framework for that. This is illustrated in Fig. 11 which shows the extrapolated results for the S -waves in the region $E \leq 1$ GeV, based on experimental inputs from Refs. [122, 124] in the region $E > 1$ GeV. It is clear that the availability of more precise data in the range $E \leq 1$ GeV would greatly strengthen the efficiency of this method. We note that a direct experimental estimate of the scattering length difference was performed recently [131] based on the lifetime of the $\pi^+ K^-$ atom at the DIRAC experiment at CERN. Unfortunately, the experimental errors are still too large and do not provide really precise information about the pion-kaon scattering lengths.

Alternatively, scattering phase shifts can be computed in lattice QCD using Lüscher's method [31]. Results for πK phase shifts were first obtained in Refs. [132, 133] and in Ref. [51]. In this last work, the influence of one inelastic scattering two-body channel is accounted for and $m_\pi = 391$ MeV. Very recently, results for $m_\pi = 230$ MeV have been presented [40]. Once physical values for m_π are reached, these lattice QCD results can be compared directly to experimental measurements of the πK phase shifts which provides a direct probe of the quality of the numerical QCD solution.

Finally, let us note that there is a sizable tension between the values of scattering lengths obtained from dispersive analyses of data [110, 111], on one side, and the predictions from Chiral Perturbation Theory [92, 93] and lattice calculations [112–115], on the other side. The values of this threshold parameters are related to two important questions. On the one hand, for phenomenology, establishing the convergence and reliability of SU(3) Chiral Perturbation Theory. On the other hand, for the foundations of QCD, the size of the strange versus the non-strange chiral condensate, i.e., the detailed pattern of the QCD spontaneous chiral symmetry breaking is very important.

As previously noticed and as shown in Fig. 11, the existing πK data starts at 750 MeV, and one

needs an extrapolation down to the threshold at ~ 635 MeV. Hence, the new KLF data at low energies, together with the general improvement in statistics, will be determinant to resolve this tension.

5.5 Highlights of the Strange Meson Program

Measurements of $K\pi$ scattering in the S -wave will allow the K_L -Facility to contribute to our understanding of the elusive κ meson, as described in Sec. 7.3.2. Figure 12 shows the expected improvement in the determination of the mass and width of the κ that can be reached with 100 days of running time.

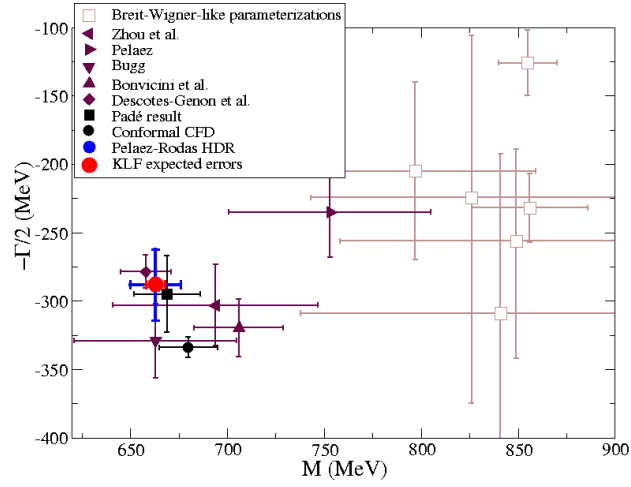


Figure 12: Expected precision on the κ pole parameters for 100 days of running time (see Sec. 7.3.2 for details).

6 Proposed KL Beam Facility

We propose to use the KL Facility with the GlueX spectrometer, in JLab Hall D, to perform precision measurements of $K_L N \rightarrow KY^*$ and $K_L N \rightarrow Y^* \rightarrow \pi Y, KN, K\Xi$ from liquid hydrogen and deuterium cryogenic targets (LH_2/LD_2) in the resonance region, $W = 1490 - 2500$ MeV, and $\text{CM } \cos \theta$ from -0.95 to 0.95 . It will operate at a neutral kaon flux of $1 \times 10^4 K_L/s$ (that is by three order of magnitude higher than SLAC had in the past [134]). The ability of GlueX to measure over wide ranges in θ and ϕ with good coverage for both charged and neutral particles, together with the K_L energy information from the KL Facility, provide an ideal environment for these measurements.

6.1 K_L Beam at Hall D

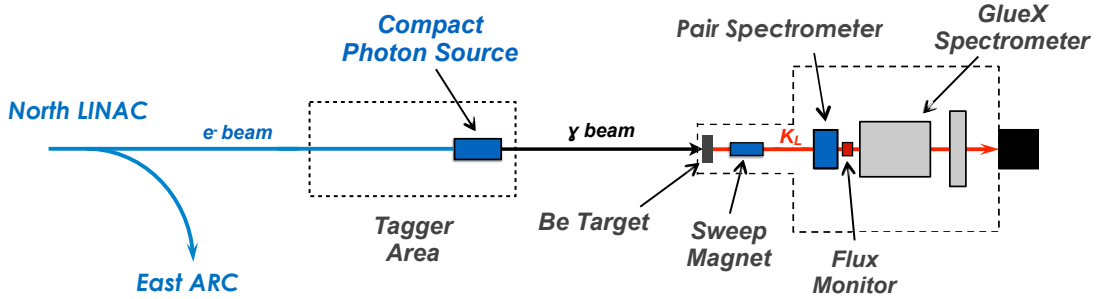


Figure 13: Schematic view of Hall D beamline on the way $e \rightarrow \gamma \rightarrow K_L$. Electrons first hit the copper radiator inside of CPS, then photons hit the Be target, and finally, neutral kaons hit the LH_2/LD_2 cryogenic target. The main components are the CPS, Be target assembly, sweep magnet, and neutral kaons FM (see the text for details). Beam goes from left to right.

Schematic view of the Hall D beamline for KLF is presented in Figure 13. At the first stage, 12 GeV electrons will scatter in the copper radiator (10 % R.L.) inside the Compact Photon Source (CPS) generating an intense beam of untagged bremsstrahlung photons. The CPS will be located downstream of the tagger magnet. The tagger alcove has more space than that available in Halls C/A. So the positioning of the CPS and the placement of shielding are simplified. The Hall D tagger magnet and detectors will not be used. The CPS design combines in a single properly shielded assembly all elements necessary for the production of the intense photon beam, such that the overall dimensions of the setup are limited and the operational radiation dose rates around it are acceptable. For Hall D, the dose rates in the vault during full 60 kW beam operations with the CPS are comparable to the nominal running conditions in the vault. More details about the CPS can be found in **CPS supplementary materials** [20, 135].

At the second stage, bremsstrahlung photons, created by electrons will hit the Be target assembly located at the beginning of the collimator cave (Fig. 14), and produce neutral kaons along with neutrons, photons, and charged particles which will be thrown away by the magnetic field. Lighter elements provide higher photoproduction yield for a unit of radiation length. Beryllium targets

were used for K_L production at SLAC [136] and NINA [137]. The beam tungsten plug of a 0.10 m thick (30 R.L.) is connected to the beryllium to clean up the beam and confine induced radiation.

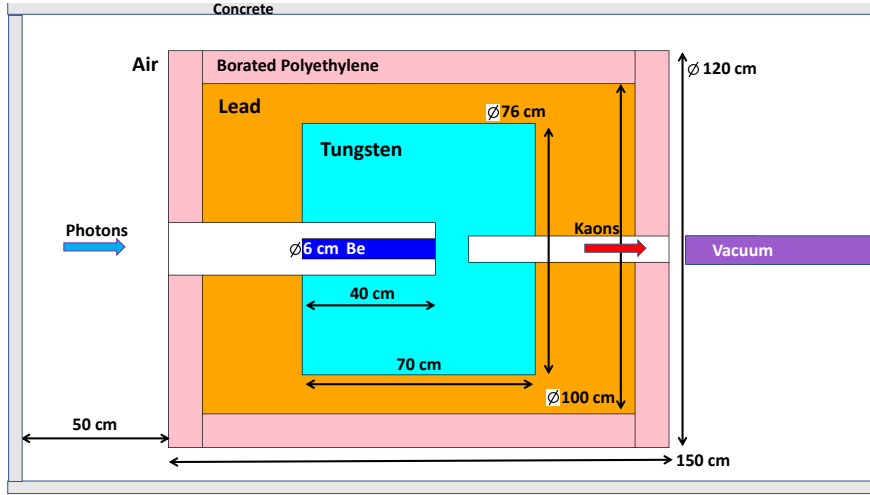


Figure 14: Schematic view of the Be-target (K_L production target) assembly. Concrete, borated polyethylene, lead, tungsten, beryllium, vacuum beam pipe, and air shown by grey, pink, brown, light blue, blue, violet, and white color, respectively. Beam goes from left to right.

Changeover from the photon to the K_L beamline and from the K_L to the photon beamline requires further evaluation. However, initial conservative estimates are that this changeover could be completed approximately in 6 months. Therefore, the majority of this changeover could be completed during a typical summer shutdown period in the CEBAF accelerator schedule. The collimator cave has enough space (with the 4.52 m width) for the Be-target assembly to remain far enough from the beamline. Water cooling would be required around the beryllium and tungsten plug. Cooling water available in the experimental hall is sufficient to dissipate 6 kW of power delivered by the photon beam. More details about a Be-target assembly are in **Be-target supplementary materials** [138].

The GlueX wiki [139] is a source of the collimator cave geometry. Additional shielding inside the collimator cave was optimized to minimize the neutron and γ background in the experimental hall and to satisfy the RadCon requirement establishing the radiation dose rate limit in the experimental hall (1 mrem/h). The permanent sweeping magnet (3.83 m in length) is placed right after the second concrete wall. It cleans up the charged component of the beam and has a field integral of 0.8 Tm, which is enough to remove all charged background coming out of the Be-target assembly.

The vacuum beam pipe has a $\varnothing 0.07$ m and prevents neutron rescattering in air. Finally, K_L mesons will reach the LH_2/LD_2 cryogenic target located inside the GlueX spectrometer. The distance between the primary Be and cryogenic targets is 24 m.

An accurate determination of the K_L beam flux is necessary to maximize the physics impact of the resulting data. To reach an accuracy of $<5\%$ in the determination of the flux, we plan to build a dedicated FM which would utilize in-flight decays of the K_L . To account for various possible acceptance effects during K_L beam propagation from the Be-target, we plan to measure the K_L flux upstream of the GlueX detector, utilizing the Hall D Pair Spectrometer [140] as shielding against K_L which have decayed further upstream. The FM will measure a small fraction of decayed K_L 's, concentrating on the portion decaying within a distance of 2 m downstream of the Pair Spectrometer magnet center (see Fig. 15). The FM is a combination of solenoid magnetic field spectrometer and a time of flight detectors. The FM consists of the following major parts: the front

Property	Value
Electron beam current (μA)	5
Electron flux at CPS (s^{-1})	3.1×10^{13}
Photon flux at Be-target $E_\gamma > 1500 \text{ MeV}$ (s^{-1})	2.6×10^{11}
K_L beam flux at cryogenic target (s^{-1})	1×10^4
K_L beam σ_p/p @ 1 GeV/c (%)	~ 1.5
K_L beam σ_p/p @ 2 GeV/c (%)	~ 5
K_L beam nonuniformity (%)	< 2
K_L beam divergence ($^\circ$)	< 0.15
K^0/\bar{K}^0 ratio at cryogenic target	2:1
Background γ flux at cryogenic target, $E_\gamma > 50 \text{ MeV}$ (s^{-1})	$\sim 10^5$
Background γ flux at cryogenic target, $E_\gamma > 500 \text{ MeV}$ (s^{-1})	$\sim 10^3$
Background neutron flux at cryogenic target (s^{-1})	6×10^4

Table 1: Expected electron/photon/kaon beam conditions at the K_L experiment.

Property	Value
Copper radiator in CPS (%R.L.)	10
\varnothing Be-target (m)	0.06
Be-target length (m)	0.40
\varnothing LH ₂ /LD ₂ cryogenic target (m)	0.06
LH ₂ /LD ₂ cryogenic target length (m)	0.40
Photon beamline length (m)	67
Kaon beamline length (m)	24

Table 2: Expected targets properties at the K_L experiment.

cap, forward tracker, backward tracker, endcap, and solenoidal magnet. The FM can be further equipped with a plastic scintillator barrel, covering inner part of a magnet and a start counter (FMSC), comprising plastic scintillator bars covering the beampipe, from the location of the Pair Spectrometer magnet to the FM magnet 15.

To be measured by the FM, both charged particles from the kaon decay need to be incident within the FM acceptance. Taking into account the different branching ratios, we expect to reconstruct the following number of K_L from various decay channels (see Fig. 16 (left)). One can quantify the expected rate in terms of the achievable statistical error within a one day measurement (see Fig. 16 (right)). For the kaon beam momenta range appropriate for the hyperon program a 1 % statistical error of the K_L flux determination is achievable in less than a day.

An accurate flux monitoring requires determination of the kaon flux as both a function of transversal position within the beampipe and kaon energy. The most inner 3 cm of the transverse beam profile at the position of the FM would correspond to a 6 cm profile at the cryogenic target. A $\varnothing 7$ cm beam pipe allows sufficient margins and the clean definition of a fiducial regions of the transverse beam profile at the FM position. All in all we expect to measure about 1.1k kaon/s in the FM.

Flux Monitor

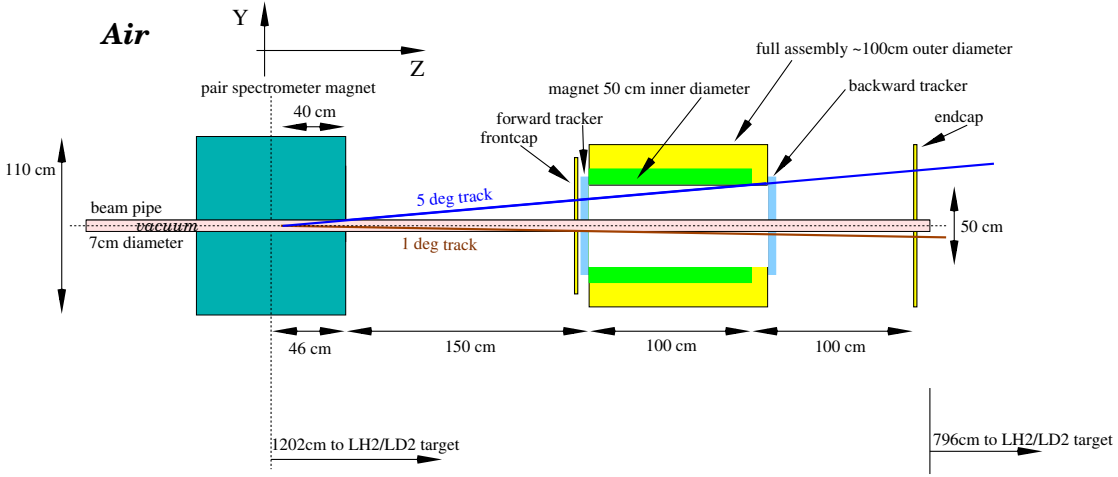


Figure 15: Schematic view of the Flux Monitor setup.

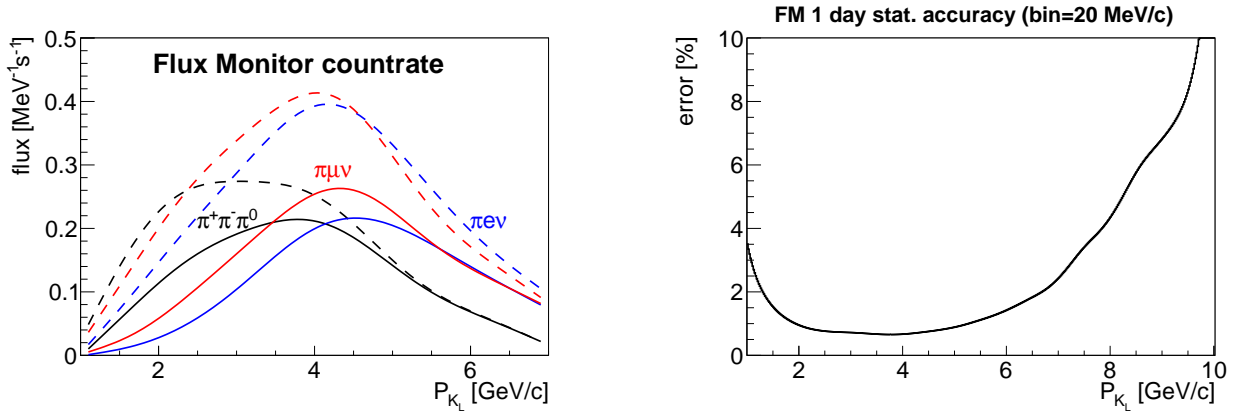


Figure 16: The Flux Monitor performance. Left panel: Visible K_L flux for various decay channels within the FM acceptance. Solid lines correspond to a system with front/end-caps only. Dashed lines show the improvement one can obtain with the additional barrel part extension to the FM. Right panel: Expected statistical accuracy for 1 day FM measurement ($\pi^+\pi^-\pi^0$ branch only) in 20 MeV/ c momentum bin.

More details about the FM can be found in **FM supplementary materials** [141]. All our MC calculations have been performed for the JLab Hall D beamline geometry. Tables 1 and 2 summarize beam properties and dimensions of targets, respectively.

6.1.1 Beamline Delivery for Secondary K_L Beam

The proposed secondary K_L experiment requires time-of-flight measurements, which in turn requires substantially lower bunch repetition rates in CEBAF than the nominal 249.5 MHz or 499 MHz. Gun laser hardware lends itself to powers of two reductions in repetition rates, so this proposal in-

cludes beam delivery at either the 32nd (15.59 MHz) or 64th (7.80 MHz) harmonic of the nominal 499 MHz.

An average dump power limit of 30 kW to 60 kW for 12 GeV electrons in the CPS translates to average beam currents of $2.5\ \mu\text{A}$ to $5.0\ \mu\text{A}$. Combining these beam requirements leads to individual bunch charges shown in Table 3.

Current (μA)	Rep Rate (MHz)	Harmonic of 499 MHz	Bunch Charge (pC)	Equivalent 499 MHz Current (μA)
2.5	15.59	32nd	0.16	80
2.5	7.80	64th	0.32	160
5.0	15.59	32nd	0.32	160
5.0	7.80	64th	0.64	320

Table 3: CEBAF injector bunch currents and repetition rates for Secondary K_L experiment.

Operations with 0.16 pC to 0.32 pC bunch charge has been demonstrated but shown to be challenging in the 12 GeV era. Injector setup time of up to a week is required to limit bunch tails that cause beam trips and background, and intervention on the order of every few days is currently required to maintain a reasonable accelerator availability. The G0 experiment ran 1.6 pC/bunch, but only at 3 GeV with the 6 GeV machine and in a dedicated configuration that required substantial interception to trim beam tails [142].

These concerns may be mitigated somewhat by completion of the injector upgrade program, including operations of a 200 keV gun, in the 2021 timeframe. The HV gun was installed in summer 2018, and some initial tests with modest gun voltages occurred in FY19, but the full injector upgrade for potential high bunch charge availability will not be available for study until FY21 [143].

Low frequency, high power amplifier use has been attempted at CEBAF in recent years, resulting in substantial damage and high amplifier failure rates even near 30 MHz because of high peak power required as repetition rate is lowered. The low bunch repetition rate with high bunch charge therefore also requires considerable investment.

With the existing and planned gun configuration, laser development is required to achieve any of the planned bunch repetition rates. This requires construction of a pulse picker that would pass a sub-harmonic of the 249.5 MHz system (for example, 15.6 MHz) to avoid major impact to the existing 249.5/499 MHz laser systems. Amplification is then required before doubling to the proper wavelength to achieve useful power, even for $10\ \mu\text{A}$ beam. Additional power amplification is necessary for the higher beam currents required here.

To build up a beamline delivery system for the secondary K_L beam requires the pulse picking system and the laser amplifier. The lead time on amplifiers can be long so ideally a year of advance funding would be necessary to design, build and demonstrate the system performance [142].

The G0 experiment [144] used a commercial $\text{Ti:Al}_2\text{SO}_3$ laser with a very long (~ 5 m) optical cavity that was very difficult to keep on and locked to the accelerator RF. This solution is not

practical for the 12 GeV era.

6.1.2 K_L Beam Parameters

Neutral kaon production was simulated for a photon bremsstrahlung beam produced by the 12 GeV electron beam in the Hall D CPS. The main mechanism of K_L production in our energy range is via ϕ -meson photoproduction, which yields the same number of K^0 and \bar{K}^0 . We have taken as a model the Pythia generator [145], which includes hyperon production. Total and differential cross sections for the ϕ -meson photoproduction on proton and complex nuclei (coherent and incoherent) data were taken from Refs. [146,147]. The angular distributions that we used for $\phi \rightarrow K_L K_S$ decay are from Refs. [146,148,149]. Our calculations show that the ϕ decay in its rest frame is mostly perpendicular to the axis of ϕ -momentum. Since K_L s need to stay along the original photon beam direction to get to the LH₂/LD₂ cryogenic target, this condition requires that the ϕ production and decay angles in the laboratory frame be about the same. That means that we will have only K_L s from ϕ -mesons produced at relatively high momentum transfer t at the Be target. It suppresses the number of “useful” K_L s by a factor of ~ 3 or more (in comparison with the case if K_L and K_S momenta are parallel to the ϕ -momentum). The K_L absorption, used in our calculations, was studied extensively in Ref. [150]. More than 80 % of the produced K_L s will be absorbed in the Be target and following tungsten beam plug.

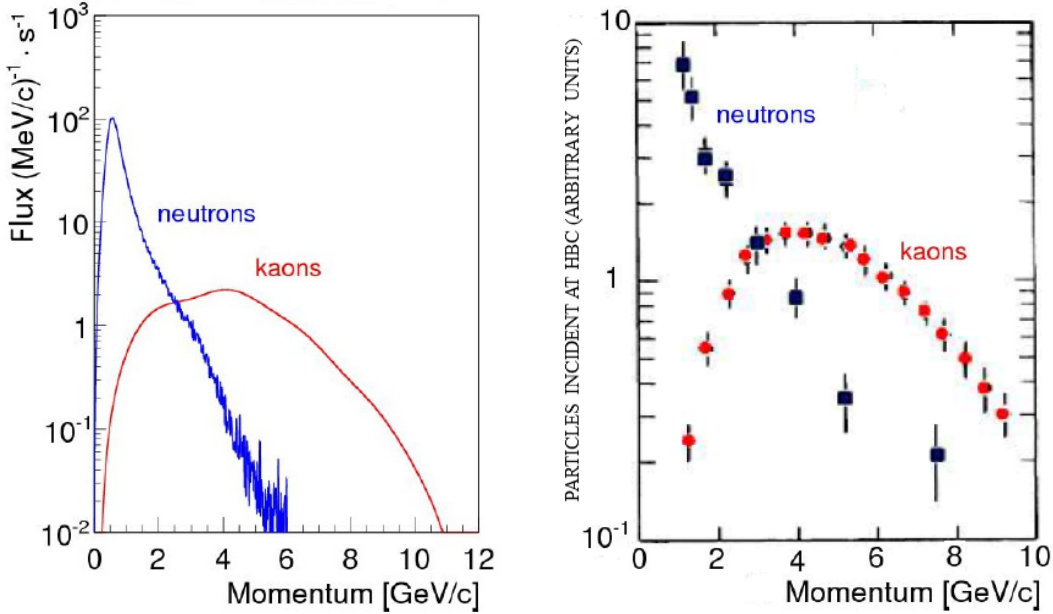


Figure 17: K_L and neutron momentum spectra on the cryogenic target. Left panel: Rate of K_L (red) and neutrons (blue) on the LH₂/LD₂ cryogenic target of Hall D as a function of their generated momentum, with a total rate of 1×10^4 K_L /s and 6×10^4 n /s. Kaon calculations were performed using Pythia generator [145] while neutron calculations were performed using the MCNP transport code [152]. Right panel: Experimental data from SLAC measurements using a 16 GeV/ c electron beam were taken from Ref. [136] (Fig. 2). The rate of K_L (red filled circles) and neutrons (black filled squares) is shown.

One of the main K_L -beam parameters is the momentum distribution (momentum spectrum as a function of the distance and angle) [151]. Results of our simulations for the K_L momentum spectrum for those K_L reaching the LH₂/LD₂ cryogenic target. The spectrum first increases with K_L momentum up to ~ 4 GeV/c since the ϕ decay cone angle decreases at higher γ -beam and K_L -momenta. This selects lower ϕ production t values, which are more favorable according to the ϕ differential cross section. At a certain point, the highest possible γ -beam momentum is reached and the K_L -momentum spectrum decreases to the endpoint. Pythia calculations show that ϕ decays yield roughly 70 % of the K_L flux with the rest originating from hyperon photoproduction. The number of K^0 exceeds the number of \bar{K}^0 by 30 % points according to this generator for our conditions.

To estimate the expected rate of K_L s at the LH₂/LD₂ cryogenic target, we used the conditions listed in Tables 1 and 2 which results in a beam flux of about 1×10^4 K_L/s from all production mechanisms at the cryogenic target (Fig. 17). We simulated the K_L and neutron production from 12-GeV electrons under these conditions for the KL Facility and the results (Fig. 17(left)) are in reasonable agreement with the K_L spectrum measured by SLAC at 16 GeV (Fig. 17(right)).

6.1.3 K_L Beam Background: Muons, Neutrons, and Gammas

Background radiation condition is one of the most important parameters of the K_L beam for the JLab KL Facility [151]. We have performed a comprehensive simulations of the neutron, photon and muon backgrounds and their possible influence on proposed measurement. The neutron and γ flux and dose rate for the KLF experiment is below the RadCon limit as listed in Tables 8 and 9. Overall, the Be-target assembly conceptual design satisfies the RadCon the radiation dose rate limit in the Hall D. All kind of backgrounds are expected to have marginal effect on proposed measurements. Below we summarize the background conditions for each type of particles.

Muon Background

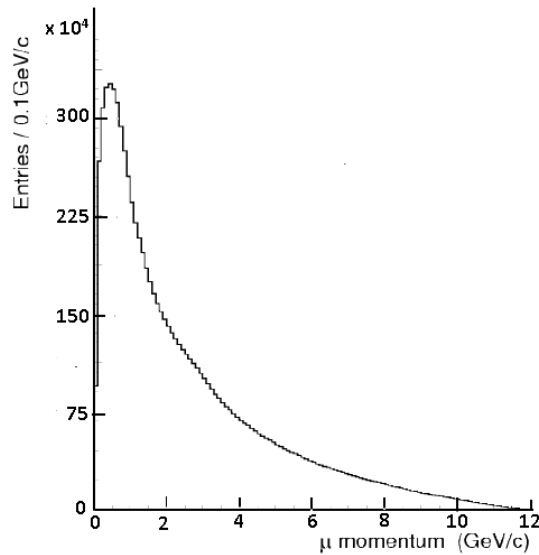


Figure 18: Muon momentum spectrum for Bethe-Heitler production.

Following Keller [153], our Geant4 [154] simulations included Bethe-Heitler muon background from the Be-production target and photon dump at CPS, both background into the detector and muon dose rate outside Hall D. Most of the muons are produced in the photon dump. Our calculations show that muons will be swept out of the K_L beamline; thus, they are not inherently a significant background. However, due to their high penetration ability, it might be important for purposes of the shielding. We have taken into account only the Bethe-Heitler muon production process. Muons from pion decays and other production mechanisms will increase the total muon yield only slightly. They were not included in our model. The number of produced muon in the Be target and tungsten beam plug is about the same, but muons originating in tungsten have a much softer momentum spectrum. The estimated number of produced muons is $\sim 6 \times 10^6 \text{ s}^{-1}$. Their momentum spectrum is shown in Fig. 18.

To summarize: Half of muons will have momenta higher than 2 GeV/c, $\sim 10 \%$ of muons will have momenta higher than 6 GeV/c, and $\sim 1 \%$ of muons will have momenta above 10 GeV/c. Overall, the muon flux for the KLF experiment is tolerable.

Neutron and Gamma Background

To estimate the neutron and γ flux in a beam and neutron dose rate in the experimental hall from scattered neutrons and γ , we used the MCNP6 N-Particle (MCNP) Transport code [152]. The realism of MCNP simulations is based on the advanced nuclear cross section libraries created and maintained in national laboratories of DOE complex. The physical models implemented in the MCNP6 code take into account bremsstrahlung photon production, photonuclear reactions, neutron and photon multiple scattering processes. The experimental hall, collimator cave, and photon beam resulted from copper radiator at CPS were modeled.

The MCNP model simulates a 12 GeV $5 \mu\text{A}$ electron beam hitting the copper radiator inside the CPS. Electron transport was traced in copper radiator, vacuum beam pipe for bremsstrahlung photons, and Be-target. Neutrons and photons were traced in all components of the used MCNP model. The media outside concrete walls of the collimator cave and bremsstrahlung photon beam pipe was excluded from consideration to facilitate the calculations.

Fluence-to-Effective Dose conversion factors from ICRP 116 [155] were implemented to convert neutron fluence to effective dose rate.

The neutron energy on the cryogenic target varied between 0.1 – 1 GeV with an exponentially dropping tail extending up to 10 GeV. The flux is not sufficient to provide a significant background in the case of np or nd interactions in the cryogenic target, see Appendix A4 for details.

The neutron dose rate for the silicon photomultipliers (SiPM) of the start counter [156–158] and BCAL [158, 159] is given in Fig. 19 (left). There is an issue for SiPM and low level of BCAL. Previous studies stand that the dose rate of 30 mreh/h increases a dark current at SiPM by a factor of 5 after 75 days of running period [160].

In our calculations, we took into account Pair Spectrometer and FM magnets and 4 SEG-blocks ($132 \times 132 \times 66 \text{ cm}^3$) shildings around the beam pipe and a concrete block ($132 \times 132 \times 20 \text{ cm}^3$) with a steel collimator for the beam pipe (outer $\varnothing 13 \text{ cm}$ and inner $\varnothing 8 \text{ cm}$). We are confident that the additional steel collimator between SEG-blocks reduces a neutron radiation dose for BCAL up

to <0.1 mrem/h which is negligible. While there is still an issue for SiPMs of the start counter which is 632 ± 145 mrem/h. SiPMs can be replaced with regular PMTs, but we have to worry about shielding the magnetic field. Another option is MCP-PMTs which are rad hard and resistant to magnetic fields.

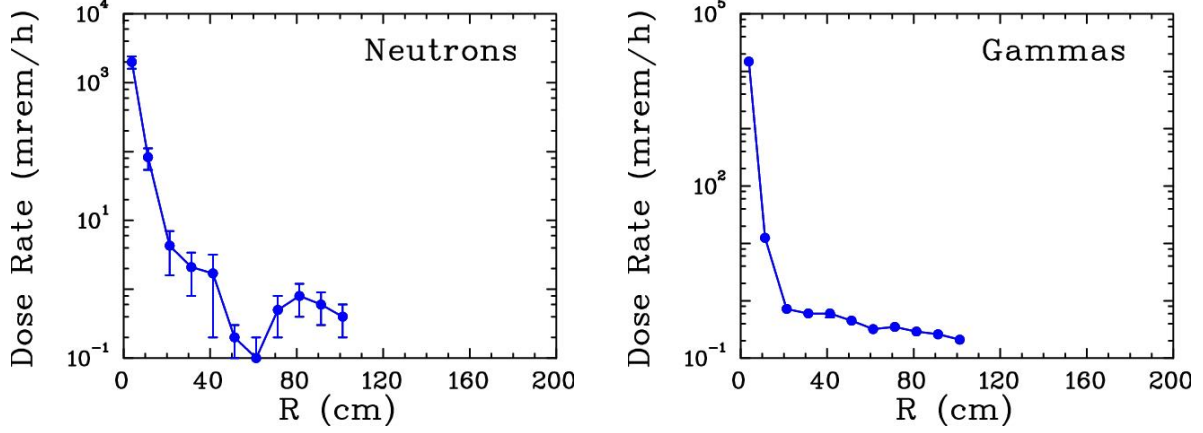


Figure 19: Neutron (left) and γ (right) dose rate background calculated for SiPM and BCAL on the face of the cryogenic target. In this case, we did not take into account additional shielding in the experimental hall.

To estimate the photon flux in a beam and γ dose rate in the experimental hall from scattered neutrons, we used the same MCNP Transport code [152]. After passing through a 30 R.L. tungsten beam plug and the charged background component removed by the sweep magnet, we will have some residual γ background produced by EM showers. It decreases exponentially with increasing energy of photons and vanishes above 30 MeV. The γ dose calculated is $(2.0 \pm 0.1) \times 10^{-2}$ mrem/h which is acceptable by RadCon. More details about the neutron/gamma doses can be found in **Be-target supplementary materials** [138].

To summarize: The neutron and γ flux and dose rate for the KLF experiment is below the RadCon limit as listed in Tables 8 and 9. Overall, the Be-target assembly conceptual design satisfies the RadCon the radiation dose rate limit in the Hall D. The full engineering design is on the way.

6.1.4 K_L Momentum Determination and Beam Resolution

The mean lifetime of the K_L is 51.16 ns ($c\tau = 15.3$ m) whereas the mean lifetime of the K^- is 12.38 ns ($c\tau = 3.7$ m) [3]. For this reason, it is much easier to perform measurements of $K_L p$ scattering at low beam energies compared with $K^- p$ scattering.

The momentum of a K_L beam will be measured using time-of-flight (TOF) - the time between the accelerator bunch (RF signal from CEBAF) and the reaction in the LH_2/LD_2 target as detected by the GlueX spectrometer. Thus the TOF resolution is a quadratic sum of accelerator time and GlueX spectrometer time resolutions. Since the accelerator signal has a very good time resolution on the order of few picoseconds, the TOF resolution will be defined mainly by the GlueX detector. The details of time reconstruction for the TOF is discussed in Sec. 7. In our calculations, we used

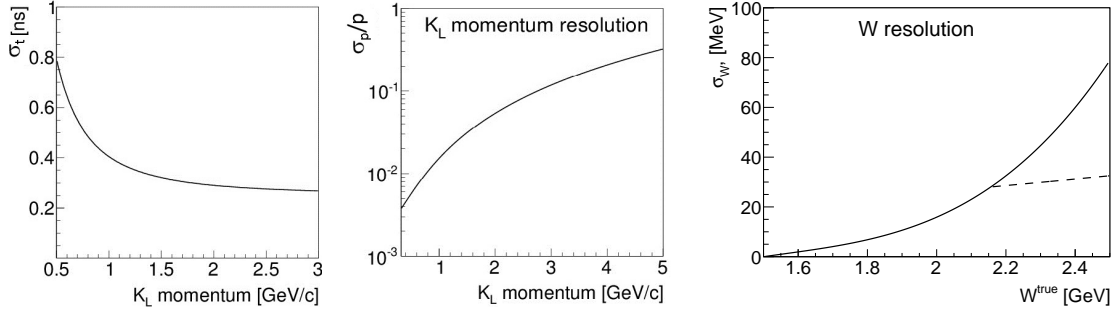


Figure 20: Left panel: Time resolution (σ_t) for K_L beam as a function of K_L -momentum. Middle panel: Momentum resolution (σ_p/p) as a function of momentum (note, log scale). Right panel: Energy resolution (σ_W) as a function of energy. The dashed line shows approximate W resolution from reconstruction of the final-state particles.

currently achieved Start Counter time resolution of 250 ps to show the time and beam momentum resolution vs. kaon momentum (Fig. 20). All hyperon production reactions have very similar TOF and final state reconstructed W -resolution, see Sec. 7 and Appendix A5. While the W resolution vs. W shows on (Fig. 20(right)).

To get precise TOF information, the electron beam needs to have a narrow bunch time structure. As discussed in Sec. 6.1.1, the electron beam can be delivered with predetermined repetition rate. For the K_L experiment, the 64 ns bunch spacing structure is an optimal choice. It allows no cross-bunch overlap for the full range of kaon beam momentum from $p_{K_L} > 320$ MeV/c.

The uncertainty in a neutral kaon production position at lower momenta ($p < 0.5$ GeV/c) affects timing resolution caused by the TOF difference between the photon and kaon time traversing the Be target, however, as $\Delta p/p = \gamma^2 \Delta t/t$ momentum resolution is below 1 % at lower momenta. The TOF resolution is flat for momenta higher than 1 GeV/c. The momentum resolution decreases with momentum: for 1 GeV/c it is ~ 1.5 % and for 2 GeV/c it is ~ 5 %. For fully reconstructed final states W can be reconstructed directly, providing a better resolution in the region where the TOF method deteriorates, $W > 2.2$ GeV (see dashed curve in Fig. 20(right)).

The K_L beam momentum and time resolution are governed by the time resolution provided by the GlueX detector from the reconstruction of charged particles produced in the LH_2/LD_2 target. There are three detector systems that can provide precision timing information for reconstructed charged particles in GlueX: the Start Counter (ST) [157], Barrel Calorimeter (BCAL) [159], and Time of Flight (TOF) detectors. The aforementioned detectors and the charged particle time resolutions they provide are discussed in this section.

The GlueX ST is a cylindrical plastic scintillator detector surrounding the LH_2/LD_2 target, with 3 mm thick scintillator bars and a tapered nose region that bends toward the beamline at the downstream end. The scintillation light from each of the 30 scintillator bars is detected by an array of four 3×3 mm² Hamamatsu S10931-050P surface mount silicon photomultipliers (SiPMs) [161]. The time resolution of the ST was determined to be 250 ps during the 2016 and 2017 GlueX run periods and thus provided adequate separation of the 250 MHz photon beam bunch structure delivered to Hall D during that time. This performance was achieved using the recommended operating

gain and bias voltages supplied by Hamamatsu to provide both the FADC 250 analog signals and precision F1TDC discriminator signals used in the GlueX reconstruction.

To summarize: The simulation studies in this proposal (see Appendix A5 have assumed a time resolution of 250 ps, which is adequate for the proposed physics program. With the current detector, the overall K_L -momentum resolution will be determined by utilizing the timing information from the ST, BCAL, and TOF detectors and will probably overshoot a very conservative 250 ps specification. Finally, we are exploring potential upgrades to improve the ST time resolution significantly; however, such improvements would not influence much on the resonance parameters extracted by the PWA, hence they have low priority for the proposed hyperon spectroscopy program.

6.2 LH_2/LD_2 Cryogenic Target for Neutral Kaon Beam at Hall D

The proposed experiment will utilize the existing GlueX liquid hydrogen cryogenic target (Fig. 21) modified to accept a larger diameter target cell [162]. The GlueX target is comprised of a kapton cell containing liquid hydrogen at a temperature and pressure of about 20 K and 19 psia, respectively. The 100 ml cell is filled through a pair of 1.5 m long stainless steel tubes (fill and return) connected to a small container where hydrogen gas is condensed from two room-temperature storage tanks. This condenser is cooled by a pulse tube refrigerator with a base temperature of 3 K and cooling power of about 20 W at 20 K. A 100 W temperature controller regulates the condenser at 18 K.

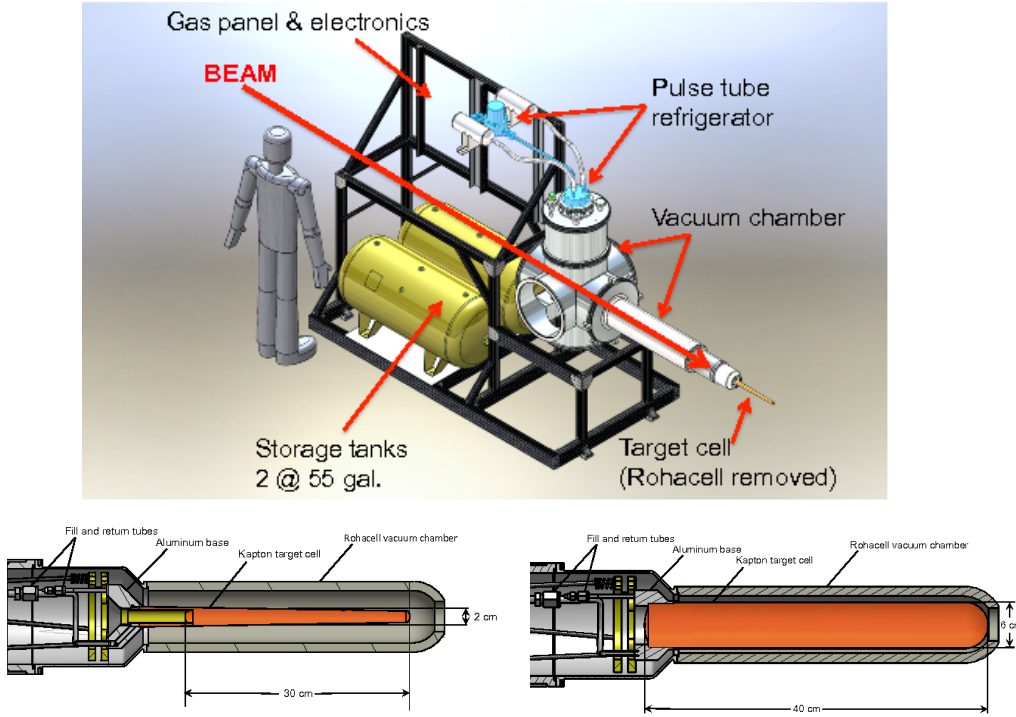


Figure 21: Top: The GlueX liquid hydrogen target. Bottom Left: Kapton target cell for the GlueX LH_2/LD_2 cryogenic target. Bottom Right: Conceptual design for a larger target cell for the proposed K_L beam at Hall D experiment.

The entire target assembly is contained within an “L”-shaped stainless steel and aluminum vacuum chamber with a Rohacell extension surrounding the target cell. The ST for the GlueX experiment fits snugly over this extension. The vacuum chamber, along with the hydrogen storage tanks, gas handling system, and control electronics, is mounted on a custom-built beamline cart for easy insertion into the Hall D solenoid. A compact I/O system monitors and controls the performance of the target, while hardware interlocks on the target temperature and pressure and on the chamber vacuum ensure the system’s safety and integrity. The target can be cooled from room temperature and filled with liquid hydrogen in about 5 hours. For empty target runs, the liquid can be boiled from the cell in about 20 minutes (the cell remains filled with cold hydrogen gas), and then refilled with liquid in about 40 minutes.

The GlueX cell (Fig. 21 (bottom left)) is closely modeled on those utilized at Hall B for more than a decade and is a horizontal, tapered cylinder about 0.38 m long with a mean diameter of 0.02 m. The cell walls are 130 μm kapton glued to an aluminum base. A $\varnothing 0.02$ m reentrant beam window defines the length of LH_2/LD_2 in the beam to be about 0.30 m. Both entrance and exit windows on the cell are 75 μm kapton. In normal operation, the cell, the condenser, and the pipes between them are all filled with liquid hydrogen. In this manner, the liquid can be subcooled a few degrees below the vapor pressure curve, greatly suppressing bubble formation in the cell. In total, about 0.4 liter of LH_2 is condensed from the storage tanks, and the system is engineered to recover this quantity of hydrogen safely back into the tanks during a sudden loss of insulating vacuum, with a maximum allowed cell pressure of 49 psia [163].

A conceptual design for the neutral kaon beam target is also shown in Fig. 21 (bottom right). The proposed target cell has a $\varnothing 0.06$ m and a 0.40 m length from entrance to exit windows, corresponding to a volume of about 1.1 liter, which will require filling the existing tanks on the target cart to about 50 psia. The Collaboration will work with the JLab Target Group to investigate alternative materials and construction techniques to increase the strength of the cell. As an example, the LH_2 target cell recently developed for Hall A is $\varnothing 0.063$ m, 0.18 m long and has a wall thickness of approximately 0.2 mm. The cell is machined from a high-strength aluminum alloy, AL7075-T6, and has a maximum allowed pressure of about 100 psia. It is expected that minor modifications to the cryogenic target’s piping systems will also be required to satisfy the increased volume of condensed hydrogen.

The proposed system is expected to work equally well with liquid deuterium, which condenses at a slightly higher temperature than hydrogen (23.3 K versus 20.3 K at atmospheric pressure). The expansion ratio of LD_2 is 13 % higher, which implies a storage pressure of about 60 psia. Therefore, the new target cell must be engineered and constructed to work with both LH_2 and LD_2 .

7 Expected Results and Beam Time Requirements

Several simulations on various channels were performed to obtain an insight on the expected results and the beam time requirements for precision measurements. The simulations results that follow are based on a 100 days of beamtime with a 1×10^4 K_L /s impinged on a 40 cm long target. Generated events assuming standard beam/target conditions listed in Tables 1 and 2 are processed through a full Geant3-based Monte Carlo (MC) simulation of the GlueX detector [164]. Below we provide a summary of studies performed on various channels for Hyperon spectroscopy. More detailed can be found in Appendix A5.

7.1 Hyperon spectroscopy

For the case of hyperon spectroscopy, a number of channels that are key to studying hyperon resonances was simulated and studied in detail. Specifically, a summary of the simulation results on the following two-body reactions:

1. $K_L p \rightarrow K_S p$,
2. $K_L p \rightarrow \pi^+ \Lambda$,
3. $K_L p \rightarrow K^+ \Xi^0$
4. $K_L d \rightarrow K^+ \Xi^- p_{spectator}$
5. $K_L p \rightarrow K^+ n$.

are presented here (more details can be found in Appendix A5. An analog to the $N\pi$ reactions for the N^* spectra is the $\pi^+ \Lambda$ (and $\pi^+ \Sigma^0$ not shown here) and can provide crucial information on the excited spectrum of hyperons. The study of cascade data allows us to place stringent constraints on dynamical coupled-channel models and identify resonances that do not couple strongly to the $\pi\Lambda$ but decay preferably to a $K\Xi$ channel; analogous to N^* resonances that do not couple strongly to πN but are cleanly seen in $K\Lambda$ and $K\Sigma$ channels. In addition, cascade data on proton and neutron targets provides us with long-sought information on missing excited Ξ states, which can be easily identified and isolated using missing-mass and invariant-mass techniques, and the possibility to measure the quantum numbers of the already established $\Xi(1690)$ and $\Xi(1820)$ from a double-moment analysis. Finally, nonresonant contributions that could interfere with hyperon production amplitudes and distort hyperon signals can also be studied. This is because due to strangeness conservation, formation of intermediate resonances is forbidden in the $K_L p \rightarrow K^+ n$ reaction. Therefore, a detailed study of this reaction provides a clean and controlled way to study and eliminate nonresonant contributions.

The statistical uncertainties obtained after 100 days of running for the differential cross sections of reactions $K_L p \rightarrow K_S p$, $K_L p \rightarrow \pi^+ \Lambda$, and $K_L p \rightarrow K^+ \Xi^0$ are show in Fig. 22. The proposed experiment will allow us to reconstruct about 2.7M $K_S p$ events in the $K_S \rightarrow \pi^+ \pi^-$ channel, allowing an unprecedented and detailed investigation of the cross section ambiguities evident in

existing results. Furthermore, the proposed experiment will significantly improve measurements of $K_L p \rightarrow \pi^+ \Lambda$ and $K_L p \rightarrow K^+ \Xi^0$ as illustrated by the uncertainties in Fig. 22.

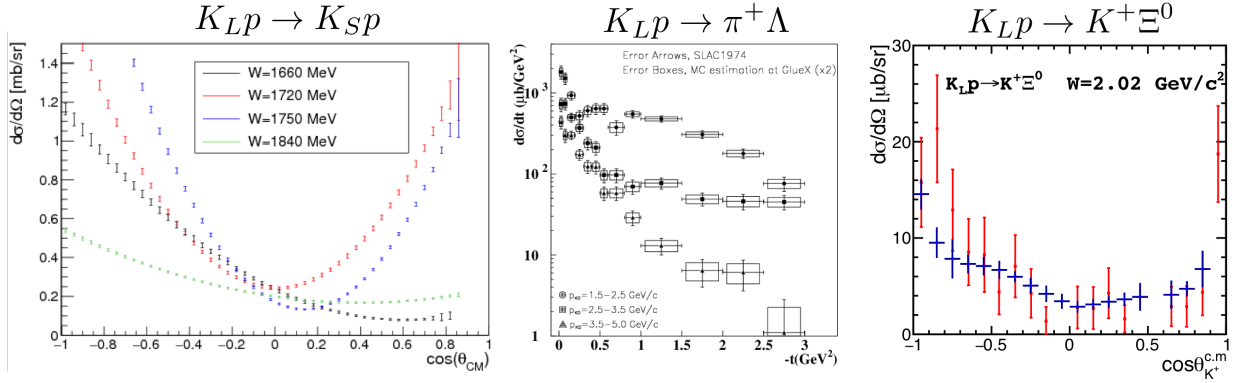


Figure 22: Differential cross sections for reactions 1, 2, and 3 exclusively reconstructed illustrating the statistical uncertainties after 100 days of running. Left panel: Cross sections of $K_L p \rightarrow K_S p$ binned in various W bins as a function of the center of mass angle (one can compare to existing data from Ref. [165]). Middle panel: Differential cross section for various kaon momentum bins as a function of t for $K_L p \rightarrow \pi^+ \Lambda$. The boxed errors indicate the statistical uncertainty increased by a factor of 2 after 100 days of running as compared to existing uncertainties [134]. Right panel: Cross section of $K_L p \rightarrow K^+ \Xi^0$ reconstructed exclusively for a specific W bin as a function of the kaon angle. The uncertainties after 100 days of running are shown with blue error bars and are compared to the existing results (red error bars) [166].

Utilizing the large self-analyticity of hyperons through their parity violating weak decay, one can easily determine the hyperon induced polarization by studying the angular distribution of the hyperon decay products. Such measurements place further stringent constraints on the underlying dynamics and are shown to be an invaluable tool in identifying PWA amplitudes. Figure 23 shows the two-fold differential induced polarisation and the statistical uncertainties obtained after 100 days of running for $K_L p \rightarrow \pi^+ \Lambda$ (left) and $K_L p \rightarrow K^+ \Xi^0$ (right). The proposed experiment will increase significantly the kinematic coverage of available results and provide a statistical improvement by at least of factor of 2 on existing measurements.

An analysis of generated polarization data from the reaction $K_L n \rightarrow K^+ \Xi^-$ using models described in Sec. 4.9 indicate that with 100 days of beamtime the expected statistical uncertainties allow a clear identification between the two available models, which give very different predictions. The left panel in Fig. 24 illustrates the expected two-fold differential results on the induced cascade polarization (Ξ^-) after 100 days of running using generated data from the two model predictions. The expected statistical significance for the model separation at the same W -bin as a function of experiment duration is shown in the right panel. The right panel indicates that a 100 days experiment would reach a decisive level of 7.6σ separation power, compared to only a 3.5σ separation after 20 days.

The spectrum of excited cascades is barely known and practically nothing is known about their quantum numbers. Detailed studies utilizing generated data was performed to investigate the dis-

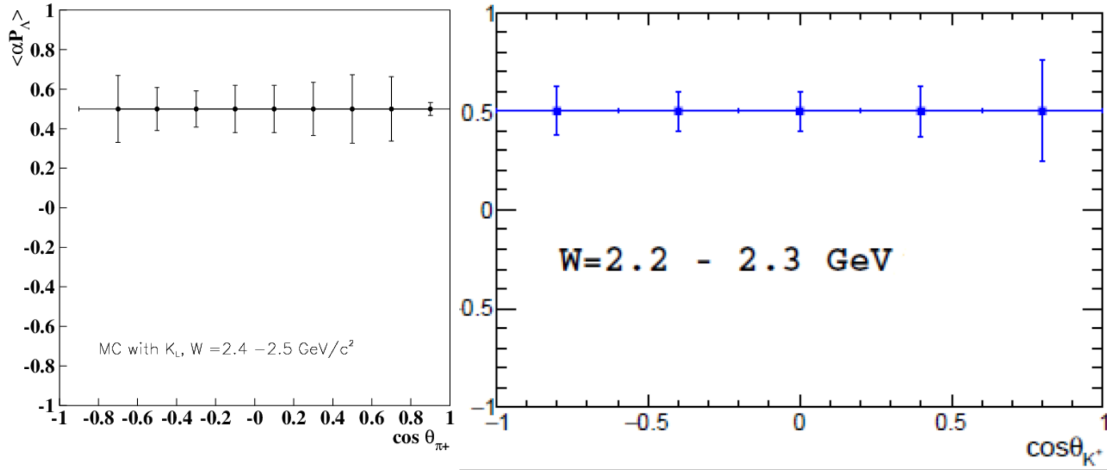


Figure 23: Two-fold differential results on the induced polarization of Λ (left) and Ξ^0 (right) from $K_L p \rightarrow \pi^+ \Lambda$ and $K_L p \rightarrow K^+ \Xi^0$ after 100 days of running.

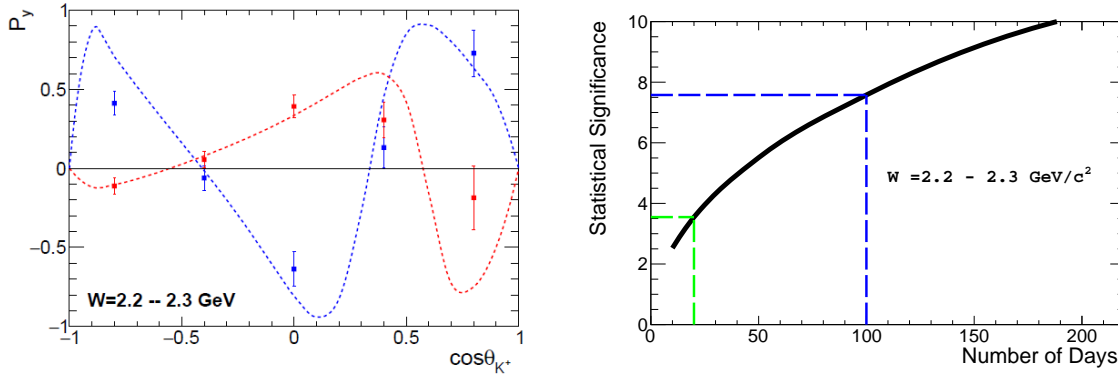


Figure 24: Left panel: Estimated statistical uncertainties of the induced polarization of the Ξ^- in a $K_L n \rightarrow \bar{K}^+ \Xi^-$ reaction as a function of CM $\cos \theta_{K^+}$ (two-fold differential). The curves show the theoretical predictions based on two solutions as described in Sec. 4.9. Right panel: Expected statistical significance, in units of σ s, to distinguish two models as a function of the running time. Two benchmark cases of 20 and 100 days are highlighted by the dashed green and blue curves, respectively.

covery potential achievable at KLF including measurements on the neutron. The left panel of Fig. 25 shows the production cross sections that will be measurable at KLF with 100 days (blue) and 20 days (green) of running considering a 10 % statistical uncertainty and a branching ratio ¹ $Br(\Xi^* \rightarrow \bar{K} \Lambda) = 1$. The right panel shows the lowest measurable $\Xi^* \rightarrow \bar{K} \Lambda$ branching fraction at KLF as a function of experiment duration indicating the lowest measurable branching ratios at 20 and 100 days.

100 days of running allows us to study the several Ξ^* states even with somewhat suppressed $\Xi^* \rightarrow$

¹From BNL measurements given in Ref. [167] the Ξ^{*-} production cross section should be on the order of $1 - 10 \mu b$ and the higher Ξ^* mass the lower the cross section, from $3.7 \mu b$ for the $\Xi^*(1820)$ to $1 \mu b$ for the $\Xi^*(2500)$.

$\bar{K}\Lambda$ decay of heavy Ξ^* 's². A W -variation of the Ξ^* production cross-section provide and important information on $\Xi^* \rightarrow \bar{K}\Lambda^*$ and $\Xi^* \rightarrow \bar{K}\Sigma^*$ couplings as an inverse process allowing further insight into Ξ^* internal structure.

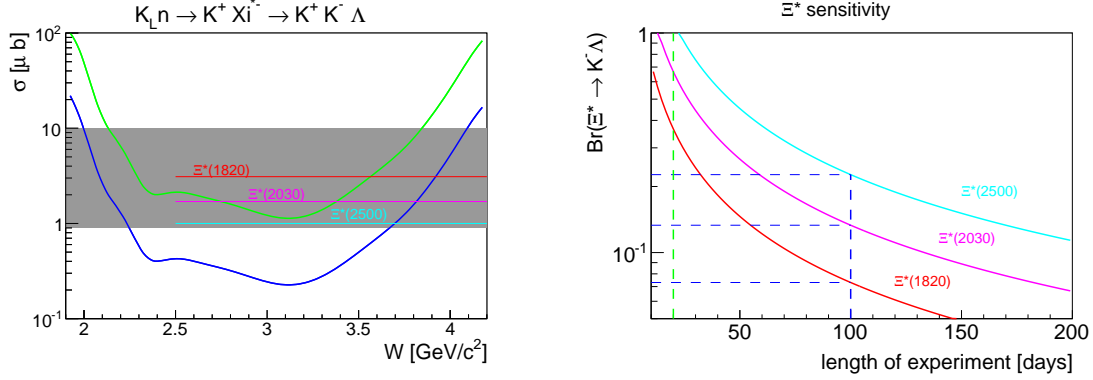


Figure 25: Left panel: Ξ^* discovery potential achievable at KLF during the 100 (blue) and 20 (green) day experiment, under assumption of 10 % statistical accuracy and $Br(\Xi^* \rightarrow \bar{K}\Lambda) = 1$. The gray band corresponds to typical Ξ^* cross sections and horizontal lines are few examples of BNL cross sections from Ref. [167] Right panel: Estimation of lowest measurable $\Xi^* \rightarrow \bar{K}\Lambda$ branching fraction at KLF as a function of experiment duration at $W \sim 3.1 \pm 0.025$ GeV. Two benchmark cases of 100 (20) days are highlighted by dashed blue (green) curves.

Finally, the nonresonant reaction $K_L p \rightarrow K^+ n$, can be studied in a clean and controlled way and one can use this to identify nonresonant contributions to the hyperon production amplitudes. In 100 days of beamtime, we expect to detect ~ 60 M events significantly improving the statistical significance of existing measurements [168, 169] and provide precision measurements in the energy range $2 < W < 3.5$ GeV where there are no data on this reaction at all.

7.2 Expectations for Λ^* and Σ^* Spectroscopy via a $K^+\Xi$ PWA

The observation of Λ^* and Σ^* hyperons at KLF will require a coupled-channel PWA using the measured differential cross sections and recoil observables, which have been simulated in Sec. 4. The resonance poles in the complex energy plane will be used to confirm previously observed states and identify new Λ^* and Σ^* resonances in the hyperon spectrum (see Appendix A3).

The existing $K_L p$ database is so poor that PWAs of individual $K_L p$ -induced reactions may not be possible based on currently available data (Appendix A2). In particular, there are no $K_L p \rightarrow K^+ \Xi^0$ polarization data available and there is only one energy for the $K_L p \rightarrow \pi^+ \Lambda$ reaction with both $d\sigma/d\Omega$ and polarization data. Our proposal does not consider the use of a polarized target at this stage and, for that reason, we will be able to measure polarization data for recoil observables only. Overall, one certainly cannot perform a reliable PWA for reactions in which only $d\sigma/d\Omega$ data are available. The existing $K_L n$ database is nonexistent.

²The $\Xi^* \rightarrow \bar{K}\Lambda$ is “dominant” for many Ξ^* states according to PDG2018 [3]

To estimate the impact that new K_L measurements will have on fits, we have carried out a study $K_L p \rightarrow K^+ \Xi$ reaction. Using the recent BnGa solution [170, 171], we generated pseudodata for the $K_L p \rightarrow K^+ \Xi$ reaction: $d\sigma/d\Omega$ and recoil polarization P . The pseudodata were generated for our worse case of statistics for a $K_L p \rightarrow K^+ \Xi^0$ binning of 20 MeV in CM energy W and $\theta = 5$ (10) 175° for $d\sigma/d\Omega$ and $\cos \theta = -0.8$ (0.4) 0.8 for P . A series of global fits were obtained using settings associated with 20 and 100 days of running time within BnGa framework.

The simulated solution was obtained from the fit of the $K^- p \rightarrow K \Xi$ data using the K-matrix fit which included all 3 and 4 star Λ and Σ -hyperons [3] and an additional Σ state needed to fit the data. The quantum numbers of this state were found to be $5/2^-$ and its mass is located just above 1900 MeV. This fit also showed a notable deviation for the pole position of the $\Sigma(2030)7/2^+$ state from the PDG2018 value (Table 4). The data from the $K_L p$ collision where only Σ hyperons are produced can provide a crucial information which can confirm or reject this solution.

The data simulated as 20 and 100 days of the data taken were fitted as a sum of the Breit-Wigner states. Although 20 day data set allowed us to reproduce the quantum numbers of the all contributions from the simulated solution the properties of the $\Sigma(1920)5/2^-$ and $\Sigma(2030)7/2^+$ hyperons were defined with large uncertainties. The mass of the $\Sigma(1920)5/2^-$ state was found to be notably higher than that used in the simulation (Table 4). The fit of the 100 day data sets solve all the mentioned above problem. The masses and the widths of the simulated states were found to be much close to those simulated in the solution and with much smaller errors. The fit of the 100 day data sets allowed us to define with much larger accuracy the couplings of the fitted states into $K \Xi$ channel.

An example of the fit results for $d\sigma/d\Omega$ and P for 20 and 100 days settings together with 100 days pseudodata are shown on Fig. 26. To illustrate the effect for 20 (100) days data taking on resonance parameters we plot the total cross section for two prominent Σ^* states: $\Sigma(1920)5/2^-$ and $\Sigma(2030)7/2^+$, see Fig. 27.

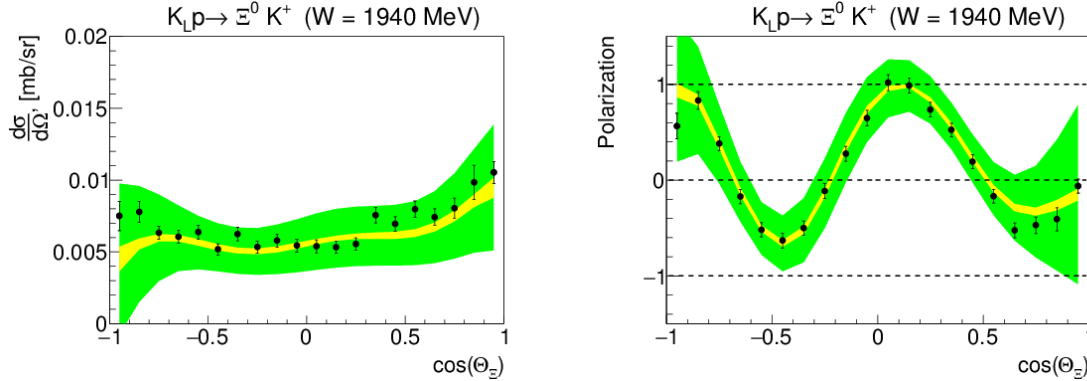


Figure 26: Two examples ($W = 1940$ MeV) showing the impact of the proposed data on the BnGa solutions. The green (yellow) hatched band indicates the present uncertainties for 20 (100) days of running time. The solid black points corresponds to the pseudodata. $d\sigma/d\Omega$ on the left and P on the right panels.

The new measurements, specifically the 100 days of running time case will significantly reduce the uncertainties of the observables. The total angular resolution will therefore be greatly improved,

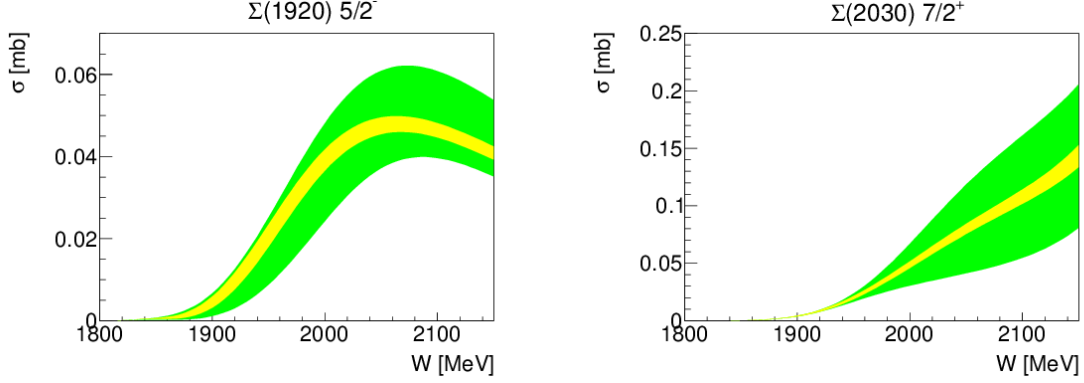


Figure 27: Resulting effect of 20 (green) and 100 (yellow) days of running time on two Σ^* resonances within BnGa PWA solution. $\Sigma^*(1920)5/2^-$ (left) and $\Sigma^*(2030)7/2^+$ (right).

which will enhance the possibility of determining the number of amplitudes that are involved. With this greater understanding of these observables, effects of higher-spin resonances can be investigated.

From the PWA of $K_L p \rightarrow K^+ \Xi$, we extracted Breit-Wigner resonance parameters for two example states in the Σ^* spectrum, $\Sigma(1920)5/2^-$ and $\Sigma(2030)7/2^+$. The mass and width parameters are shown in Table 4 under the 20- and 100-day scenarios. The precision of the resonance parameters significantly deteriorates in a 20-day scenario. With 100 days of running time we could reach a precision level comparable to modern results of the SAID πN PWA [172].

Resonance	20 days: M, Γ	100 days: M, Γ	PDG2018: M, Γ	LQCD: M
$\Sigma(1920)5/2^-$	$1977 \pm 21 \pm 25$ $327 \pm 25 \pm 25$	$1923 \pm 10 \pm 10$ $321 \pm 10 \pm 10$		2027 2487 2659 2781
$\Sigma(2030)7/2^+$	$1981 \pm 30 \pm 30$ 350 ± 80	$1930 \pm 20 \pm 30$ 400 ± 40	2030 ± 10 180 ± 30	2686 2709 2793 2806

Table 4: Comparison of masses and widths (in MeV units) of simulated values with PDG2018 [3] and LQCD [30] predictions.

To summarize: With 100 days of running time, we can provide a reliable solution for all the resonances having elastic branching ratios larger than 4 %, at least up to $l = 4$. With 20 days of beamtime, we could only carry out simple “bump-hunting” - an identification of well-defined and well-separated resonances with regular shapes. All irregular cases (e.g., molecular states with skewed shapes and complex energy-dependent-widths, threshold-effects, multiple interferences, etc.) and all the exotic states that are predicted to populate the hyperon spectrum will require high-precision polarization observables on the order of 0.1 or better to be identified. From our $K^+ \Xi$ PWA study, we can infer that the precision of resonance parameters extracted from PWA of KLF data for the higher-mass Λ^* and Σ^* states we propose to measure will deteriorate without sufficient running time. The spectrum of excited Λ^* and Σ^* states is expected to be densely populated with

typical mass differences of about 100 MeV for states with the same quantum numbers [3]. Therefore to disentangle the spectrum of observed hyperon states, we require sufficient precision for the extracted mass and width parameters, provided by the proposed 100 days of running time.

7.3 Expected results in Strange Meson Spectroscopy

The $K\pi$ scattering has two possible isospin channels, $I = 1/2$ and $I = 3/2$. For S -wave scattering, both are significant below 2 GeV, whereas the P -wave $I = 3/2$ is almost negligible. Below 1 GeV the P -wave is basically a narrow elastic wave peaking at 892 MeV, interpreted as the $K^*(892)$ resonance, whereas a second resonance, the $K_1^*(1410)$ exists above 1 GeV, although its properties are less precisely known. The $I = 3/2$ S -wave is elastic and repulsive up to 1.7 GeV and contains no known resonances. The P -wave $I = 3/2$ has been measured in Ref. [124] and is also repulsive but very small. However, the $I = 1/2$ S -wave has a peaking broad resonance above 1350 MeV, interpreted as $K_0^*(1430)$. In addition, some phenomenological [94–98, 173–178] and experimental [179, 180] studies require the presence of a resonance with a very large width, called κ (kappa), or $K_0^*(800)$, in the region close to the $K\pi$ threshold.

Most of the experimental studies of the $K\pi$ system have been performed by experiments with kaon scattering beam off nucleons. This is related to the high cross section of the $K\pi$ system production with this processes. For example, the cross section of the $K^*(892)$ resonance, produced in the reaction $K^-p \rightarrow \bar{K}^0\pi^-p$ at 2.1 GeV/c [181], is 1.34 ± 0.08 mb. In case of a neutral kaon beam, the equivalent reaction to the process $K^-p \rightarrow K^{*-}(892)p$ is the kaon beam scattering $K_L p \rightarrow K^{*0}(892)p$. Therefore, the production of the $K\pi$ system, using the K_L facility, can provide an adequate environment for studying the strange meson states. More details about a simulation study are in Appendix A6).

7.3.1 Impact on P -Wave Phase-Shift Study

The pion exchange in the hadro-production mechanism of $K^{*0}(892)$ occurs mostly at low $-t$, thus we can have access to the amplitude scattering of $K^0\pi^0 \rightarrow K^+\pi^-$, as illustrated in Fig. 9. Using the resolutions and efficiencies from our simulations, we can estimate the improvement that can be made on the scattering amplitude analysis of $K\pi \rightarrow K\pi$. The range of $-t$ that will be used in this comparison will be $[0.14, 0.2]$ GeV² to ensure that the t efficiency is uniform. The efficiency of this t range selection is $\epsilon_\pi = 17.85\%$. The expected number of events in this case is 2×10^6 . The study of the $K\pi$ P -wave phase-shift is mainly used to extract the vector form factor $f_\pm(t)$ [182], where t is the four-momentum transfer. The vector form factor, at the optical point $f_+(0)$, has an impact on the measurement of the CKM matrix element V_{us} [128, 182], where the precision on this measurement plays an important role on probing the physics beyond the Standard Model. The phenomenological studies [128, 182] analyzed the $K\pi$ P -wave phase-shift produced by Belle Experiment [127] using the decay $\tau \rightarrow K\pi\nu_\tau$ and LASS data [122, 124] using the scattering reaction $K^-p \rightarrow K^+\pi^-n$. We can evaluate the improvement that can be performed by KLF in these type of studies. The comparison is made to the LASS results [122] which is a similar scattering reaction study but with charged kaon beam presented in Fig. 28 (left panel). The

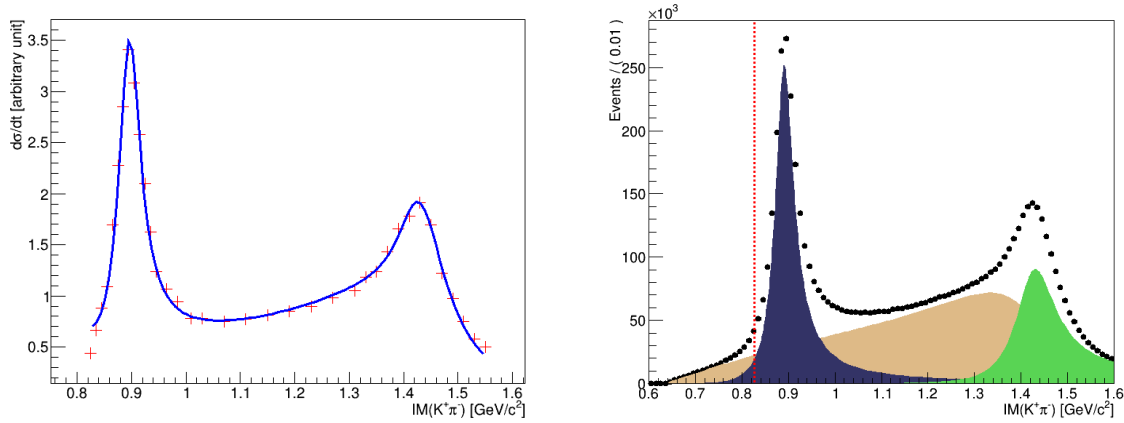


Figure 28: Left panel: Cross section of $K^-p \rightarrow K^+\pi^-n$ as a function of the invariant mass from LASS results [122]. The blue line is the fit to the cross section using composite model containing two RBW, spin-1 and spin-2, and S -wave LASS parameterization. Right panel: Expected distribution of the $K^+\pi^-$ invariant mass below 1.6 GeV from KLF after 100 days of run. The dark blue function represents the $K^+\pi^-$ P -wave, light brown the S -wave and green the D -wave. The dashed line represents the threshold of $K\pi$ invariant mass in LASS results [122].

resulting model from the fit to LASS amplitude is used to simulate the distribution of the invariant mass of $K^+\pi^-$ P -wave with KLF.

7.3.2 $K\pi$ S -Wave and Kappa Investigation

S-wave and D-wave Production in $K_Lp \rightarrow K^+\pi^-p$

The $K\pi$ S -wave scattering, below 2 GeV, has two possible isospin channels. The 1/2 isospin S -wave contains two resonances, κ and $K_0^*(1430)$, both of them are not well defined. In 3/2 S -wave no resonance is found. So far, the available data used to study the dynamics of the S -wave are LASS data [122, 124]. The $K\pi$ P -wave and D -wave are well defined with one resonance $K^*(892)$ as vector meson and one resonance $K_2^*(1430)$ as tensor meson. The simulation of the reaction $K_Lp \rightarrow K^{*0}(892)p \rightarrow K^+\pi^-p$ in KLF can be used to estimate the total production rate of the different $K\pi$ waves. Fig. 28 (left panel) shows the fit to the cross section of LASS results. We expect $N_S = 3.5 \times 10^6$ events, after 100 days KFL-run, for the S -wave production and $N_D = 1.2 \times 10^6$ for the D -wave. The total 100 days production statistics for the $K^+\pi^-$ system is expected to be $\approx 7 \times 10^6$ events for the S , P , and D -waves combined. This production includes 1/2 and 3/2 isospin and represent about 50 times the dataset collected by LASS experiment [122].

Fig. 28 (right panel) shows the expected $K^+\pi^-$ invariant mass distribution produced by the reaction $K_Lp \rightarrow K^{*0}(892)p \rightarrow K^+\pi^-p$ in KLF.

It has to be noted that especially in the region below 0.75 GeV with the new data we expect to have a dramatic improvement, not only due to the very high statistics, but also because LASS did not provide any data below 0.75 GeV. These data are therefore very relevant for the extraction of the

scalar scattering lengths that will test the predictions and convergence of SU(3) Chiral Perturbation Theory. Moreover, the rigorous variable for analytic continuation to the complex plane is s , and due to the large width of the κ , the real part of the κ pole position in the s -plane is $\text{Re}(M_\kappa - i\Gamma/2)^2 \simeq (M_\kappa^2 - \Gamma^2/4) \simeq 0.39 \text{ GeV}^2$, much closer to threshold $s_{th} \simeq 0.40 \text{ GeV}^2$ than to its nominal mass $M_\kappa^2 \simeq (0.682)^2 \text{ GeV}^2 \simeq 0.465 \text{ GeV}^2$, which makes the determination of the pole especially sensitive to the threshold region and thus the KLF low-energy results are of even greater relevance.

Kappa Investigation

The κ or $K_0^*(800)$ meson is a 0^+ resonance with strangeness. The pole of this resonance is found in the $K\pi$ S -wave with isospin $1/2$. In case of neutral kaon scattering off proton producing a $K\pi$ system with neutral or charged exchange, the S -wave final state is composed of the two isospin components $1/2$ and $3/2$. Therefore if possible, splitting the two components to study the pole of the κ meson would be very important. It should be noted that this separation was not performed for LASS. Actually, the existing $I = 3/2$ data are previous to LASS and of much less precision, which is a large source of uncertainty that contaminates the extraction of the $I = 1/2$ amplitude and the κ or other strange resonance poles.

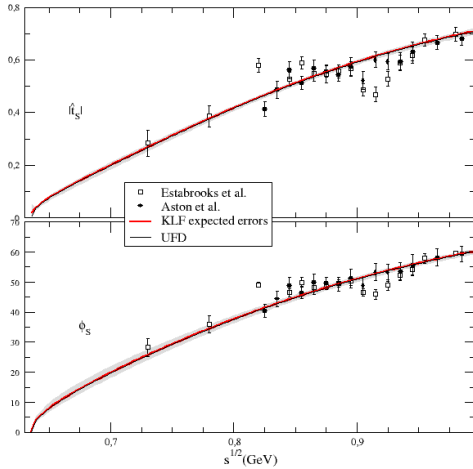


Figure 29: Plot produced by the authors of Ref. [111]. Data from LASS results [122, 124]. The upper panel shows the S -wave $K\pi$ amplitude in the $(S^{I=1/2} + S^{I=3/2})/2$ combination of isospin that was actually measured, whereas the lower one shows the phase-shift, which was measured independently. The continuous line is the unconstrained fit from Pelaez and Rodas dispersion relation study [111], whose uncertainties are covered by the gray band. For comparison, the red lines represent the fit to the amplitude of LASS scaled by the expected KLF production during 100 days of run, whose corresponding uncertainties are delimited by the red band. Note that there are no data below 0.725 GeV.

The following evaluations are based on the assumption that KLF will produce high statistics data in a combined isospin $3/2$ and $1/2$ states.

From the Monte Carlo simulations, we expect that the dataset produced by KLF with each charged final state reactions $K^+\pi^-$ and $K^-\pi^+$ will be about 50 times larger than the LASS dataset [122]. In Fig. 29, we have redrawn a figure taken from Ref. [111] and we show the fit to the amplitude in that dispersion relation study, but now also including as a red line and a red band the fit to LASS amplitudes [122] scaled by the precision that will be produced by KLF after 100 days of run. The present systematic effects have already been included in the red band.

There are many *models* describing the $\kappa/K_0^*(800)$ and its associated pole (see the PDG2018 [3] for an exhaustive compilation). For illustration we show some representative results in Fig. 30. Note that many of them still use Breit-Wigner parameterizations, which unfortunately are not applicable

in this case because they violate chiral symmetry and do not have the left and circular cuts that are numerically relevant for precise determinations of the κ pole.

The other analyses, we list in Table 5 are: a model of a T-matrix pole [183] and more sophisticated models including some implementation of chiral symmetry [108, 184], but still with some model dependence that is not included in their uncertainties. We also show a dispersive evaluation [178], where the difficult left and circular cut contributions have been approximated with some assumptions (like a cut-off), but with very conservative systematic uncertainties. In addition, we show two extractions of the pole, one exploiting the analyticity in the whole complex plane by means of a conformal expansion [111] and another one using Padé approximants to extract the pole parameters from local information of the amplitude near the pole without assuming a specific parameterization [118]. Both of them use as input a fit to data constrained with Forward Dispersion Relations and their uncertainties include an estimate of systematic effects. Other determinations in the literature, not shown here, are usually based on models and often quote uncertainties that do not include systematic effects.

Finally, as already commented, the most rigorous determination of the κ pole with a realistic estimate of both statistical and systematic uncertainties, can be made by means of Roy-Steiner Dispersion Relations. There is actually such an estimate of the pole [24], although it does not use data on the scalar wave below 1 GeV. Actually, the scalar partial waves in that region are obtained as solutions of the Roy-Steiner equations with input from other waves and higher energies. In this sense, the κ pole and the whole low-energy region in Ref. [24] are a prediction, not a determination from data.

Reference	Pole (MeV) $\sqrt{s_\kappa} \equiv M - i\Gamma/2$	Comment
Bonvicini [183]	$706.0 \pm 24.6 - i 319.4 \pm 22.4$ MeV	T -matrix pole model from CLEO
Bugg [184]	$663 \pm 42 - i 342 \pm 60$ MeV	Model with LO Chiral symmetry
Pelaez [108]	$753 \pm 52 - i 235 \pm 33$ MeV	Unitarized ChPT up to NLO
Conformal CFD [111]	$680 \pm 15 - i 334 \pm 8$ MeV	Conformal parameterization from dispersive fit
Padé [118]	$670 \pm 18 - i 295 \pm 28$ MeV	Analytic local extraction from dispersive fit
Zhou <i>et al.</i> [178]	$694 \pm 53 - i 303 \pm 30$ MeV	partial-wave dispersion relation. Cutoff on left cut.
Descotes-Genon <i>et al.</i> [24]	$658 \pm 13 - i 279 \pm 12$ MeV	Roy-Steiner prediction. No S-wave data used below 1 GeV.
Pelaez-Rodas HDR [21, 185]	$663 \pm 14 - i 288 \pm 27$ MeV	Roy-Steiner analysis of scattering data
KLF expected errors	$663 \pm 6 - i 288 \pm 5$ MeV	As previous line but with KLF expected errors

Table 5: Illustrative values of $\kappa/K_0^*(800)$ -pole determinations from models (Lines 2 to 7). Line 8 is a model independent prediction from a dispersive analysis without using S -wave data below 1 GeV. We also compare in the last two lines the model independent extraction using present data versus the extraction using the expected KLF data.

Thus, in order to estimate the effect of the proposed KLF experiment, we have recalculated the pole obtained by using a Roy-Steiner analysis either using all the existing data [21, 185] or with the LASS data rescaled to the expected accuracy of the KLF experiment. In the first case, without KLF, we find $M_\kappa \simeq 663 \pm 14$ MeV and $\Gamma_\kappa = 596 \pm 53$ MeV, whereas by rescaling the LASS data with the expected KLF precision the uncertainties are divided by slightly more than a factor of two for the mass, to find: $M_\kappa \simeq 663 \pm 6$ MeV; and by a factor of five for the width, finding: $\Gamma_\kappa = 596 \pm 10$ MeV. According to these results, just by rescaling the statistics, a significant

improvement on κ search can be performed by KLF, especially at the elastic region of the $K\pi$ invariant mass. Fig. 30 shows as pole positions in the complex plane, the different determinations of the κ mass and width, that we have just described, including the determination with the expected amplitude and phase-space that will be produced by KLF after 100 days of run. The expected result for the kappa pole is $\sqrt{s_\kappa} \equiv M - i\Gamma/2 = 663 \pm 6 - i288 \pm 5$ MeV (the error coming from πK scattering is less than 1 MeV, the rest comes basically from the high energy Regge input to the dispersive integrals).

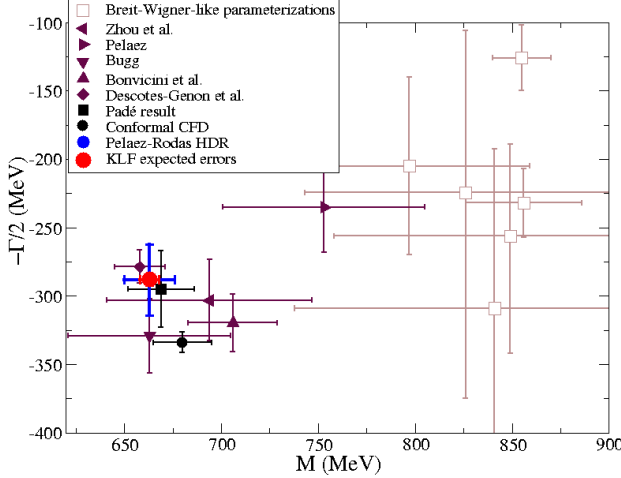


Figure 30: Present situation of the determinations of the κ pole. The figure is from Ref. [21, 185] but we have added as a red point with uncertainties, the simulation of the pole position that would be obtained by means of a Roy-Steiner analysis when fitting to the amplitude and phase-shift of LASS, but scaled by the precision that will be produced by KLF experiment after 100 days of run. This calculation also include estimates of systematic effects. Note that the other points are either predictions [24] or illustrative models that may have additional systematic uncertainties due to their model dependence, like Breit-Wigner determinations.

To summarize: The KLF proposal will have a very significant impact in our knowledge of πK scattering amplitudes in the scalar $I = 1/2$ -channel. First, it will certainly improve the still conflictive determination of the $K_0^*(1430)$ parameters. Second, it will help to lower the tension between phenomenological dispersive determinations of scattering lengths from data versus those from Chiral Perturbation Theory and lattice QCD. Finally, and more importantly, it will reduce by more than a factor of two the uncertainty in the mass determination of the controversial κ or $K_0^*(800)$ and by a factor of five the uncertainty on its width (and therefore on its coupling). Thus it will settle the debate on its existence, and the existence of a light scalar nonet, as well as on its nature as a non-ordinary state beyond the quark model. The reduction of uncertainties by a factor of two on the mass and of five on the width are guaranteed just by the large statistical sample of KLF compared to the LASS.

The additional reductions could be expected from the fact that KLF will be able to measure the amplitude at much lower center of mass energies, closer to the threshold.

It has to be mentioned that in the LASS experiment with charged kaon beam, with fixed strangeness, and charged final state $K^-\pi^+$ only one isospin state could be produced, while in the proposed experiment with KL Facility, the neutral kaon beam scattering on both proton and neutron targets at low t -Mandelstam will allow to produce and identify all four isospin partners of $K_0^*(800)$.

7.4 Expected Statistical Accuracy

A coupled-channel PWA is the most direct and least model-dependent way to extract resonance properties. However, as shown in Sec. 7.2, it requires knowledge of both the differential and polarization observables at the same CM energy. In order to ensure that the duration of the experiment would be adequate to extract all observables with sufficient accuracy, dedicated studies were performed. One can determine the recoil polarization utilizing large self-analysing powers of hyperon decays. In this case, the errors on the polarization measurement are essentially of statistical nature, hence one can infer desired accuracy in the polarization measurement to a required beam time of experiment in a straightforward way. From theoretical perspective, the polarization error on the order of 0.1 looks essential in getting unambiguous PWA solution (see Sec. 7.2). Polarization errors larger than 0.5 would have no influence on convergence of the PWA fit, hence will be discarded. This tight theoretical constraints impose strict requirement for the duration of experiment to collect sufficient statistics in each channel. Fig. 31 shows the expected error in measurement of polarization observable as a function of CM energies (left) and experiment duration (right) for the key reaction $K_L p \rightarrow K^+ \Xi^0$. The expected error is a complex three-fold function of kaon flux (Fig. 17(left)) with maximum at $W = 3$ GeV), cross section (Ref. [166]) and detector acceptance (Fig. 57). In case of $K_L p \rightarrow K^+ \Xi^0$ reaction, it lead to a maximum statistics reachable in the range of $2.2 < W < 2.7$ GeV.

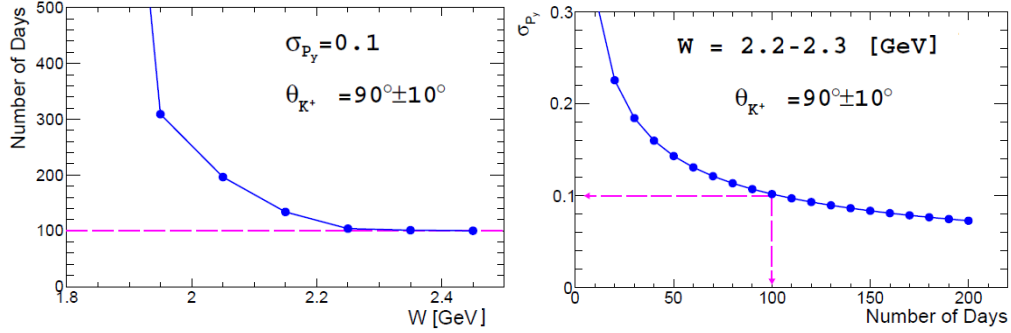


Figure 31: Required a beam time of the experiment for the $K_L p \rightarrow K^+ \Xi$ reaction. Left panel: To reach 10 % polarization uncertainty as a function of W . Right panel: Reachable polarization uncertainty at $W = 2.2$ GeV and $\theta_{K^+} = 90^\circ$.

A similar study can be performed for the another reaction channel, $K_L p \rightarrow \pi^+ \Lambda$, see Fig. 32.

This reaction requires finer binning to disentangle various $\Lambda - \Sigma$ mixing effects leading to a similar experiment duration as in $K\Xi$ case, despite larger production cross sections.

To summarize: All channels we have considered so far require about 100 days beamtime for a nominal flux of 10^4 K_L /s to exhibit the beauty of strangeness physics in details and maximize the discovery potential of the KL Facility.

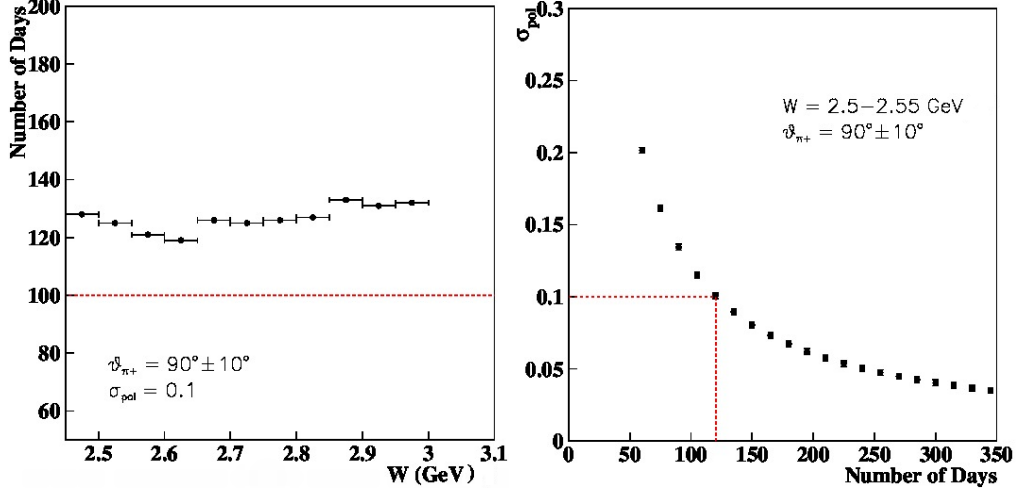


Figure 32: Required a beam time of the experiment for the $K_L p \rightarrow \pi^+ \Lambda$ reaction. Left panel: To reach 10 % polarization uncertainty as a function of W . Right panel: Reachable polarization uncertainty at $W = 2.525 \text{ GeV}$ and $\theta_{\pi^+} = 90^\circ$.

7.5 Expected Systematic Uncertainties

Systematic uncertainties with K_L beam will be reaction and kinematics dependent. The total systematic errors include three major sources: detector related, induced by the reconstruction algorithms, and overall flux estimation. The first two sources can be linked to the current GlueX program. Indeed after several years of running our understanding of the GlueX detector performance is in quite advanced state. The K_L program will utilize this knowledge. Hence, we expect the detector related systematical errors to be of the similar size to that of the photon program and below $\approx 3 \%$ [6]. The only source of uncertainty which cannot be estimated from ongoing GlueX program is K_L flux related ambiguity. A dedicated K_L Flux Monitor will be able to provide a flux determination with an accuracy better than 5 %.

Additional source of systematical uncertainties in the determination of resonance parameters is related to theoretical extraction of “true” observables from experimental data. Theoretical uncertainty is two-folded: the first part related to the absence of experimental data, e.g., the absence of polarization observables, or non-existence of measurements on neutron target; the second one is associated with particular theoretical methods employed to extract resonance parameters. We, in KLF, will attack this problem from both directions: precise experimental measurements will cover gaps in existing database, while comprehensive theoretical analysis of competing theoretical groups (SAID, BnGa, GW-Juelich, MAID, or Kent State) with uncorrelated method-dependent systematics will eliminate the second source of uncertainties.

Systematic uncertainties for the pole position of the κ from $K\pi$ scattering have already been taken into account in the estimation of the precision for its mass and width.

8 Summary and Beam Time Request

We propose to perform strange hadron spectroscopy with a secondary K_L beam in the GlueX setup at JLab. Precise new experimental data (both differential cross sections and recoil polarization of hyperons) for $K_L p$ scattering with good kinematic coverage will be obtained. This will allow predictions from the CQM and LQCD to be checked for all families of excited Λ^* , Σ^* , Ξ^* , and Ω^* hyperon resonances for the first time. In addition, it will permit a search for the possible existence of hybrids in the hyperon sector as predicted by the lattice calculations [57].

A complete understanding of three-quark bound states requires accurate measurements of the full spectra of hyperons with their spin-parity assignments, pole positions, and branching ratios. An important impact of these strange hyperon spectroscopy measurements is their significance for the thermodynamic properties of the early universe at freeze-out, which is one of the main physics topics at heavy-ion colliders.

Besides hyperon spectroscopy, the experimental data obtained in the strange meson sector in the reactions $K_L p \rightarrow K^\pm \pi^\mp p$ and $K_L p \rightarrow K_S \pi^\pm n(p)$ will provide precise and statistically significant data for experimental studies of the $K\pi$ system. This will allow a determination of quantum numbers of strange meson resonances in S- (including $\kappa(800)$), P-, D-, and higher-wave states. It will also allow a determination of phase shifts to account for final-state $K\pi$ interactions. Measurements of $K\pi$ form factors will be important input for Dalitz-plot analyses of D -meson and charmless B mesons with $K\pi$ in final state.

The K_L facility at JLab will be *unique in the world*. The high-intensity secondary beam of K_L (1×10^4 K_L/s) would be produced in EM interactions using the high-intensity and high-duty-factor CEBAF electron beam with very low neutron contamination as was done at SLAC in the 1970s; but now, with three orders of magnitude higher intensity [134]. The possibility to perform similar studies with charged kaon beams is under discussion at J-PARC with intensities similar to those proposed for the K_L beam at JLab. If these proposals are approved, the experimental data from J-PARC will be complementary to those of the proposed K_L measurements.

Reaction	Statistics (events)
$K_L p \rightarrow K_S p$	2.7M
$K_L p \rightarrow \pi^+ \Lambda$	7M
$K_L p \rightarrow K^+ \Xi^0$	2M
$K_L p \rightarrow K^+ n$	60M
$K_L p \rightarrow K^- \pi^+ p$	7M

Table 6: Expected statistics for differential cross sections of different reactions with LH_2 and below $W = 3.0$ GeV for 100 days of beam time.

In Table 6, we present the expected statistics for 100 days of running with a LH_2 target in the GlueX setup at JLab. The expected statistics for the 5 major reactions are very large. There are however, two words of cautions at this stage. These numbers correspond to an inclusive reaction reconstruction, which is enough to identify the resonance, but might not be enough to uncover its

nature. The need for exclusive reconstruction is essential to extract polarization observables was highlighted in Sections 7.2 and 7.4. It further decrease the expected statistics, e.g., from 2M to 200k events in the $K\Xi$ case. These statistics, however, would allow a precise measurement of the double-differential polarization observables with statistical uncertainties on the order of 10 %. Secondly, kaon flux has a maximum around $W = 3$ GeV, which decreases rapidly towards high/low W 's. Thus, the 100 days of beam time on the LH_2 are essential to maximize the discovery potential of the K_L Facility and uncover the densely populated hyperon states at low- W .

There are no data on "neutron" targets and, for this reason, it is hard to make a realistic estimate of the statistics for $K_L n$ reactions. If we assume similar statistics as on a proton target, the full program will be completed after running 100 days with LH_2 and 100 days with LD_2 targets.

Appendices

A1 The Interest of the RHIC/LHC Community in Excited Hyperon Measurements

The relativistic heavy-ion community at RHIC and the LHC has recently embarked on specific analyses to address the issue of strangeness hadronization. LQCD calculations in the QCD crossover transition region between a deconfined phase of quark and gluons and a hadronic resonance gas have revealed a potentially interesting sub-structure related to the hadronization process. Studies of flavor-dependent susceptibilities, which can be equated to experimental measurements of conserved quantum-number fluctuations, seem to indicate a slight flavor hierarchy in the three-quark sector (u,d,s) in thermalized systems. Specifically, the ratios of higher-order susceptibilities in the strange sector show a higher transition temperature than in the light sector [186]. Both pseudo-critical temperatures are still within the error bars of the quoted transition temperature based on all LQCD order parameters [187, 188], which is 154 ± 9 MeV, but the difference of the specific susceptibilities is around 18 MeV and well outside their individual uncertainties.

This difference seems to be confirmed by statistical thermal-model calculations that try to describe the yields of emitted hadrons from a QGP based on a common chemical freeze-out temperature. Although the yields measured by ALICE at the LHC in 2.76 TeV PbPb collisions can be described by a common temperature of 156 ± 2 MeV, with a reasonable χ^2 , the fit improves markedly if one allows the light quark baryons to have a lower temperature than the strange quark baryons [189]. A similar result has been found when the thermal fluctuations of particle yields as measured by the STAR Collaboration [190, 191], which can be related to the light quark dominated susceptibilities of the electric charge and the baryon number on the lattice, have been compared to statistical model calculations [192].

If one assumes that strange and light quarks indeed prefer different freeze-out temperatures, then the question arises how this could impact the hadronization mechanism and abundance of specific hadronic species. In other words, is the production of strange particles, in particular excited resonant states, enhanced in a particular temperature range in the crossover region? Strange ground-state particle production shows evidence of enhancement, but the most likely scenario is that the increased strange quark abundance will populate excited states; therefore, the emphasis of any future experimental program trying to understand hadron production is shifting towards strange baryonic resonance production. Furthermore, recent LHC measurements in small systems, down to elementary proton-proton collisions, have revealed that even in these small systems there is evidence for deconfinement, if the achieved energy density, documented by the measured charged particle multiplicity is large enough [193]. Therefore, future measurements of elementary collisions in the K-Long Facility experiment at JLab might well provide the necessary link to future analysis of strange resonance enhancements in heavy-ion collisions at RHIC and the LHC and a deeper understanding of the hadronization process.

This statement is also supported by comparisons between the aforementioned LQCD calculations

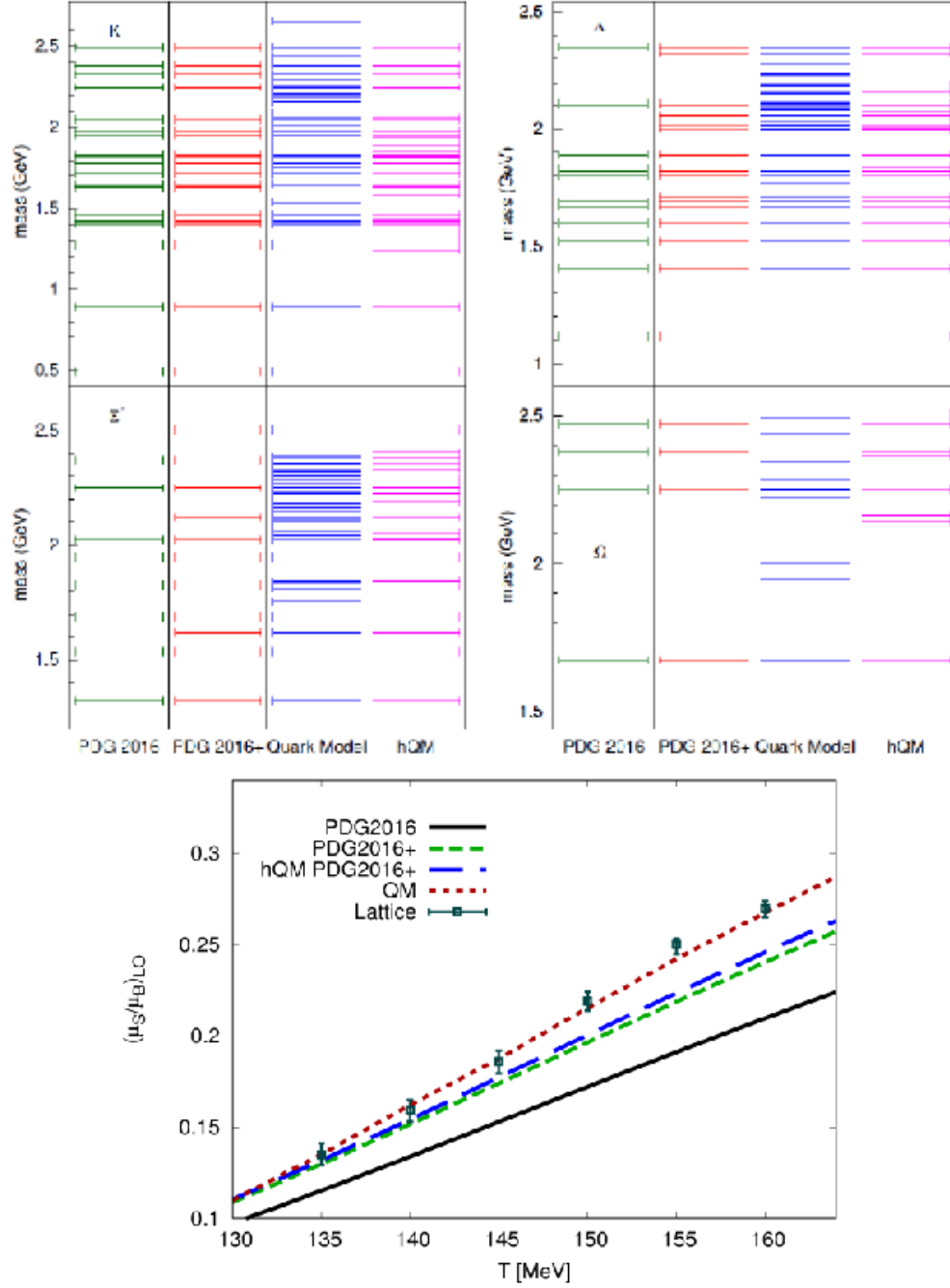


Figure 33: Upper panel: Comparison of predicted and measured excited strange hadronic states in PDG2018, PDG2018+ (including one star states), QM, and hQM. Lower panel: Lattice QCD calculation of the temperature dependence of the leading order susceptibility ratio (μ_s/μ_B) compared to results from HRG model calculations with varying number of hadronic states.

and model predictions based on a non-interacting hadronic resonance gas. The Hadron Resonance Gas (HRG) model [194–197] yields a good description of most thermodynamic quantities in the hadronic phase up to the pseudo-critical temperature. The idea that strongly interacting matter in the ground state can be described in terms of a non-interacting gas of hadrons and res-

onances, which effectively mimics the interactions of hadrons by simply increasing the number of possible resonant states exponentially as a function of temperature, was proposed early on by Hagedorn [198]. The only input to the model is the hadronic spectrum: usually it includes all well-known hadrons in the *Review of Particle Physics* (RPP), namely the ones rated with at least two stars. Recently, it has been noticed that some more differential observables present a discrepancy between lattice and HRG model results. The inclusion of not-yet-detected states, such as the ones predicted by the original Quark Model (QM) [199, 200] has been proposed to improve the agreement [201, 202]. A systematic study based on a breakdown of contributions to the thermodynamic pressure given by particles grouped according to their quantum numbers (in particular baryon number and strangeness) enables us to infer in which hadron sector more states are needed compared to the well-known ones from the RPP [203]. In case of a flavor hierarchy in the transition region, one would expect the number of strange resonances to increase, due to a higher freeze-out temperature, compared to the number of light-quark resonances. Figure 33 shows the effect of different strange hadron input spectra to the HRG model in comparison to LQCD. Figure 33 (Upper plot) shows the number of states in PDG2018 [3], PDG2018+ (including one star states), the standard QM, and a Quark Model with enhanced quark interactions in the hadron (hyper-central model hQM [204]). Fig. 33 (Lower plot) shows a comparison of the HRG results to a leading-order LQCD calculation of μ_s/μ_B ; i.e., the ratio to strange to baryon number susceptibility [203].

An interesting conclusion that arises from these studies is that the improvement in the listing of strange resonances between PDG2008 [205] and PDG2018 [3] definitely brought the HRG calculations closer to the LQCD data. By looking at details in the remaining discrepancy, which is in part remedied by including one-star rated resonances in PDG2018, it seems that the effect is more carried by singly strange resonances rather than multi-strange resonances, also in light of comparisons to quark models that include di-quark structures [206] or enhanced quark interactions in the baryon (hypercentral models [204]). This is good news for the experiments since the Λ and Σ resonances below 2 GeV are well within reach of the KLF experiment and, to a lesser significance, the RHIC/LHC experiments. In this context it is also important to point out that the use of both hydrogen and deuterium targets in KLF is crucial since it will enable the measurement of charged and neutral hyperons. A complete spectrum of singly strange hyperon states is necessary to make a solid comparison to first-principle calculations.

To summarize: Any comparisons between experimentally verified strange quark-model states from YSTAR and LQCD will shed light on a multitude of interesting questions relating to hadronization in the non-perturbative regime, exotic particle production, the interaction between quarks in baryons and a possible flavor hierarchy in the creation of confined matter.

A2 Previous Measurements for Hyperons

While a formally complete experiment requires the measurement, at each energy, W , and angle, θ , of at least three independent observables, the current database for $K_L p \rightarrow \pi Y$ and KY is populated mainly by unpolarized cross sections. Figure 34 illustrates this quite clearly.

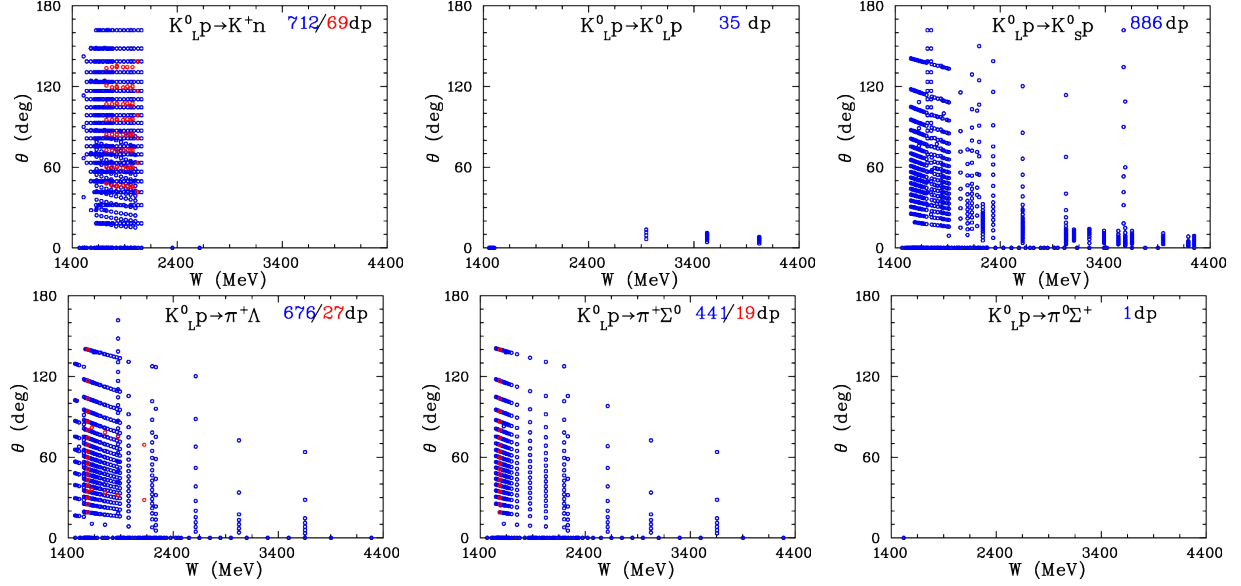


Figure 34: Experimental data available for $K_L p \rightarrow K^+ n$, $K_L p \rightarrow K_L p$, $K_L p \rightarrow K_S p$, $K_L p \rightarrow \pi^+ \Lambda$, $K_L p \rightarrow \pi^+ \Sigma^0$, and $K_L p \rightarrow \pi^0 \Sigma^+$ as a function of CM energy W [207]. The number of data points (dp) is given in the upper righthand side of each subplot [blue (red) shows the amount of unpolarized (polarized) observables]. Total cross sections are plotted at zero degrees.

The initial studies of the KLF program at GlueX will likely focus on two-body and quasi-two-body processes: elastic $K_L p \rightarrow K_S p$ and charge-exchange $K_L p \rightarrow K^+ n$ reactions, then two-body reactions producing $S = -1$ ($S = -2$) hyperons as $K_L p \rightarrow \pi^+ \Lambda$, $K_L p \rightarrow \pi^+ \Sigma^0$, and $K_L p \rightarrow \pi^0 \Sigma^+$ ($K_L p \rightarrow K^+ \Xi^0$). Most of the previous measurements induced by a K_L beam, were collected for $W = 1454$ MeV and with some data up to $W = 5054$ MeV. Experiments were performed between 1961 and 1982 with mostly hydrogen bubble chambers at ANL, BNL, CERN, DESY, KEK, LRL, NIMROD, NINA, PPA, and SLAC. Note that some of data were taken at EM facilities at NINA [137] (a short overview about NINA experiments is given by Albrow recently [208]) and SLAC [136]. The goal of the Manchester University group that worked at the Daresbury 5-GeV electron synchrotron NINA was CP-violation, which was a hot topic back to the mid 1960s. The main physics topics that the SLAC group addressed were studies of the systematics for particle/anti-particle processes through the intrinsic properties of the K-longs.

The first paper that discussed the possibility of creating a practical neutral kaon beam at an electron synchrotron through photoproduction was an optimistic prediction for SLAC by Drell and Jacob in 1965 [209]. With significant developments in technology, high-quality EM facilities, such as JLab [15], are now able to realize a complete hyperon spectroscopy program.

The overall systematics of previous $K_L p$ experiments varies between 15 % and 35 %, and the

energy binning is much broader than hyperon widths. The previous number of K_L -induced measurements (2426 $d\sigma/d\Omega$, 348 σ^{tot} , and 115 P observables) [207] was very limited. Additionally, we are not aware of any measurements on a “neutron” target.

Our knowledge about the non-strange sector is more advanced vs. the strange one [3]. For the non-strange case, for instance, phenomenology has access to 51k data of $\pi N \rightarrow \pi N$ and 39k data of $\gamma N \rightarrow \pi N$ below $W = 2.5$ GeV [76].

A3 Determination of Pole Positions

In spite of their model dependence, partial-wave BW parameters have for quite some time been the preferred connection between experiment and QCD in hadronic spectroscopy. More recently, however, pole parameters (e.g., pole positions and residues) have justifiably become the preferred connection, and this fact has also been recognized by the Particle Data Group in recent editions of the *Review of Particle Physics* [3]. Therefore, the extraction of pole parameters from experimental data becomes a procedure of utmost importance.

Extraction of pole parameters is usually performed in two ways: (a) in an energy-dependent way (ED) or (b) in an energy-independent procedure through SES PWAs. In an ED procedure, one measures as many observables as possible to be close to the complete set and then fits the observables with parameters of a well-founded theoretical model that describes the reaction in question. Continuity in energy is enforced by the features of the theoretical model. In a SE procedure, one again measures as many observables as possible but attempts to extract partial waves by fitting energy-binned data independently, therefore, reducing the theoretical input. A discrete set of partial waves is obtained, and the issues of achieving continuity in energy have recently been extensively discussed either by introducing the constraints in analyticity [210] or through angle- and energy-dependent phase ambiguity [211,212].

In energy-dependent models, pole parameters have been extracted in various ways. The most natural way is the analytic continuation of theoretical model solutions into the complex-energy plane. Simpler single-channel pole extraction methods have been developed such as the speed plot [213], time delay [214], the N/D method [215], regularization procedures [216], and Pade approximants [117], but their success has been limited. In single-energy analyses, the situation is even worse: until recently no adequate method has been available for the extraction of pole parameters. All single-channel methods involve first- or higher-order derivatives, so partial-wave data had to be either interpolated or fitted with an unknown function, and that introduced additional and, very often, uncontrolled model dependencies.

That situation has been recently overcome when a new Laurent+Pietarinen (L+P) method applicable to both, ED and SES models, has been introduced [217–221]. The driving concept behind the single-channel (and later multichannel) L+P approach was to replace solving an elaborate theoretical model and analytically continuing its solution into the full complex-energy plane, with an approximation actualized by local power-series representation of partial-wave amplitudes having well-defined analytic properties on the real energy axis, and fitting it to the given input. In such a way, the global complexity of a model is replaced by a much simpler, and almost model-independent expansion, limited to the regions near the real energy axis. And this is sufficient to obtain poles and their residues. This procedure gives the simplest function with known analytic structure that fits the data. Formally, the introduced L+P method is based on the Mittag-Leffler expansion³ of partial-wave amplitudes near the real-energy axis, where we represented the regular background term by a conformal-mapping-generated, fastly converging power series called a

³Mittag-Leffler expansion [222] is the generalization of a Laurent expansion to a more-than-one pole situation. For simplicity, we call it Laurent expansion.

Pietarinen expansion ⁴. In practice, the regular background part is usually fitted with three Pietarinen expansion series. Each of them approximates the most general function which describes the background, and has a branch point at x_{bp} , while all free parameters are then fitted to the chosen channel input. The first Pietarinen expansion with branch-point x_P which is restricted to an unphysical energy range represents all left-hand cut contributions. The next two Pietarinen expansions describe background in the physical range, and the used branch points x_Q and x_R are defined by the analytic properties of the analyzed partial wave. A second branch point is usually fixed to the elastic channel branch point describing threshold effects, and the third one is either fixed to the dominant channel threshold value, or let free.

Thus, solely on the basis of general physical assumptions about analytic properties of the fitted process like number of poles and number and location of conformal mapping branch points, the pole parameters in the complex energy plane are obtained. In such a way, the simplest analytic function with a set of poles and branch points which is fitting the input is actually constructed. This method is equally applicable to both theoretical and experimental input ⁵.

The transition amplitude of the multichannel L+P model is parametrized as

$$T^a(W) = \sum_{j=1}^{N_{pole}} \frac{g_j^a}{W_j - W} + \sum_{i=1}^3 \sum_{k_i=0}^{K_i^a} c_{k_i}^a \left(\frac{\alpha_i^a - \sqrt{x_i^a - W}}{\alpha_i^a + \sqrt{x_i^a - W}} \right)^{k_i}, \quad (8)$$

where a is a channel index, W_j are pole positions in the complex W (energy) plane, g_j^a coupling constants. The x_i^a define the branch points, $c_{k_i}^a$, and α_i^a are real coefficients. K_i^a , $i = 1, 2, 3$ are Pietarinen coefficients in channel a . The first part represents the poles and the second term three branch points. The first branch point is chosen at a negative energy (determined by the fit), the second is fixed at the dominant production threshold, and the third branch point is adjusted to the analytic properties of fitted partial wave.

To enable the fitting, a reduced discrepancy function D_{dp} is defined as

$$D_{dp} = \sum_a^{all} D_{dp}^a;$$

$$D_{dp}^a = \frac{1}{2 N_W^a - N_{par}^a} \times \sum_{i=1}^{N_W^a} \left\{ \left[\frac{\text{Re } T^a(W^{(i)}) - \text{Re } T^{a,exp}(W^{(i)})}{Err_{i,a}^{Re}} \right]^2 + \left[\frac{\text{Im } T^a(W^{(i)}) - \text{Im } T^{a,exp}(W^{(i)})}{Err_{i,a}^{Im}} \right]^2 \right\} + \mathcal{P}^a,$$

⁴This type of conformal mapping expansion was introduced by Ciulli and Fisher [223, 224]. It was described in details and also used in pion-nucleon scattering by Pietarinen [225, 226]. The procedure was named Pietarinen expansion by Höhler in Ref. [60].

⁵Observe that fitting partial wave data originating from experiment as energy independent analysis is even more favorable.

where

$$\mathcal{P}^a = \lambda_{k_1}^a \sum_{k_1=1}^{K^a} (c_{k_1}^a)^2 k_1^3 + \lambda_{k_2}^a \sum_{k_2=1}^{L^a} (c_{k_2}^a)^2 k_2^3 + \lambda_{k_3}^a \sum_{m=1}^{M^a} (c_{k_3}^a)^2 k_3^3$$

is the Pietarinen penalty function, which ensures fast and optimal convergence. N_W^a is the number of energies in channel a , N_{par}^a the number of fit parameters in channel a , λ_c^a , λ_d^a , λ_e^a are Pietarinen weighting factors, $Err_{i,a}^{Re, Im}$... errors of the real and imaginary part, and $c_{k_1}^a$, $c_{k_2}^a$, $c_{k_3}^a$ real coupling constants.

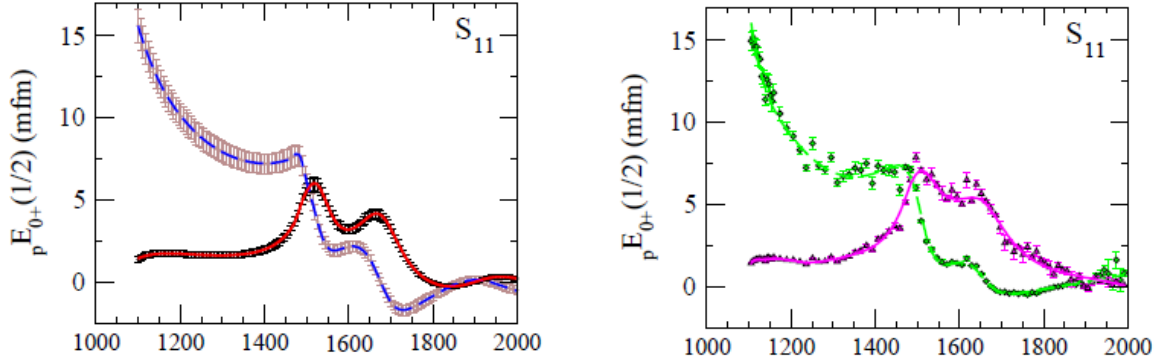


Figure 35: L+P fit to CM12 GW/SAID pion photoproduction $_pE_{0+}$ ED and SESs [227].

In order to obtain reliable answers in the L+P model we have to build knowledge about the analytic structure of the fitted partial wave into the fitting procedure. Because we are looking for poles, we only have to define which branch points to include. Their analytic form will be determined by the number of Pietarinen coefficients. As we have only three branch points at our disposal we expect that the first branch-point will describe all subthreshold and left-hand cut processes, the second one is usually fixed to the dominant channel opening, and the third one is to represent background contributions of all channel openings in the physical range. So, in addition to choosing the number of relevant poles, our anticipation of the analytic structure of the observed partial wave is of great importance for the stability of the fit.

The L+P model has been successfully applied to both theoretical models and discrete partial-wave data. As an example, in Fig. 35, we give the achieved quality of the fit for the CM12 GW/SAID pion photoproduction amplitudes [227].

To summarize: Methods of the described L+P model will be used to extract pole parameters for both ED solutions, obtained by the method described in Section 4, and SESs developed independently.

Element	Outer \varnothing /Inner \varnothing (m)	Thickness (m)	Volume (m ³)	Density (kg/m ³)	Mass (kg)
Borated polyethylen (front)	1.20/0.16	0.10	0.111	1000	111.1
Borated polyethylen (side)	1.20/1.00	1.30	0.449	1000	449.2
Borated polyethylen (back)	1.20/0.08	0.10	0.113	1000	112.6
Lead (front)	1.00/0.16	0.30	0.230	11350	2605.8
Lead (side)	1.00/0.76	0.70	0.232	11350	2635.8
Lead (back)	1.00/0.08	0.30	0.234	11350	2657.2
Tungsten (front)	0.76/0.16	0.40	0.173	19300	3346.9
Tungsten (center)	0.76/0.00	0.10	0.045	19300	875.5
Tungsten (back)	0.76/0.08	0.20	0.090	19300	1731.7
Beryllium	0.06/0.00	0.40	0.001	1848	2.1

Table 7: Elements of the Be-target assembly.

A4 Neutron and Gamma Background

1. Elements of the Be-target Assembly

Schematic view of the Be-target assembly (K_L production target) is given in Fig. 14. The elements of the Be-target assembly are presented in Table 7. The weight of the construction is 14.5 ton. Changeover from the photon to K_L beamline and from the K_L beamline to photon needs to be further evaluated and in the most conservative scenario may take approximately 6 months or less. This maximal break period may fit the current CEBAF Accelerator schedule. It has to be mentioned that the collimator cave has enough space (with the 4.52 m width) for the Be-target assembly to remain far enough from the beamline.

2. Neutron and Gamma Background

The schematic view of the collimator cave with the Be-target assembly is given in Fig. 13.

Several tallies were placed along the beam and at the experimental hall for neutron and γ fluence estimation. Tally descriptions are:

- **#1:** spot for flux ($\varnothing 0.07$ m) on the beam in the experimental hall right behind of the concrete wall;
- **#2:** spot for flux ($\varnothing 0.07$ m) outside the beam in the experimental hall right behind of the concrete wall;
- **#3:** spot for flux ($\varnothing 0.07$ m) on the beam in the experimental hall right on the face of the cryogenic target;
- **#4:** spot for flux ($\varnothing 0.07$ m) outside the beam in the experimental hall right on the face of the cryogenic target;
- **#5:** area for dose rate (6×6 m²) on ceiling of the experimental hall centered at the GlueX detector - key area for the RadCon;
- **#6:** ring for dose rate (outer $\varnothing 0.08$ m and inner $\varnothing 0.07$ m) on the face of the cryogenic target - to evaluate a radiation damage for the SiPMs;
- **#7-9:** area for dose rate (1×1 m²) hallway in the experimental hall following the GlueX detector;
- **#10-19:** rings for dose rate (outer $\varnothing 0.25, 0.45, 0.65, 0.85, 1.05, 1.25, 1.45, 1.65, 1.85, 2.05$ m and inner $\varnothing 0.20, 0.40, 0.60, 0.80, 1.00, 1.20, 1.40, 1.60, 1.80, 2.00$ m, respectively) on the face of the cryogenic target - to evaluate a radiation damage for the front of the BCAL;
- **#20:** spot for flux ($\varnothing 0.07$ m) on the beam right behind beryllium;
- **#21:** spot for flux ($\varnothing 0.07$ m) on the beam right behind tungsten.

(a) Neutron Background

Calculations were performed for different shielding configurations in the collimator cave to minimize the neutron and γ dose rate.

The K_L s, produced by the Be-target and survived after the beam tungsten or lead plug, are presented in Fig. 36. This figure shows that there is a small effect in the material difference in the beam plug. There are 10 % of K_L s, produced by the Be-target, survived after the beam tungsten plug. The neutron yield integral from the berilium is $2.4 \times 10^{10} \text{ n}/(\text{s} \cdot \text{cm}^2)$ and then from tungsten is $4.2 \times 10^9 \text{ n}/(\text{s} \cdot \text{cm}^2)$ (Figs. 37 and 38). So, the tungsten plug reduced the neutron flux by the same amount as the neutral kaon flux.

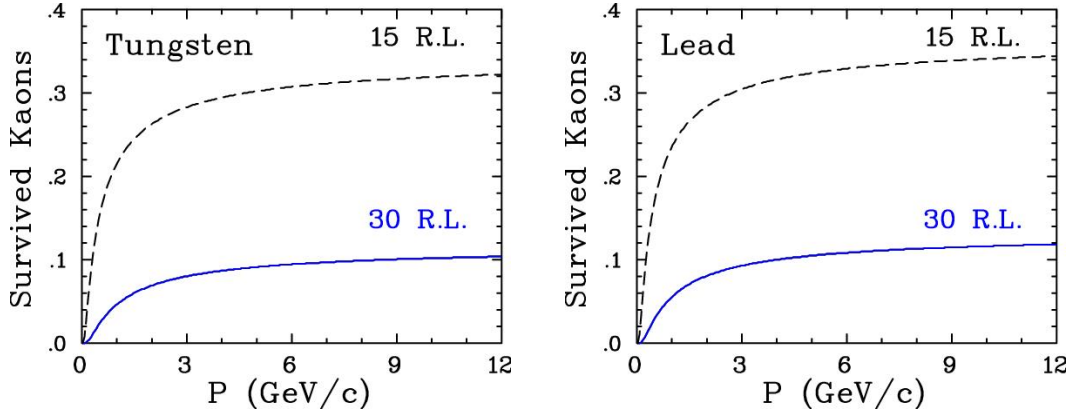


Figure 36: Fraction of survived kaons after the tungsten (left) or lead (right) plugs are installed with 15 or 30 R.L.

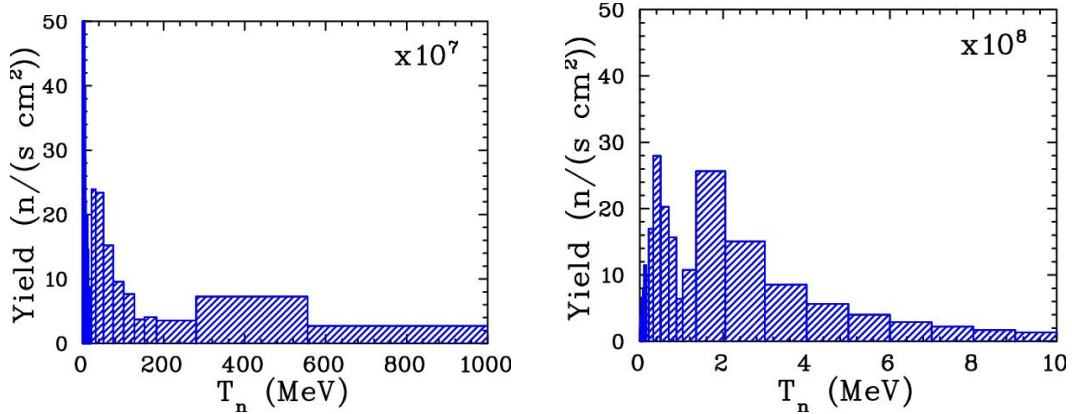


Figure 37: Number of neutrons that will not pass through the tungsten plug. Calculations were performed using the MCNP Transport code [152].

Calculations were performed for different shielding configurations in the collimator cave to minimize the neutron and γ dose rate. The vertical (horizontal) cross section of the neutron flux is given in Fig. 39 (Fig. 40).

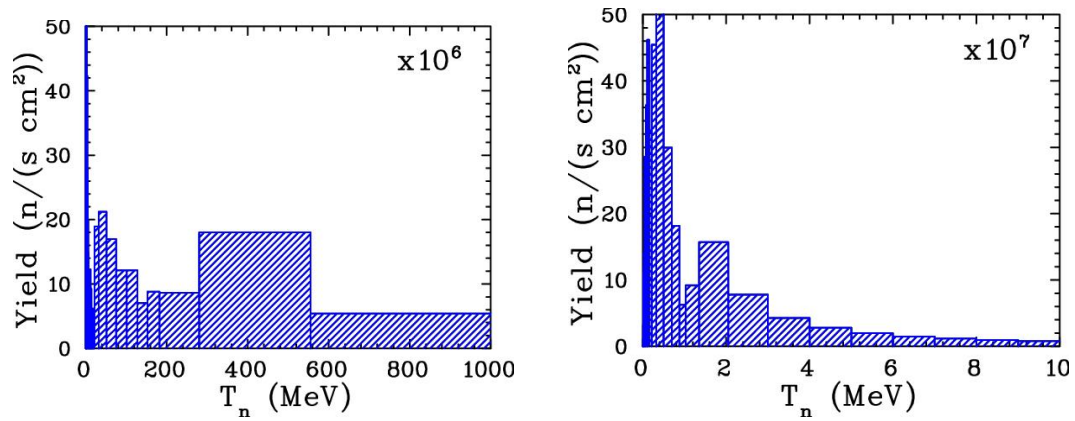


Figure 38: Number of neutrons that will pass through the tungsten plug. Calculations were performed using the MCNP Transport code [152].

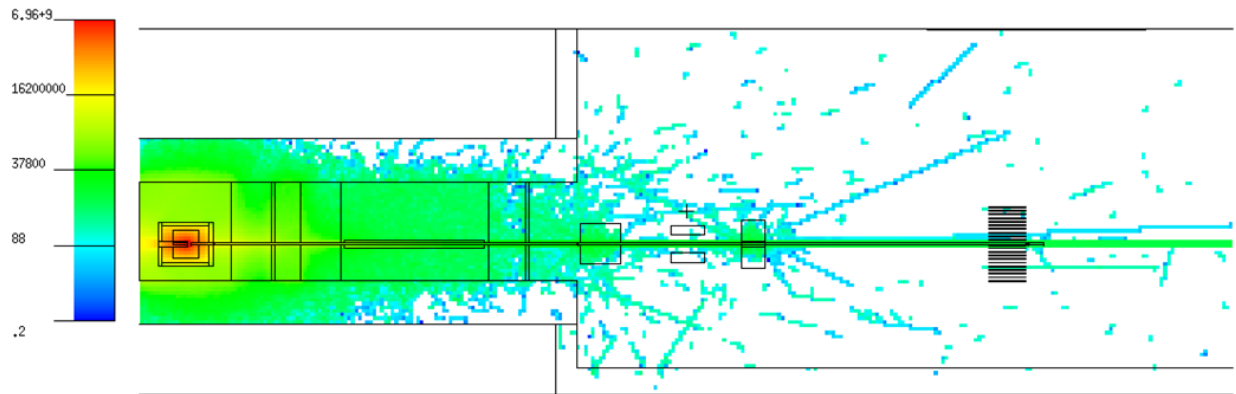


Figure 39: Vertical cross section of the neutron flux calculated for the model. Beam goes from left to right.

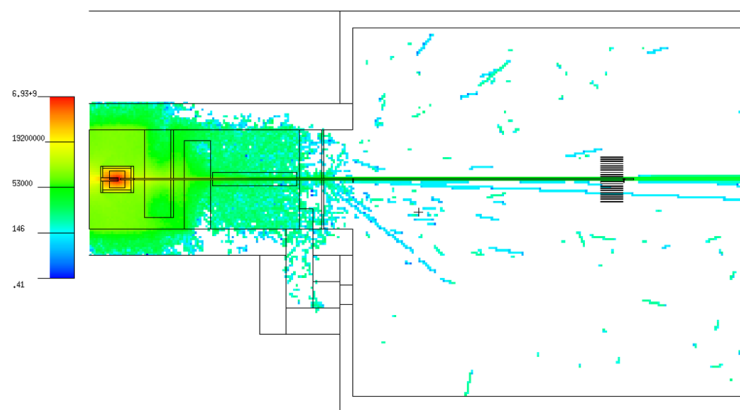


Figure 40: Horizontal cross section of the neutron flux calculated for the model. Beam goes from left to right.

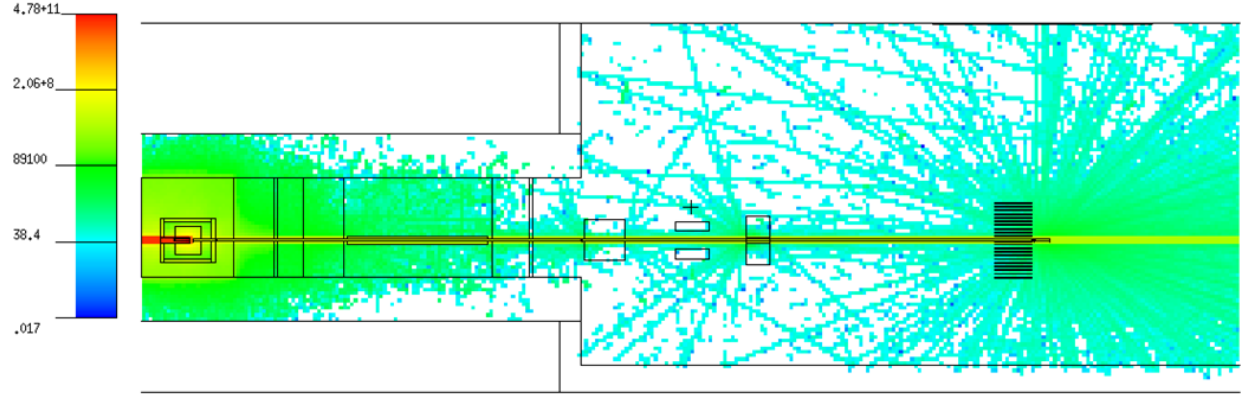


Figure 41: Vertical cross section of the γ flux calculated for the model.

Tally	Neutron flux ($\text{n}/(\text{s}\cdot\text{cm}^2)$)	Photon flux ($\gamma/(\text{s}\cdot\text{cm}^2)$)
#1	$(8.0\pm0.5)\times10^4$ (6.7 %)	$(31.1\pm0.1)\times10^6$ (0.3 %)
#2	$(2.2\pm1.7)\times10^3$ (75 %)	$(3.3\pm1.0)\times10^3$ (31 %)
#3	$(1.7\pm0.2)\times10^4$ (11 %)	$(27.2\pm0.1)\times10^6$ (0.3 %)
#4	$> 1.7 \times 10^2$	$(9.9\pm1.6)\times10^3$ (16 %)
#20	$(236.0\pm0.1)\times10^8$ (0.1 %)	$(223.0\pm0.5)\times10^6$ (0.02 %)
#21	$(41.7\pm0.1)\times10^8$ (0.1 %)	$(10.7\pm0.1)\times10^6$ (0.2 %)

Table 8: Neutron (2nd column) and γ (3rd column) background flux calculated for different tallies (1st column). Percentage in brackets shows statistical uncertainties of MC simulations.

(b) Gamma Background

The vertical cross section of the γ flux is given in Fig. 41.

3. Neutron Dose Rate for the SiPM

The neutron dose rate for the silicon photomultipliers (SiPM) of the start counter [156–158] and BCAL [158, 159] is given in Fig. 19(left). There is an issue for SiPM and low level of BCAL. Previous studies stand that the dose rate of 30 mreh/h increases a dark current at SiPM by a factor of 5 after 75 days of running period [160].

Tally	Dose rate (mrem/h)	Dose rate (mrem/h)
#5	0.11 ± 0.04 (36 %)	$(2.0 \pm 0.1) \times 10^{-2}$ (3.8 %)
#6	632 ± 145 (23 %)	$(3.0 \pm 0.1) \times 10^3$ (2.9 %)
#7	0.02 ± 0.02 (100 %)	$(7.1 \pm 4.2) \times 10^{-3}$ (59 %)
#8	0.01 ± 0.01 (100 %)	$(3.0 \pm 1.8) \times 10^{-3}$ (58 %)
#9	> 0.1	$(2.2 \pm 0.5) \times 10^{-2}$ (25 %)
#10	1.8 ± 1.8 (100 %)	(0.52 ± 0.04) (7.8 %)
#11	> 0.1	(0.57 ± 0.10) (18 %)
#12	> 0.1	(0.45 ± 0.05) (10 %)
#13	0.01 ± 0.01 (100 %)	(0.42 ± 0.05) (13 %)
#14	0.3 ± 0.3 (86 %)	(0.46 ± 0.05) (11 %)
#15	0.4 ± 0.2 (61 %)	(0.36 ± 0.04) (11 %)
#16	0.1 ± 0.1 (91 %)	(0.28 ± 0.02) (7.4 %)
#17	1.2 ± 0.8 (66 %)	(0.24 ± 0.01) (5.5 %)
#18	0.3 ± 0.2 (77 %)	(0.19 ± 0.01) (3.4 %)
#19	0.3 ± 0.2 (57 %)	(0.18 ± 0.01) (4.0 %)

Table 9: Neutron (2nd column) and γ (3rd column) dose rate background calculated for different tallies (1st column). Percentage in brackets shows statistical uncertainties of MC simulations.

A5 Hyperon Spectroscopy: Details of Monte Carlo Study

Detailed and extensive simulations on various channels were performed to obtain an insight on the expected results and the beam time requirements for precision measurements as discussed in Sec. 7. This appendix aims at providing more details on the simulations performed.

A5.1 K_L Beam

The K_L beam is generated by sampling the momentum distribution of K_L particles produced by interactions of a photon beam with a beryllium target 24 m upstream of the LH_2/LD_2 cryogenic target. The K_L beam profile was simulated to be uniform within a $\varnothing 0.06$ m at the LH_2/LD_2 cryogenic target. The expected K_L beam nonuniformity is below 2 % with a beam divergence $< 0.15^\circ$ (see Table 1). Due to the very strong t -dependence in the ϕ photoproduction cross section [228] and the P -wave origin of the $\phi \rightarrow K_L K_S$ decay, the majority of kaons will be produced at very small angles. In the simulation studies discussed in this section, 1×10^4 K_L /s are impinged on a 0.40 m long LH_2 target for a beamtime of 100 PAC days.

A5.2 The GlueX Detector

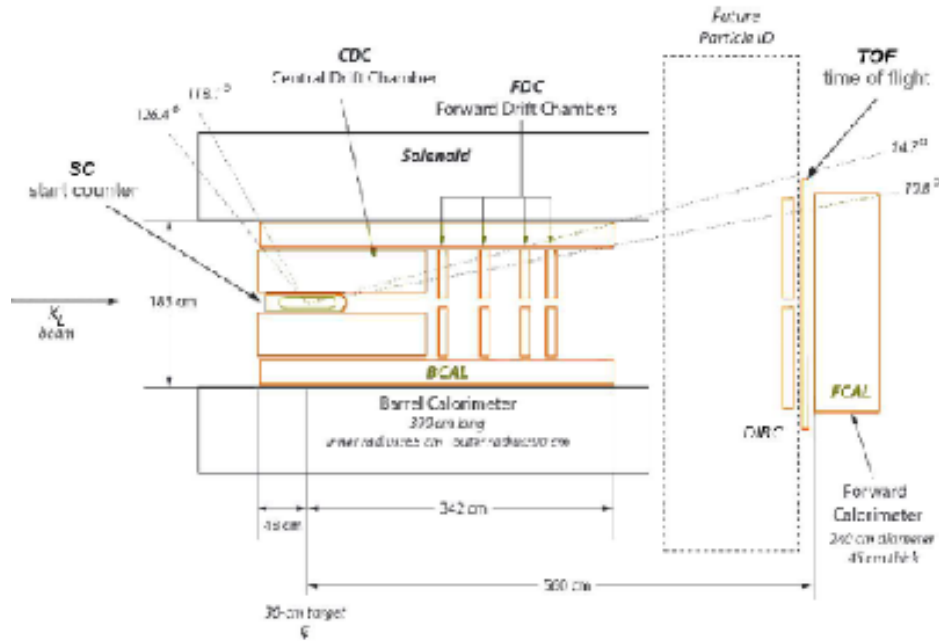


Figure 42: Schematic view of the GlueX detector.

The GlueX detector is a large acceptance detector based on a solenoid design with good coverage for both neutral and charged particles. The detector consists of a solenoid magnet enclosing devices for tracking charged particles and detecting neutral particles, and a forward region consisting of

two layers of scintillators (TOF) and a lead-glass EM calorimeter (FCAL). A schematic view of the GlueX detector is shown in Fig. 42. The magnetic field at the center of the bore of the magnet for standard running conditions is about 2 T. The trajectories of charged particles produced by interactions of the beam with the 0.40-m LH_2/LD_2 cryogenic target at the center of the bore of the magnet are measured using the Central Drift Chamber (CDC) for angles greater than $\approx 20^\circ$ with respect to the beamline. Forward-going tracks are reconstructed using the Forward Drift Chambers (FDC). The timing of the interaction of the kaon beam with the LH_2 cryogenic target is determined using signals from the ST, an array of 30 mm thin (3 mm thick) scintillators enclosing the target region. Photons are registered in the central region by the BCAL. Detector performance and reconstructions techniques were evaluated during the main GlueX program. Details can be found elsewhere [164].

The following sections provide details on particle identification as well as details on the various channels studied. All simulations assumed standard beam/target conditions listed in Tables 1 and 2. A Geant3 based simulation of the GlueX detector was used to process all generated events. An extensive list of channels was generated and studied in great detail. Here we focus on simulations for the following channels:

1. $K_L p \rightarrow K_s p$
2. $K_L p \rightarrow \pi^+ \Lambda$
3. $K_L p \rightarrow K^+ \Xi^0$
4. $K_L n \rightarrow K^+ \Xi^-$
5. $K_L n \rightarrow K^+ \Xi^{*-}$
6. $K_L p \rightarrow K^+ n$

A5.3 Particle Identification

For each channel, one primary particle (the proton for the $K_s p$ channel, the π^+ for the $\pi^+ \Lambda$ channel and the K^+ for the $K^+ \Xi$ and $K^+ n$ channels) provides a rough determination for the position of the primary vertex along the beamline that is used in conjunction with the ST to determine the flight time and path of the K_L from the beryllium target to the hydrogen target, and thus determine its momentum. Protons, pions, and kaons are distinguished using a combination of dE/dx in the chambers and time-of-flight to the outer detectors (BCAL and TOF). The energy loss and timing distributions for the $K_s p$ channel are shown as an example in Fig. 43; the distributions are similar for the $\pi^+ \Lambda$ channel, where a proton band arises from the $\Lambda \rightarrow \pi^- p$ decay. Also shown is the dE/dx distribution for the $K^+ \Xi^0$ channel, where a prominent kaon band can be seen, along with pion and proton bands arising from Λ decays.

Since the GlueX detector has full acceptance in ϕ for charged particles and large acceptance in θ (roughly $1 - 140^\circ$), a full reconstruction of events is feasible for the majority of the channels. That will allow to apply four or more overconstrain kinematical fit and improve the resolution

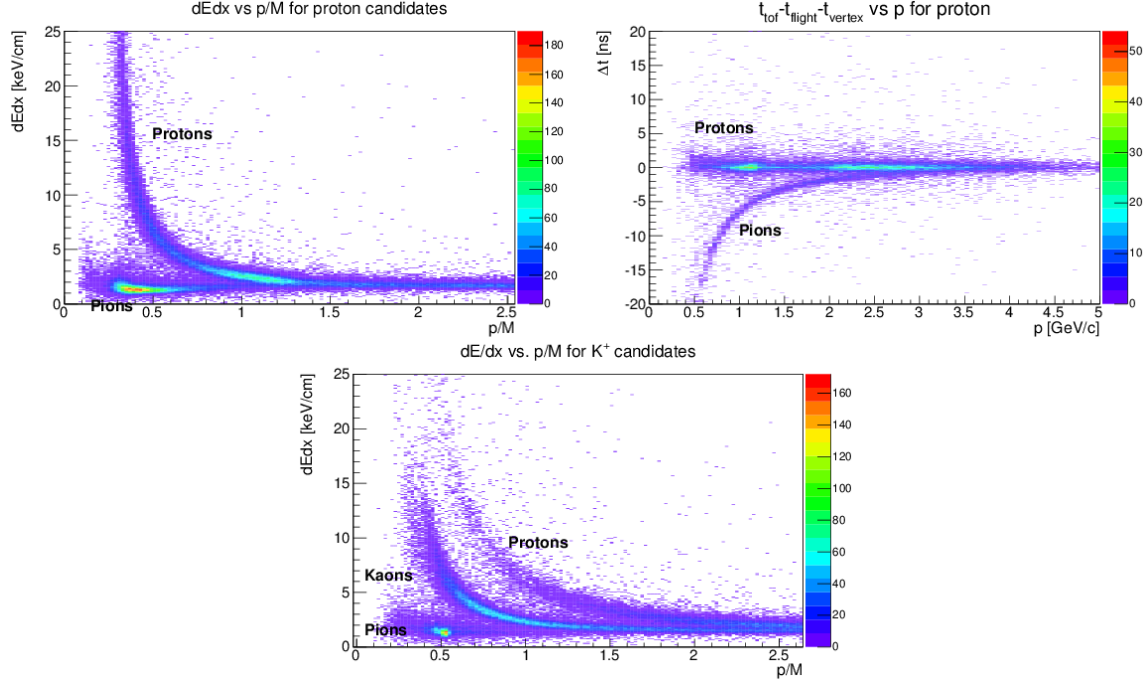


Figure 43: Particle identification. Top left panel: dE/dx for the $K_S p$ channel. Top right panel: Time difference at the primary “vertex” for the proton hypothesis for the $K_S p$ channel using the TOF. Bottom panel: dE/dx for the $K^+ \Xi$ channel. The proton and pion bands arise from the decay of the Λ .

considerably. A typical comparison between W reconstruction using the K_L -momentum for 250 ps ST resolution (red dots) and the other using kinematically fitted final-state particles for the $K_S p$ channel (blue dots) is shown in Fig. 44. Detection of all final state particles in any channel allows an improvement by about an order of magnitude in the W resolution at high W .

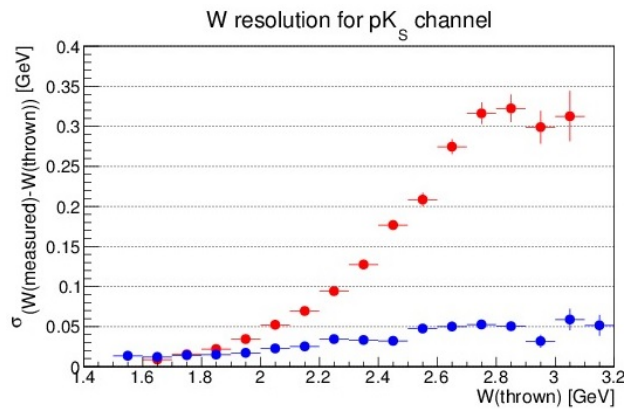


Figure 44: W resolution for the $K_S p$ channel, (blue dots) using kinematic fitting after reconstruction of all final state particles; (red dots) using K_L time-of-flight.

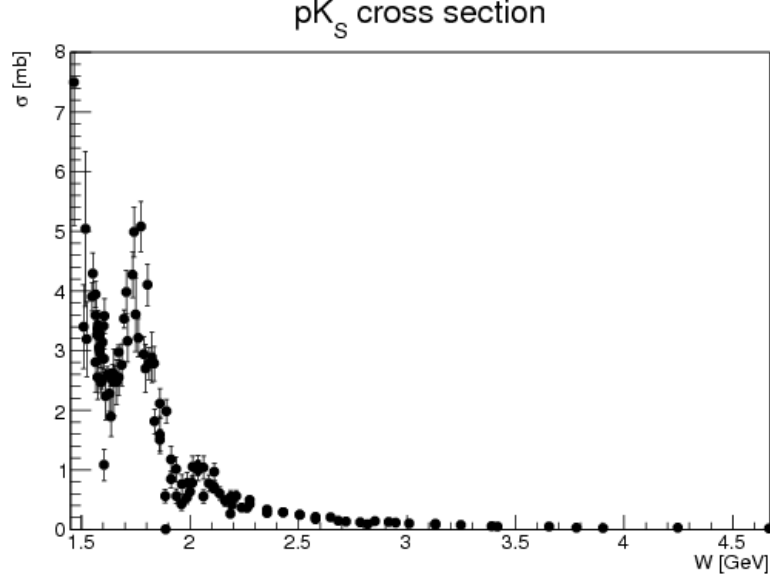


Figure 45: Total cross section for $K_L p \rightarrow K_S p$ as a function of W . The measured data are from [165] and references therein.

A5.4 Details of MC study for $K_L p \rightarrow K_S p$

The total production cross section, shown in Fig. 45, is reasonably large; however, for the differential cross section there is a fair amount of tension in the existing data sets between different measurements, and the angular coverage in some bins is sparse. Figure 46 shows the existing differential cross section data for several bins in W . The cross section as a function of $\text{CM } \cos \theta$ was parametrized using a set of Legendre polynomials (blue curves in Fig. 46); the weights of each polynomial in the set depended on W . This parametrization was used to generate $K_L p \rightarrow K_S p$ events that were passed through a full Geant3-based Monte Carlo (MC) of the GlueX detector. The final-state particles were constructed using the standard GlueX reconstruction code. We reconstructed the K_S taking advantage of the BR of 69.2 % for $K_S \rightarrow \pi^+ \pi^-$ [3]; the invariant mass of the $\pi^+ \pi^-$ pair and W as computed from the four-momenta of the proton and the two pions is shown in Fig. 47.

After combining the four-momenta of the final-state particles with the four-momenta of the beam and the target, the missing-mass squared for the full reaction should be zero, which is also shown in Fig. 47. Finally, one requires conservation of energy and momentum in the reaction by applying a kinematic fit to the data. After applying a 0.1 cut on the confidence level of the fit, an estimate for the reconstruction efficiency has been calculated and is shown as a function of W in Fig. 48. Here the efficiency includes the BR for $K_S \rightarrow \pi^+ \pi^-$. The average reconstruction efficiency is about 7 %.

The statistical uncertainties in measured cross section for 100 days of running as a function of $\text{CM } \cos \theta$ for several values of W are shown in Fig. 49. We estimate that for $W < 3$ GeV, we will detect on the order of 2.7M $K_S p$ events in the $\pi^+ \pi^-$ channel.

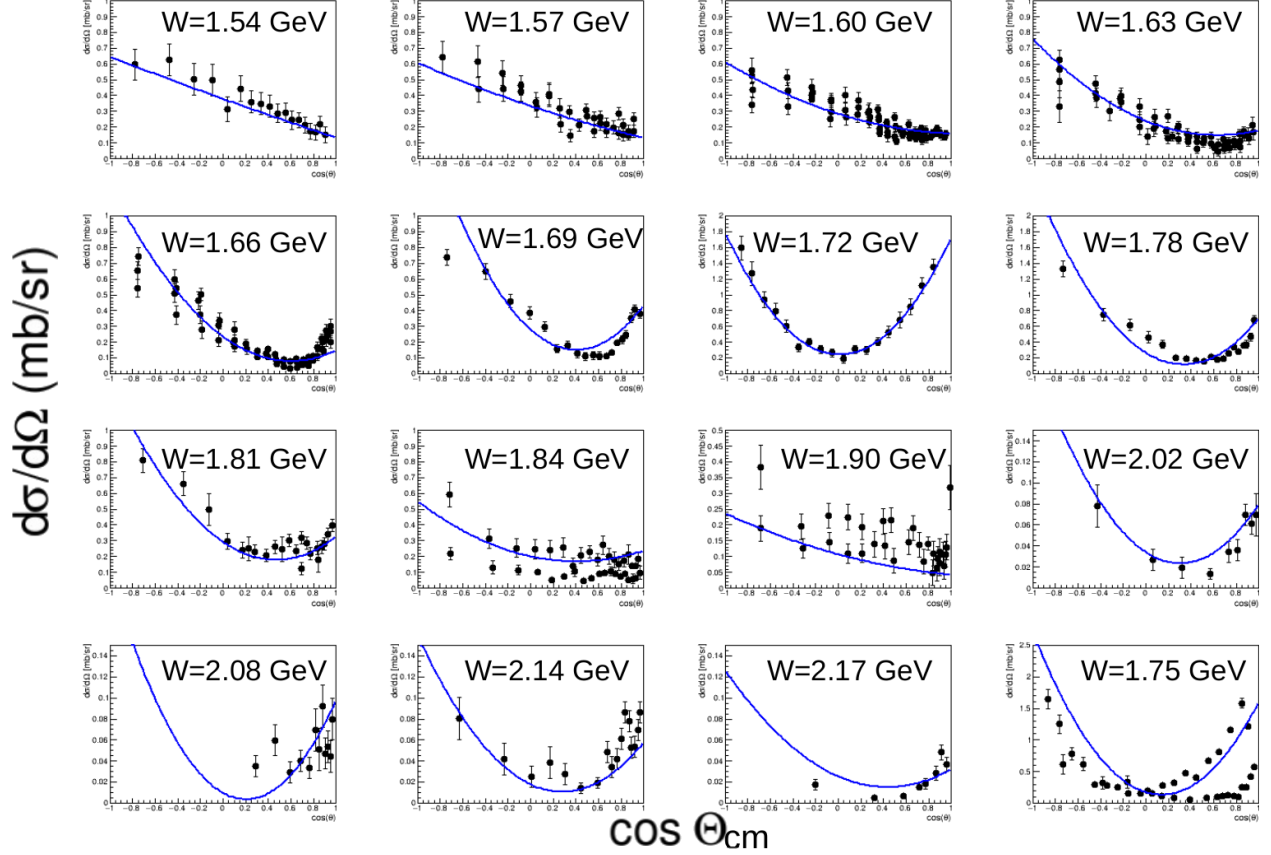


Figure 46: Differential cross section plots for $K_L p \rightarrow K_S p$ as a function of W . The blue curves are the result of a parametrization of the cross section in terms of Legendre polynomials. The measured data are from [165].

A5.5 Details of MC study for $K_L p \rightarrow \pi^+ \Lambda$

The $K_L p \rightarrow \pi^+ \Lambda$ and $K_L p \rightarrow \pi^+ \Sigma^0$ reactions are key to studying hyperon resonances – an analog of $N\pi$ reactions for the N^* spectra. They are also the key reaction to disentangling the weak exchange degeneracy of the $K^*(892)$ and $K^*(1420)$ trajectories. (A general discussion is given in Sec. 5). The first measurement of this reaction was performed at SLAC in 1974 [134] for K_0 beam momentum range between 1 GeV/ c to 12 GeV/ c . The total number of $\pi^+ \Lambda$ events was about 2500 events, which statistically limits the measurement.

For our proposed KL Facility at Hall-D, we expect a great increase in the statistics of $K_L p \rightarrow \pi^+ \Lambda$ for a very wide range of K_L beam momentum. Figure 50 shows the K_L beam momentum distributions from the generated counts (left) and reconstructed counts (right) when requiring $\beta_{K_L} > 0.95$ in time-of-flight.

We have generated the $K_L p \rightarrow \pi^+ \Lambda$ reaction taking into account the realistic K_L beam momentum distribution in the event generator. This momentum spectrum is a function of the distance and angle. Events were processed through the standard Hall-D GEANT simulation with GlueX detector

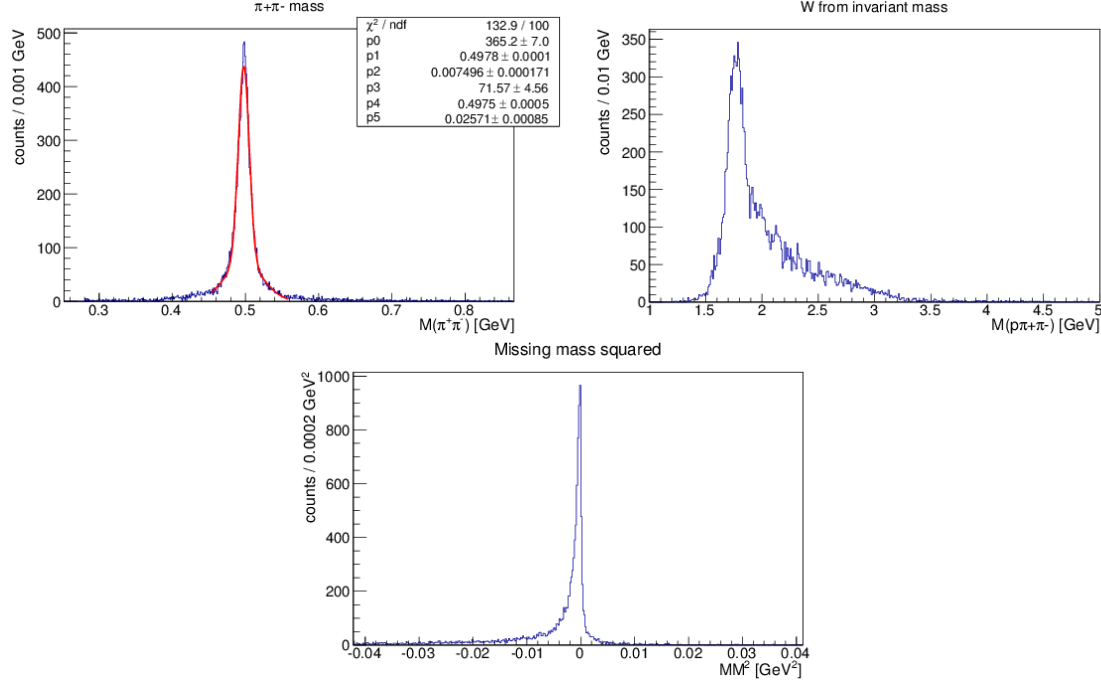


Figure 47: Full reconstruction for $K_L p \rightarrow K_S p$ and $K_S \rightarrow \pi^+ \pi^-$. Top left panel: $\pi^+ \pi^-$ invariant mass. Top right panel: W computed from $\pi^+ \pi^- p$ invariant mass. Bottom panel: Missing-mass squared for the full reaction.

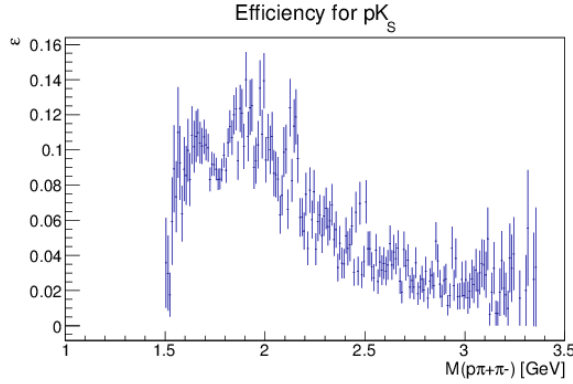


Figure 48: Estimate the efficiency for full reconstruction of the $K_L p \rightarrow K_S p$ and $K_S \rightarrow \pi^+ \pi^-$ reaction chain as a function of W .

and momentum smearing and utilized JANA for particle reconstruction that was simulated. Figure 51 shows a sample plot for polar angle versus momentum distribution of π^+ , π^- , and protons from the generated event (left) and reconstructed event (right).

Figure 52 shows an example of the reconstructed the Λ invariant mass (left) and missing mass (right). We obtained a 5 MeV invariant-mass resolution and a 150 MeV missing-mass resolution and estimated the expected total number of $\pi^+ \Lambda$ events as final-state particle within topology of $1\pi^+$, $1\pi^-$, and 1 proton. In 100 days of beam time with 1×10^4 K_L /s on the liquid hydrogen target, we expect to detect around 5.3M $K_L p \rightarrow \pi^+ \Lambda$ events for $W < 3$ GeV. Such an unprecedented statistics will improve our knowledge of these states through PWA.

The $K_L p \rightarrow \pi^+ \Lambda$ reaction has a relatively high production cross section the order of a few mb

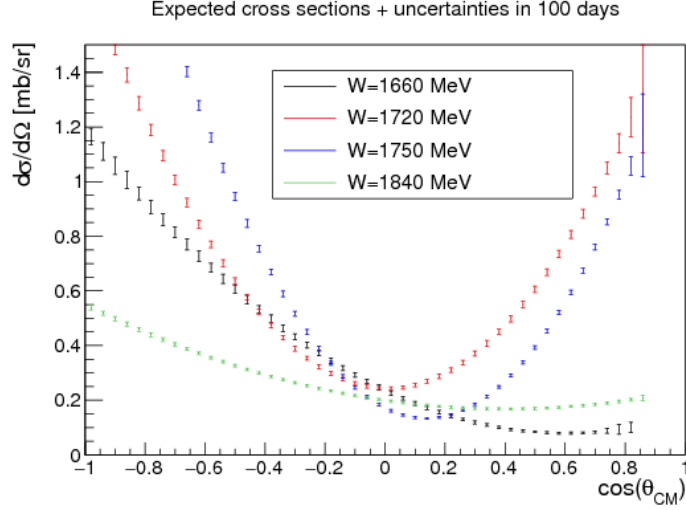


Figure 49: Reconstructed $K_{Lp} \rightarrow K_{Sp}$ differential cross sections for various values of W for 100 days of running.

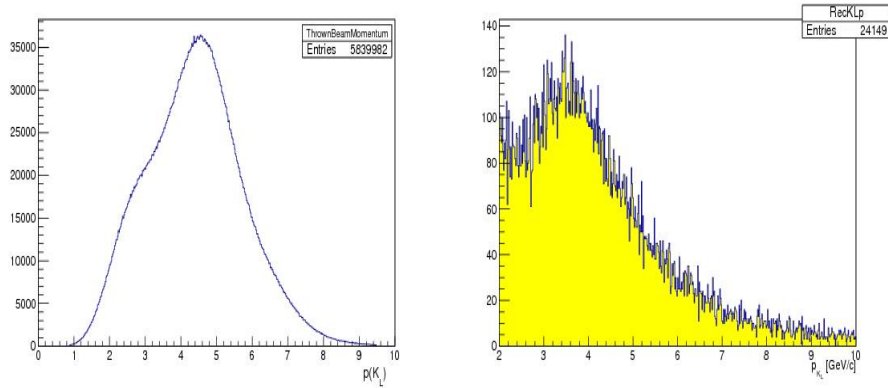


Figure 50: Beam particle (K_L) momentum distribution in MC simulation, Left panel: Generated. Right panel: Reconstructed.

in our proposed K_L -momentum range (1 – 6 GeV/c). The beam resolution has been calculated at the time-of-flight vertex time resolution (250 ps) of the start counter (TOF-ST). The estimates of the statistical uncertainty of the $\pi^+\Lambda$ total cross section as a function K_L beam momentum with GlueX detector in Hall-D are shown in Fig. 53 (left). We kept the same momentum bin size as the one from the SLAC data. The box-shaped error bars in the MC points (red triangles) were increased by a factor of 10 for comparison with the SLAC data. The proposed measurements will provide unprecedented statistical accuracy to determine the cross section for a wide range of K_L -momentum. In Fig. 53 (right), the t -dependent cross sections were shown in three beam momentum bins same as SLAC data sets: $p_{K^0} = 1.5 - 2.5$ GeV/c (solid bullets), $p_{K^0} = 2.5 - 3.5$ GeV/c (solid rectangles) and $p_{K^0} = 3.5 - 5.0$ GeV/c (solid triangles). As it shows, a strong forward peaking in t -channel for all momenta was observed, which appears to move out $|t| = 0.4 - 0.5$ GeV² at higher momenta.

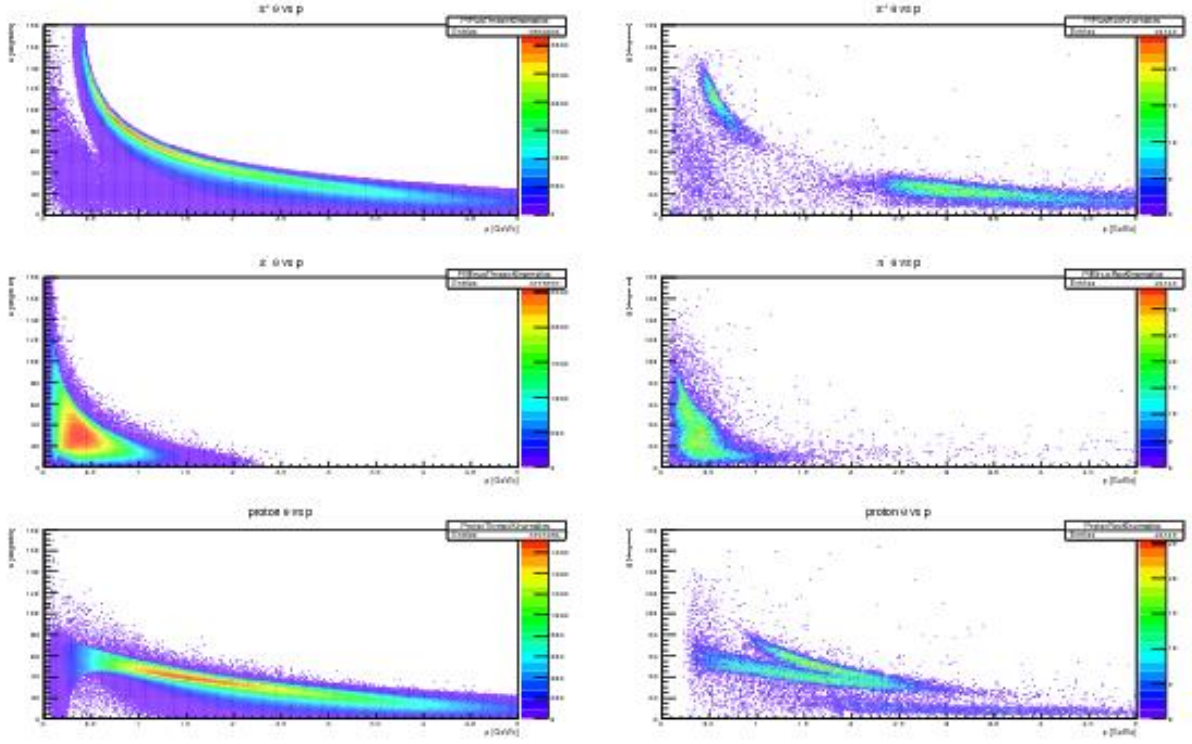


Figure 51: Momentum and angular distributions. Top row panel: π^+ , Middle row panel: π^- , Bottom row panel: proton. Left column panels: Generated and Right column panels: Reconstructed events.

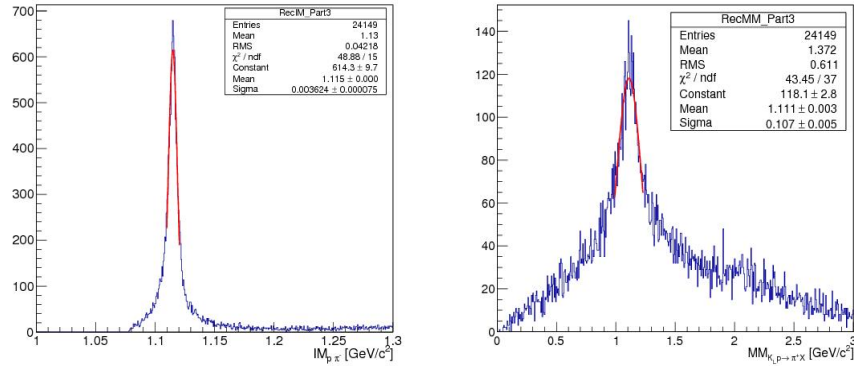


Figure 52: Λ invariant-mass distribution reconstructed. Left panel: From its $\pi^- p$ decay particles. Right panel: Missing mass of $\pi^+ X$ (right).

Parity violation in the weak decay of Λ makes it possible to measure the induced polarization. The induced Λ polarization (P_Λ) can be observed by measuring the angular distribution of the proton with respect to the normal vector to the production plane. As one can see in Sec 4.9 (Fig. 6), the recoil polarization is extremely sensitive and valuable tool to constrain PWA amplitudes. Our sim-

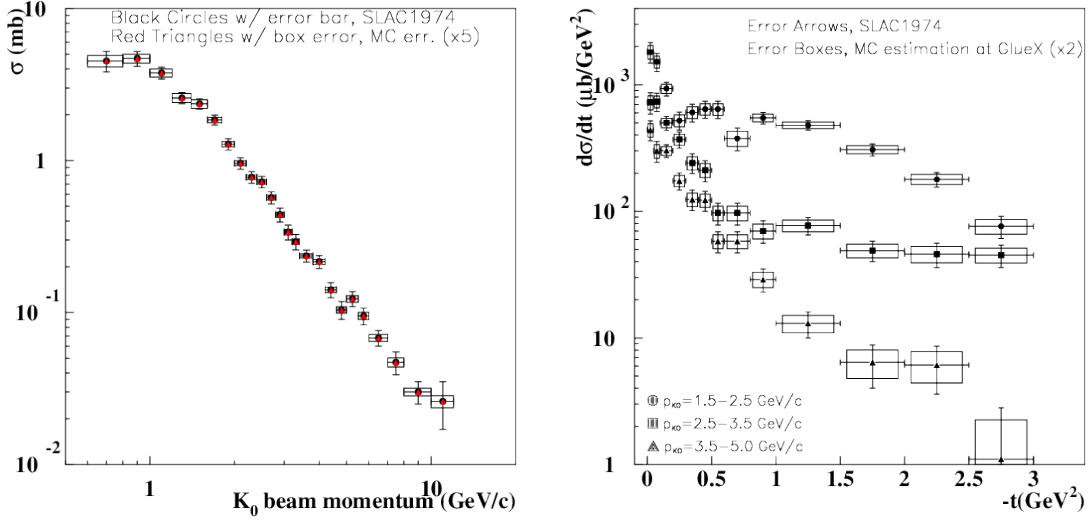


Figure 53: Left panel: Total cross section uncertainty estimate (statistical uncertainty only) for $K_L p \rightarrow \pi^+ \Lambda$ reaction as a function of K_L beam momentum in comparison with SLAC data [134]. The experimental uncertainties have tick marks at the end of the error bars. The box-shaped error bars in the MC points from K_L beam at GlueX were increased by a factor of 5. Right panel: t -dependent cross sections in three beam momentum bins (same as SLAC data sets): $p_{K^0} = 1.5 - 2.5$ GeV/c (solid bullets), $p_{K^0} = 2.5 - 3.5$ GeV/c (solid rectangles) and $p_{K^0} = 3.5 - 5.0$ GeV/c (solid triangles). The box-shaped error bars in the MC points from K_L beam at GlueX detector were increased by a factor of 2.

ulations show that existing SLAC data can be improved a lot by K_L facility at JLab (see Fig. 54).

The major source of systematic uncertainty for this reaction would be a particle miss-identification among π^+ , K^+ , and protons in the final state. However, requiring the reconstructed Λ and side-band subtraction technique for background will reduce contributions from misidentified events substantially.

A5.6 Details of MC study for $K_L p \rightarrow K^+ \Xi^0$ and $K_L n \rightarrow K^+ \Xi^-$

The study of cascade data will allow us to place stringent constraints on dynamical coupled-channel models. It was recently found in N^* spectroscopy that many N^* resonances do not couple strongly to a $N\pi$ channel, but are nicely seen in $K\Lambda$ and $K\Sigma$ channels. The corresponding situation in hyperon spectroscopy leads to many Λ^* and Σ^* resonances decaying preferably to a $K\Xi$ channel (see Sec 4.9 for details). In addition, cascade data will provide us with long-sought information on missing excited Ξ states and the possibility to measure the quantum numbers of the already established $\Xi(1690)$ and $\Xi(1820)$ from a double-moments analysis. The expected large data sample will allow us to determine the induced polarization transfer of the cascade with unprecedented precision, which will place stringent constraints on the underlying dynamics of the reaction. Po-

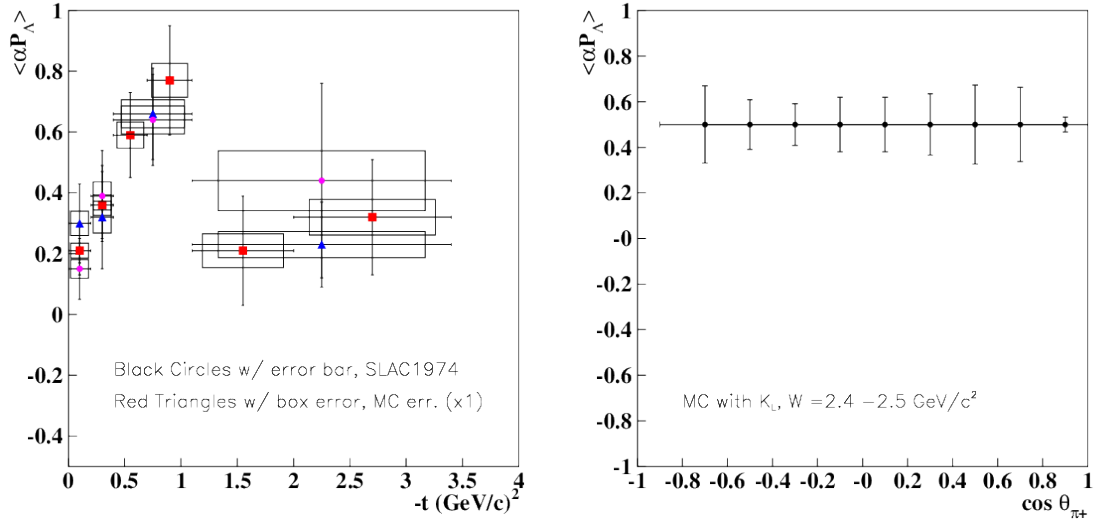


Figure 54: Left panel: Averaged polarization, $\langle \alpha P_\Lambda \rangle$ as a function of t from Ref. [134], $p_{K^0} > 2.5 \text{ GeV/c}$ (red boxes), $p_{K^0} = 2.5 - 3.8 \text{ GeV/c}$ (blue triangles) and $p_{K^0} > 3.8 \text{ GeV/c}$ (purple bullets). The experimental uncertainties have tick marks at the end of the error bars. The box-shaped error bars from the MC for the K_L beam at GlueX, assuming 100 days beamtime. $\alpha = 0.645$ is the Λ analysing power. Right panel: Estimates of the statistical uncertainties of the Λ polarization as a function of CM $\cos \Theta_{\pi^+}$ for the $W = 2.4 - 2.5 \text{ GeV}$ energy bin.

polarization measurements of hyperons shed light on the contribution from individual quarks to the overall polarization of these states. The polarization of the ground-state cascade can be measured from its weak decay in a straightforward way. With a K_L beam, the study of the reactions $K_L p \rightarrow K^+ \Xi^0$ and $K_L n \rightarrow K^+ \Xi^-$ is quite simple and an unprecedented statistical sample can be easily obtained. The statistical uncertainty obtained for two-fold differential polarization observables with 100 days of beam time ($\sim 1 \times 10^5$ reconstructed events) is of the order of 0.05–0.1, which will allow precision tests on the underlying dynamics to be performed. It also will be a first measurement of this kind.

A5.6.1 $K_L p \rightarrow K^+ \Xi^0$:

The section here focuses on the reconstruction of $K_L p \rightarrow K^+ \Xi^0$ but the initial procedure for particle identification and reaction reconstruction is almost identical to the reaction on the neutron ($K_L n \rightarrow K^+ \Xi^-$). Three topologies can be used to reconstruct the reaction $K_L p \rightarrow K^+ \Xi^0$ on free proton targets. Topology 1 requires the detection of a K^+ , topology 2 requires the detection of a K^+ and a Λ by utilizing its high branching ratio to a $\pi^- p$ pair (63.9 %), and Topology 3 requires the detection of the two-photon decay of the π^0 from $\Xi \rightarrow \pi^0 \Lambda$. Particle identification is done via a probabilistic approach involving dE/dX , time-of-flight, and track curvature information. The dE/dX distributions for kaon, proton, and π^- candidates are shown in Fig. 55.

At low particle momenta, kaons and protons can be well separated, but high-energy particles can-

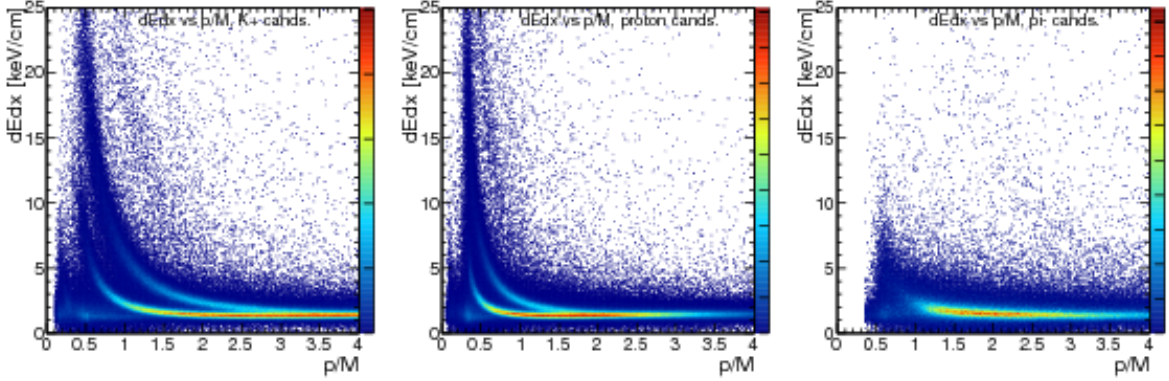


Figure 55: dE/dX distributions used in kaon proton and π^- identification for the reconstruction of $K_L p \rightarrow K^+ \Xi^0$.

not be unambiguously differentiated by dE/dX or by ToF information, which leads to particle misidentification. The higher the W , the higher ejectile energy and the more misidentification contributions we have. In this analysis (specifically Topology 2 and 3), these events were largely removed by making an invariant-mass cut on the $\pi^- p$ pair.

Figure 56 shows the missing mass of $K_L p \rightarrow K^+ X$ for simulated data for the reaction $K_L p \rightarrow K^+ \Xi^0$ used in the reconstruction of all topologies, the invariant-mass distribution of the $\pi^- p$ pair used to reconstruct Topology 2 ($K_L p \rightarrow K^+ \Lambda X$) and 3, and the invariant-mass of the two-photon pair used to reconstruct Topology 3 ($K_L p \rightarrow K^+ \Lambda \pi^0$). A 3σ cut on these distributions allows us to reconstruct the reaction fully. Fig. 56 (left) shows the 3σ W -dependent cut applied to select the missing Ξ^0 as well as the W -dependent 3σ cut to reconstruct the reaction $K_L p \rightarrow K^+ n$. The latter is one of the major sources of background for our reaction for Topology 1; however, the missing-mass resolution (obtained with a vertex-time resolution of 250 ps) allows a clean separation of these two reactions up to $W = 2.3$ GeV. Above this value, special treatment of the $K_L p \rightarrow K^+ n$ background is required as discussed later on.

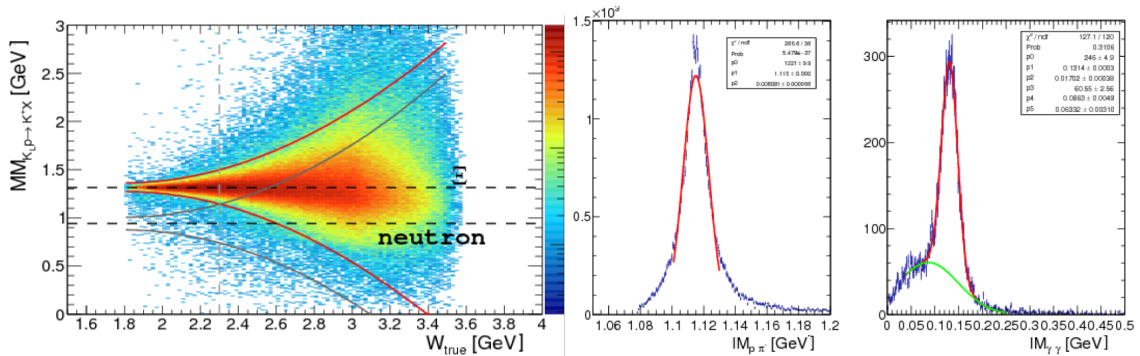


Figure 56: Missing mass of the reaction $K_L p \rightarrow K^+ X$ used to reconstruct the reaction $K_L p \rightarrow K^+ \Xi^0$ (Topology 1), and the invariant mass of $p\pi^-$ pair (Topology 2), and the invariant mass of the two-photon pair (Topology 3).

The detection efficiency as a function of the true W for each topology for the reaction on the proton

is shown in Fig. 57. As expected, the efficiency is highest for Topology 1 reaching a maximum at 60 % for $W = 2.05$ GeV. The efficiency for Topology 2 is about an order of magnitude less than Topology 1, and Topology 3 detection efficiency is on average 0.8 %. The efficiency for the reaction on the neutron for a fully exclusive reaction is of the order of a few percent.

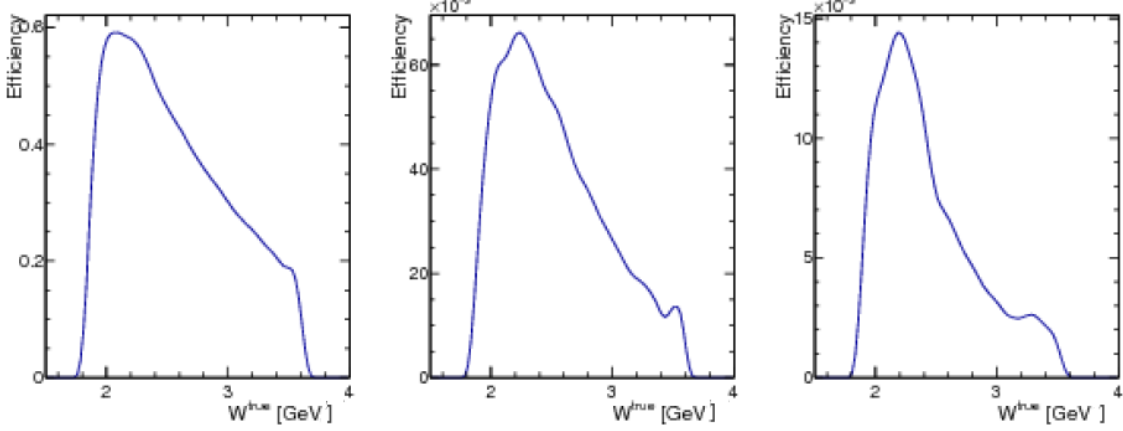


Figure 57: Detection efficiency for the reaction $K_L p \rightarrow K^+ \Xi^0$ for each topology.

In 100 days of beamtime, we expect 3×10^6 $K_L p \rightarrow K^+ \Xi^0$ events. Out of which, one can reconstruct 2×10^6 events for Topology 1 ($K_L p \rightarrow K^+ X$); 1×10^5 for Topology 2 ($K_L p \rightarrow K^+ \Lambda X$); and 2×10^4 for Topology 3 ($K_L p \rightarrow K^+ \Xi^0$). Figure 58 compares the statistical uncertainties of the total and differential cross sections for the reaction $K_L p \rightarrow K^+ \Xi^0$ with existing data taken from [166] for the three different topologies (column 1: only K^+ reconstructed, column 2: $K^+ \Lambda$ reconstructed, and column 3: $K^+ \Xi^0$ reconstructed).

Different sources of background will contribute in the three topologies used to study this reaction. Disentangling our signal $K_L p \rightarrow K^+ \Xi^0$ from the reaction $K_L p \rightarrow K^+ n$ (crucial for Topology 1), which has two orders of magnitude larger cross section is expected to be relatively straightforward. As mentioned before, a simple missing-mass cut is sufficient to remove any contributions from this reaction for $W < 2.3$ GeV. For $W > 2.3$ GeV, an s-weight approach (or neuralNets, etc.) can be utilized to remove these contribution as the shape of the background under any cascade events can be well established from simulations. Figure 59 shows the W -dependence of the missing-mass distribution of $K_L p \rightarrow K^+ X$ for the simulated reactions $K_L p \rightarrow K^+ \Xi^0$ and $K_L p \rightarrow K^+ n$ (left panel). The right panel shows the missing-mass projection at $W = 1.9$ GeV. In addition to $K_L p \rightarrow K^+ n$, the reaction $K_L p \rightarrow \pi^+ \Lambda$ is also a source of background events for Topology 1 ($K_L p \rightarrow K^+ X$) and 2 ($K_L p \rightarrow K^+ \Lambda X$). This channel contributes when the final-state π^+ is misidentified as a K^+ . This shifts the missing mass of $K_L p \rightarrow \pi^+ X$ to values lower than the ones expected, which leads to a good separation of this source of background below $W < 2.2$ GeV. Figure 60 shows the missing-mass distribution of these misidentified events, which show similar distribution with $K_L p \rightarrow K^+ n$ events. Contributions from these events for Topology 3 is completely removed by the requirement of two photons in the final state that reconstruct the mass of π^0 . For Topology 2, coplanarity cuts between the reconstructed (misidentified) K^+ and Λ can reduce contributions, whereas a background subtraction approach using the missing-mass information can be used to remove any contribution at $W > 2.2$ GeV.

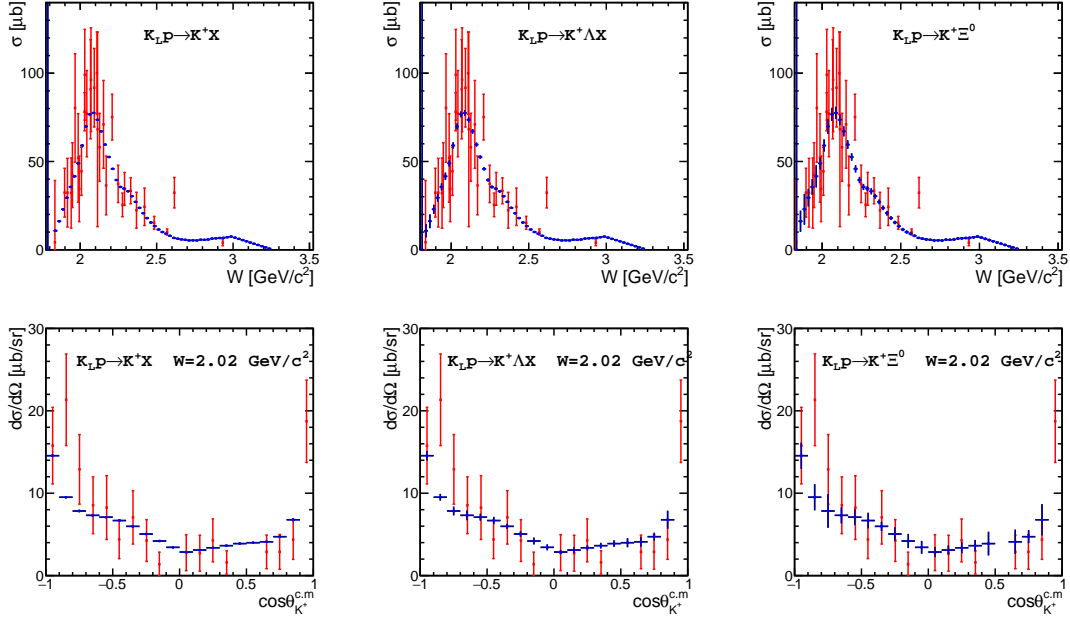


Figure 58: Total and differential cross section statistical uncertainty estimates (blue symbols) for the three topologies (column 1: only K^+ reconstructed, column 2: $K^+\Lambda$ reconstructed, and column 3: $K^+\Xi^0$ reconstructed) in comparison with data taken from Ref. [166] (red symbols).

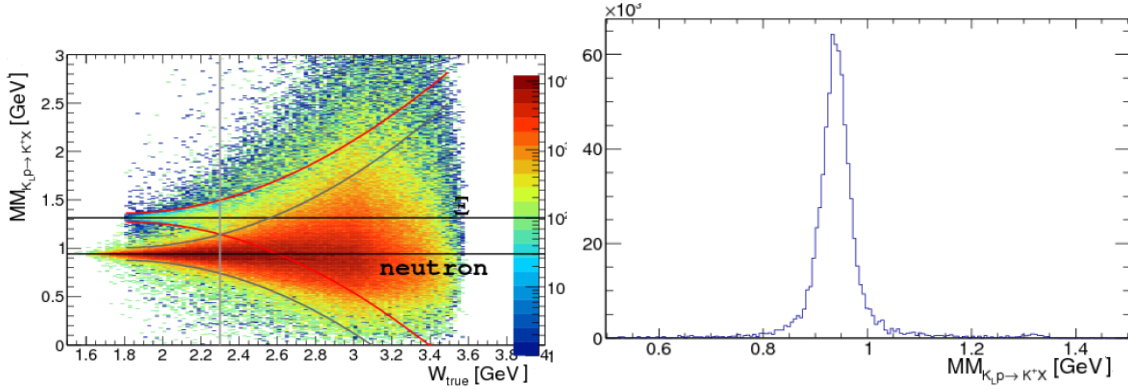


Figure 59: Missing mass of the reaction $K_L p \rightarrow K^+ X$ used to reconstruct the reactions $K_L p \rightarrow K^+ \Xi^0$ (Topology 1) and $K_L p \rightarrow K^+ n$ (which has about 2 orders of magnitude larger cross section). Right panel shows the missing mass at $W = 1.9$ GeV.

Ξ^0 induced polarization: The expected statistics also allow us to determine the cascade-induced polarization by utilizing the fact that the cascade is self-analyzing with an analyzing power of -0.406 [3].

In terms of four-vectors, conservation of energy and momentum for this reaction is written as follows:

$$\mathcal{P}_{K_L} + \mathcal{P}_p = \mathcal{P}_{K^+} + \mathcal{P}_{\Xi^0}. \quad (9)$$

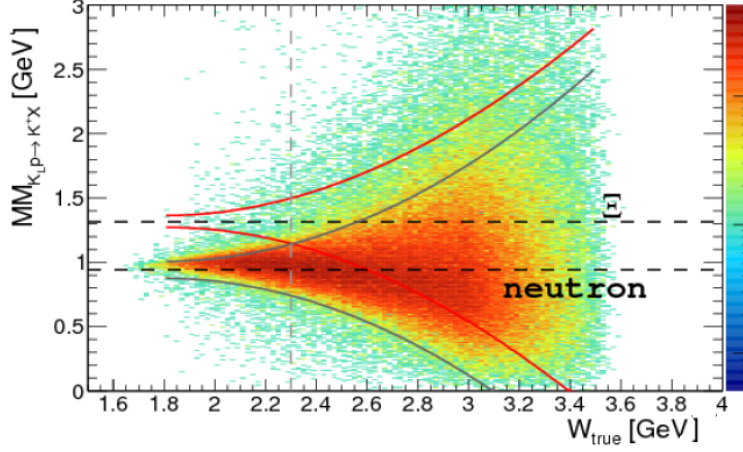


Figure 60: Missing mass of the reaction $K_L p \rightarrow K^+ X$ for simulated events from the reaction $K_L p \rightarrow \pi^+ \Lambda$. The reconstructed events here results from a pion misidentified as a kaon.

The production plane is then defined by

$$\hat{y} = \frac{\vec{P}_\Xi \times \vec{P}_{K_L}}{|\vec{P}_\Xi \times \vec{P}_{K_L}|}. \quad (10)$$

The \hat{z} axis lies along the beam direction

$$\hat{z} = \frac{\vec{P}_{K_L}}{|\vec{P}_{K_L}|}, \quad (11)$$

and thus the \hat{x} axis is defined to give a right-handed coordinate system:

$$\hat{x} = \hat{y} \times \hat{z}. \quad (12)$$

The determination of P_Ξ^y can be established by linear fits to the acceptance-corrected pion angular ($\cos \theta_\pi^y$) yields. Fitting these distributions with a first-degree polynomial,

$$y = a_0(1 + a_1 \cos \theta_\pi^y), \quad (13)$$

allows the determination of a_1 , which gives us the induced polarization

$$a_1 = P_\Xi^y \alpha. \quad (14)$$

Alternatively, one can determine the induced polarization transfer from determining the forward-backward asymmetry, A^y , of the pion angular distribution. This asymmetry is defined as

$$A^y = \frac{N_+^y - N_-^y}{N_+^y + N_-^y}, \quad (15)$$

where N_+^y and N_-^y are the acceptance-corrected yields with $\cos \theta_\pi^y$ positive and negative, respectively. The asymmetry is related to the induced polarization by

$$P_\Xi^y = \frac{-2A^y}{\alpha}. \quad (16)$$

The statistical uncertainty in the asymmetry measurement of P_{Ξ}^y is related to the Poisson uncertainty in N_+^y and N_-^y . Propagating this uncertainty to the uncertainty of A^y gives

$$\sigma_{A^y} = \frac{2}{(N_+^y + N_-^y)^2} \sqrt{N_+^y N_-^y (N_+^y + N_-^y)}. \quad (17)$$

The uncertainty in P_{Ξ}^y is then found by propagating σ_{A^y} and σ_{α} :

$$\frac{\sigma_{P_{\Xi}^y}}{P_{\Xi}^y} = \sqrt{\left(\frac{\sigma_{A^y}}{A^y}\right)^2 + \left(\frac{\sigma_{\alpha}}{\alpha}\right)^2}. \quad (18)$$

The above procedure is identical to the case of Ξ^- where the angle $\cos \theta_{\pi}^y$ is given by the negative pion from the cascade decay, in the Ξ^- rest frame.

Figure 61 shows the statistical uncertainty estimates of the induced polarization of the cascade by simple fits to the acceptance-corrected yields of the pion angular distribution in the Ξ^0 rest frame.

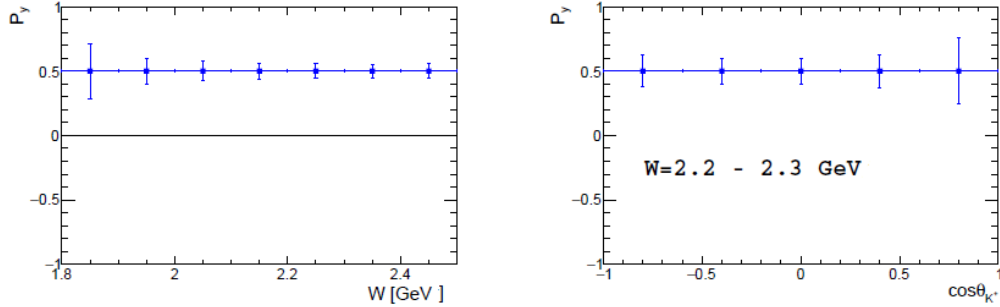


Figure 61: Estimates of the statistical uncertainties of the induced polarization of the cascade in a $K_L p \rightarrow K^+ \Xi^0$ reaction as a Left panel: Function of W (one-fold differential). Right panel: Function of CM $\cos \theta_{K^+}$ (two-fold differential).

A5.6.2 $K_L p \rightarrow K^+ \Xi^-$:

The analysis of this reaction on the neutron is based on the same approach as the one described above for $K_L p \rightarrow K^+ \Xi^0$. The main difference comes from the momentum distribution of the target nucleon. This issue can be easily addressed by selecting semi-exclusive events having only the spectator proton undetected. The analysis requires the detection of all final-state particles besides spectator, namely the K^+ , the π^- from the cascade decay and the proton and π^- from the Λ decay. Even though this condition reduces the available statistics, the W resolution can be kept high.

The reconstruction of $K_L n \rightarrow K^+ \Xi^-$ follows closely the steps outlined for the reaction on the proton $K_L p \rightarrow K^+ \Xi^0$. The identification of the pions that originates from the Λ and Ξ decays is the main difference between the two channels. Fig. 62 (left) shows the invariant mass between the proton and one of the two detected pions. It is clear from this that the pion that originates from the Λ is easily identified with minimal combinatorial background.

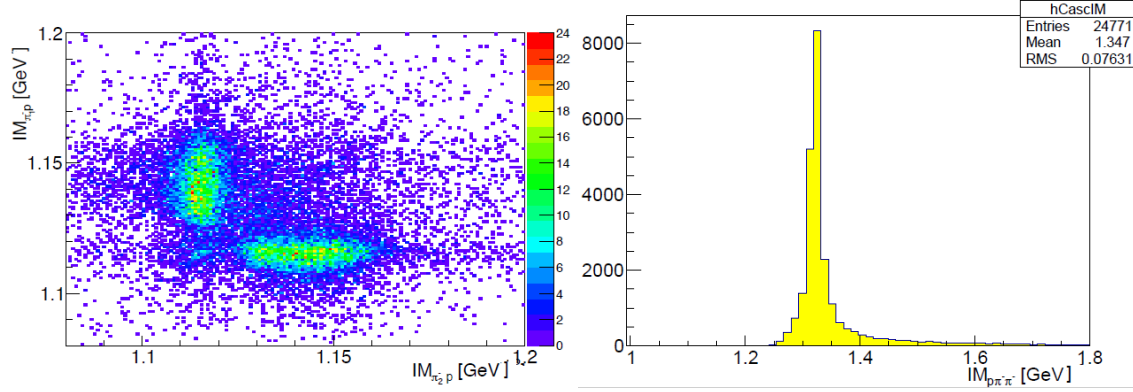


Figure 62: Left panel: Invariant mass of detected proton and π_1^- as a function of Invariant mass of detected proton and π_2^- . Right panel: Invariant mass of detected proton and two π^- .

The invariant mass of two pions and the proton is shown in Fig. 62 (right), clearly reconstructing the Ξ^- mass. Determination of cross sections and the induced polarization is identical to the $K_L p \rightarrow K^+ \Xi^0$ channel.

Based on the models described in Sec. 4.9, polarized data on the reaction $K_L n \rightarrow K^+ \Xi^-$ were generated. In 100 days of beamtime, we expect to produce several million events (between 3 and 10) depending on the two available solutions, which give very different predictions. From this, the reconstruction of 7×10^4 or 3×10^5 events is expected for the fully exclusive reaction selection. In the same manner as the reaction on the proton ($K_L p \rightarrow K^+ \Xi^0$), we will utilize the fact the cascade is self-analyzing with an analyzing power of -0.458 [3]. The statistical uncertainties obtained over a period of 100 days for the induced cascade polarization are illustrated in Fig. 63 (left). Expected statistical significance for the model separation at the same W-bin as a function of experiment duration is shown in Fig. 63 (right). In this particular case, a 100 days experiment would reach a decisive level of 7.6σ separation power, compared to only a 3.5σ separation after 20 days.

It is evident that the determination of P_y will place very stringent constraints on the available models. The statistical uncertainties obtained over a period of 100 days are sufficient to investigate the underlying dynamics and cleanly differentiate between leading theoretical predictions.

The exclusivity of the reaction allows us to obtain a much cleaner sample of events with minimal background contributions. This will be done by requiring the invariant mass of the proton and the two negative pions to be consistent with the mass of Ξ^- . An additional requirement that the invariant mass of the proton-pion pair be consistent with the mass of the Λ will eliminate any background contributions other than the excited cascade channels. Contributions from excited cascade states can also be identified and removed by the application of coplanarity cuts between the strange meson and reconstructed cascade. Excited cascade states $K_L n \rightarrow K^+ \Xi^{*-}$ can also be identified, isolated, and studied in detail using the missing-mass technique assuming the target nucleon at rest.

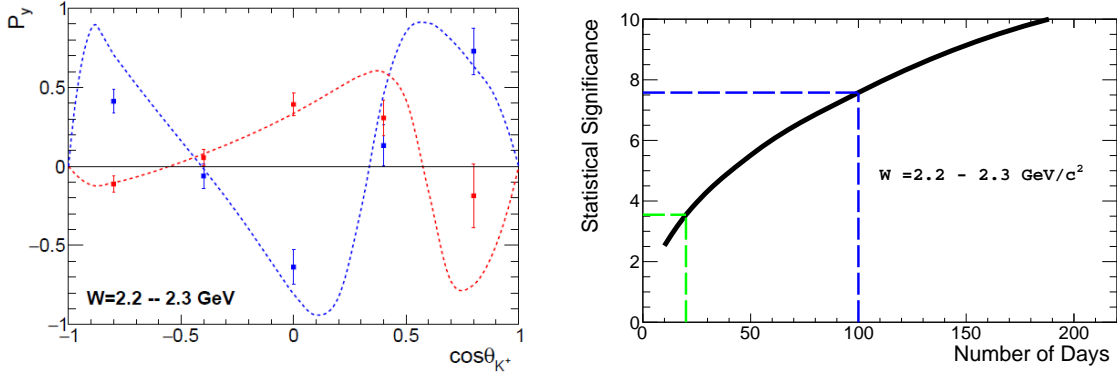


Figure 63: Left panel: Estimated statistical uncertainties of the induced polarization of the Ξ^- in a $K_L n \rightarrow \bar{K}^+ \Xi^-$ reaction as a function of CM $\cos \theta_{K^+}$ (two-fold differential). The curves show the theoretical predictions based on two solutions as described in Sec. 4.9. Right panel: Expected statistical significance, in units of σ_s , to distinguish two models as a function of the running time. Two benchmark cases of 20 and 100 days are highlighted by the dashed green and blue curves, respectively.

A5.7 $K_L n \rightarrow K^+ \Xi^{*-}$:

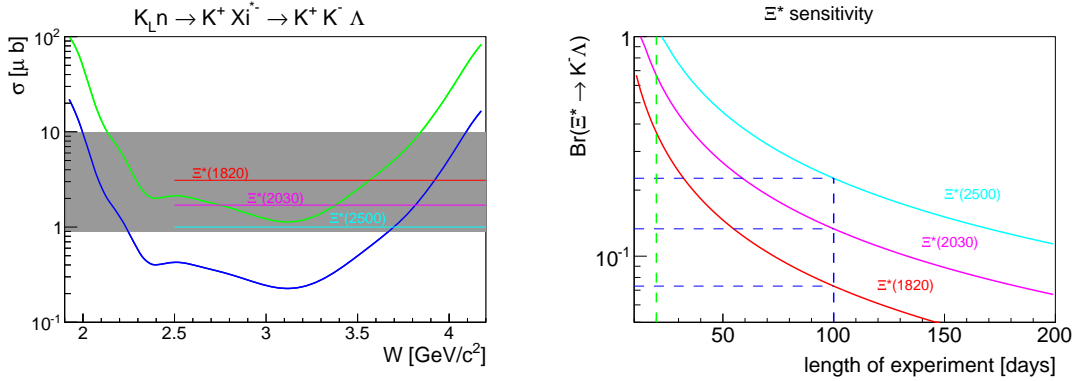


Figure 64: Left panel: The Ξ^* discovery potential achievable at KLF during the 100 (blue) and 20 (green) day experiment, under assumption of 10 % statistical accuracy and $Br(\Xi^* \rightarrow \bar{K} \Lambda) = 1$. The gray band corresponds to typical Ξ^* cross sections and horizontal lines are few examples of BNL cross sections from Ref. [167] Right panel: Estimation of lowest measurable $\Xi^* \rightarrow \bar{K} \Lambda$ branching fraction at KLF as a function of experiment duration at $W \sim 3.100 \pm 0.025$ GeV. Two benchmark cases of 100 (20) days are highlighted by dashed blue (green) curves.

The spectrum of excited cascades is barely known and practically nothing is known about their quantum numbers (see Chapter 3.2 for theory overview). To understand the ability of the KLF to contribute in this field, we have performed a series of simulations. The production of Cascades is always accompanied with kaons (K^+ or K^0) due to strangeness conservation. We have concentrated on reactions with the K^+ only to avoid unnecessary complications arising from the K^0 secondary decay vertexes. With K_L beam and associated K^+ one can produce either Ξ^{*0} on a proton target ($K_L p \rightarrow K^+ \Xi^{*0}$) or Ξ^{*-} on a neutron target ($K_L n \rightarrow K^+ \Xi^{*-}$). In both cases, the

Ξ^* properties are reconstructed from the final-state particles; hence, any minor differences due to the spectator momentum do not play any role. A dominant Ξ^{*-} decay branch is $\Xi^* \rightarrow \bar{K}\Lambda$. The Ξ^{*-} production looks more attractive since it has direct $\Xi^{*-} \rightarrow K^-\Lambda \rightarrow K^-p\pi^-$ decay with only one detached vertex from Λ decay. The full reaction contains four particles in the final state $K_L n \rightarrow K^+\Xi^{*-} \rightarrow K^+K^-p\pi^-$ all of different types, which simplifies the analysis. Two negative pions - one from the Λ decay and one from the \bar{K}^0 and an extra detached vertex sufficiently complicates the analysis of this branch on proton target. Here we will present only the simplest case $K_L n \rightarrow K^+\Xi^{*-}$ leaving other options for future studies.

The energy dependence of the $K_L N \rightarrow K^+\Xi^{*-}$ is not known. From the BNL measurements given in Ref. [167], we know that the Ξ^{*-} production cross section should be on the order of $1 - 10 \mu b$ - the higher the Ξ^* mass the lower the cross section, from $3.7 \mu b$ for the $\Xi^*(1820)$ to $1 \mu b$ for the $\Xi^*(2500)$. Some exotic cascades might have even lower production cross sections. We have tried to evaluate what Ξ^* production cross sections that might be measurable at K_L -facility within 20 and 100 days. We consider a lower bound of 10 % statistical uncertainty for the Ξ^* states to be identified. The results of our analysis can be seen in Fig. 64 in comparison with typical Ξ^* cross sections from Ref. [167]. From $N^* \rightarrow \pi N$ studies, it is known that for the high mass N^* states the $N^* \rightarrow \pi N$ branch get suppressed in favour of multi-pion ladder decays. A similar effect is expected to be seen for the high-mass Ξ^* . According to PDG, the $\Xi^* \rightarrow \bar{K}\Lambda$ is “dominant” for many Ξ^* states, however, we need to be prepared to measure somewhat suppressed $\Xi^* \rightarrow \bar{K}\Lambda$ decay of heavy Ξ^* ’s. A W -variation of the Ξ^* production cross-section provide an important information on $\Xi^* \rightarrow \bar{K}\Lambda^*$ and $\Xi^* \rightarrow \bar{K}\Sigma^*$ couplings as an inverse process allowing further insight into Ξ^* internal structure.

To summarize: with 20 days beamtime one can barely touch the lowest-lying Ξ^* resonances keeping quantum numbers determinations, which requires precise measurements of the differential observables and Λ recoil polarization, out of consideration. With 100 days beamtime, all Ξ^* resonances could be measured with a statistical significance sufficient not only for the determination of mass and width parameters but also for spin-parity assignments as well.

A5.8 Details of MC study for $K_L p \rightarrow K^+ n$

The $K_L^0 p \rightarrow K^+ n$ reaction is a very special case in kaon-nucleon scattering. Due to strangeness conservation, formation of intermediate resonances is forbidden for this reaction. The main contribution comes from various non-resonant processes, which can be studied in a clean and controlled way. Similar non-resonant processes can be seen in other reactions where they can interfere with hyperon production amplitudes, causing distortion of the hyperon signals. That is why knowledge of the non-resonant physical background is important not only for the kaon-induced reactions but for all reactions with strangeness. The non-resonant nature of the reaction does not guarantee the absence of bumps in the total cross section: kaons and/or nucleons can be excited in the intermediate stage, producing bumps in the total cross section.

The reaction $K_L^0 p \rightarrow K^+ n$ is simple and has a very high production cross section (see Fig. 65); nevertheless, data on this reaction are scarce. It is a bit simpler to perform a positive kaon beam scattering for the inverse reaction, however, the reaction on a neutron target involves final-state

interactions that may complicate the analysis. That is why the inverse reaction is also not so well known. A fair amount of differential cross-section data are available in the range $0.5 < p_{K_L} < 1.5$ GeV/c, predominantly from bubble chambers (see Ref. [229]) and there are a few measurements at high momenta: $p_K = 5.5$ GeV/c [168], $p_K = 10$ GeV/c [169]. In the energy range $2 < W < 3.5$ GeV, which can be covered by the KLF experiment with very high statistics, there are no data on this reaction at all.

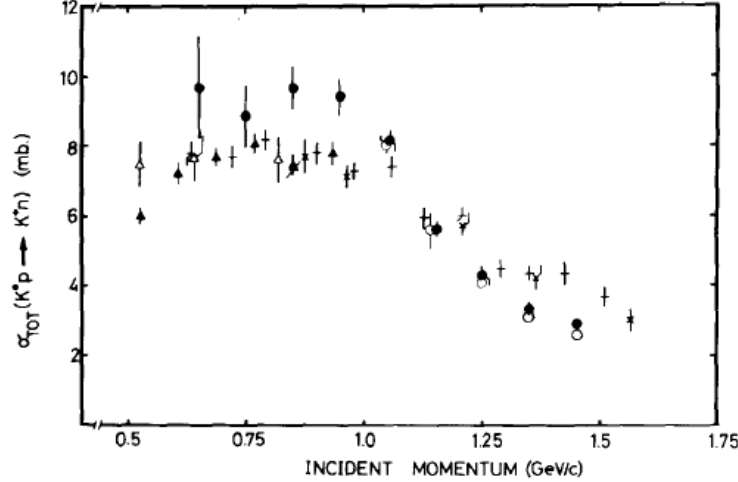


Figure 65: Total cross section for $K_L p \rightarrow K^+ n$ reaction as a function of K_L -momentum from Ref. [229].

Detection of the charged kaon is enough to reconstruct the reaction fully via the missing-mass technique. If the beam energy is determined by ToF method utilizing the 24 m flight path between the kaon production Be-target and the reaction hydrogen target, the beam resolution is driven by the ST time resolution.

In addition to a kaon, one could also detect a neutron; however, due to poor neutron detection efficiency and the large systematic uncertainties associated with neutron detection, an improvement in the reconstruction of the reaction with this approach may be problematic. As described before, kaon identification is done with a probabilistic approach involving dE/dX , time-of-flight, and track curvature information. Even in pure $K_L p \rightarrow K^+ n$ MC case one can have more than one charged particle track reconstructed due to various reactions in the detector volume. That is why in addition to the pronounced K^+ banana in Fig. 66 (left) we see some traces of pion and proton bands. At low K^+ -momenta, kaons can be well separated from pions and protons, but high-energy particles cannot be differentiated by dE/dX or by ToF information leading to particle misidentification. The higher W (the higher the ejectile energy), we have and the more kaons we lose due to misidentification; see Fig. 66 (right, green). In our analysis, we restricted ourselves to one and only one reconstructed charged-particle track. This condition helps to suppress the background, but does not reduce the reconstruction efficiency; see Fig. 66 (right, black).

Charged-particle track detection efficiency stays flat over the full range of W , but kaon reconstruction efficiency drops from about 60 % at low W to 20 % at $W \sim 3.5$ GeV. Since the GlueX acceptance is large and essentially hole-less, kaon reconstruction efficiency does not depend on yet

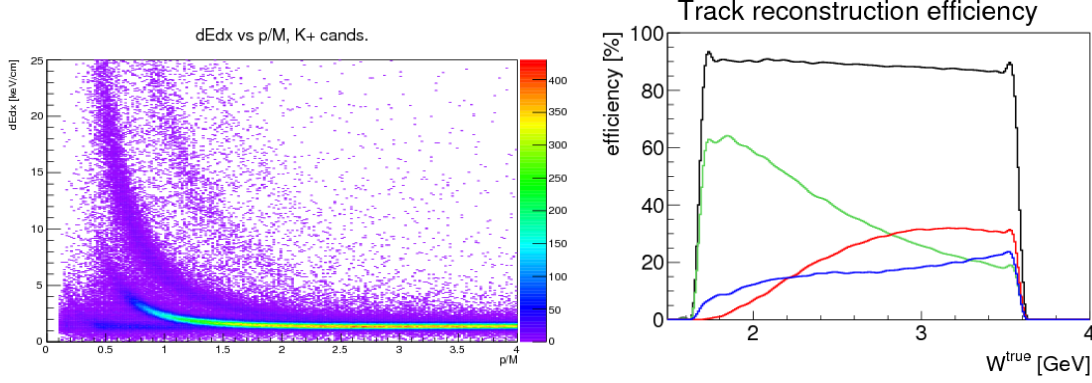


Figure 66: Left panel: dE/dx for the $K_L p \rightarrow K^+ n$ channel Right panel: Single charged-particle track detection efficiency as a function of W for the $K_L p \rightarrow K^+ n$ channel. Any charged particle (black), kaon (green), proton (red), and pion (blue).

unknown angular distributions. For the final selection of the $K_L p \rightarrow K^+ n$ reaction, we used a 3σ missing-mass cut around the neutron's mass; see Fig. 67.

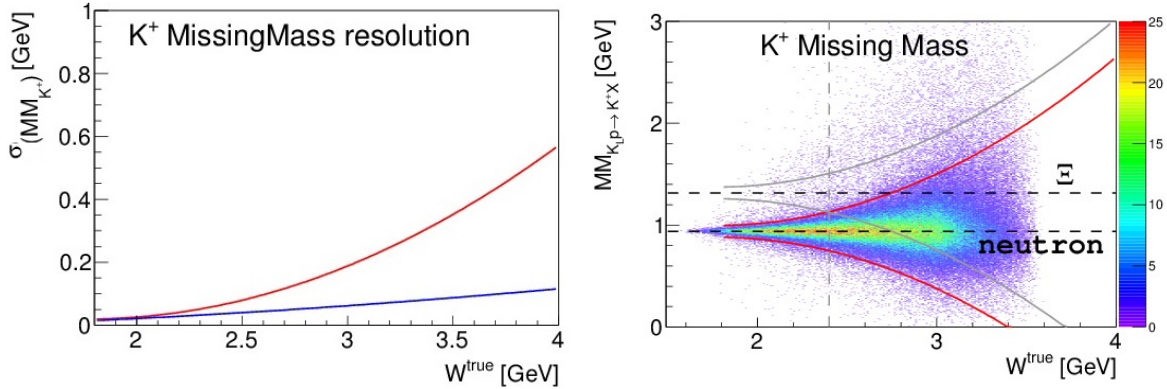


Figure 67: Left panel: Full (red) and detector related (blue) K^+ missing-mass resolution in terms of σ . In second case, the true K_L -momentum was used to calculate the missing mass. Right panel: K^+ missing-mass resolution as a function of W . 3σ missing-mass cuts for the $K_L p \rightarrow K^+ n$ (red) and $K_L p \rightarrow K^+ \Xi$ (gray) reactions are indicated by solid lines. Horizontal dashed lines show nominal masses of the neutron and Ξ baryon. The vertical gray dashed line indicates the range of pure missing-mass separation between these two reactions.

Figure 67 was plotted under the assumption of a 250 ps vertex time resolution. Both W (Fig. 65) and missing-mass resolutions are driven by the K_L -momentum resolution.

Below $W = 2.4$ GeV, the $K_L p \rightarrow K^+ n$ and $K_L p \rightarrow K^+ \Xi$ reactions can be disentangled by K^+ missing mass alone. Above this value, special treatment of the $K_L p \rightarrow K^+ \Xi$ background is required. One may notice that a 3σ cut for the $K_L p \rightarrow K^+ n$ reaction rises faster than for $K_L p \rightarrow K^+ \Xi^0$. This effect has a purely kinematical explanation - due to the higher mass of the Ξ^0 baryon, the K^+ produced in $K_L p \rightarrow K^+ \Xi$ reaction has a lower energy for the same value of W . The lower the K^+ energy we have, the better missing-mass resolution we get, and the more

narrow the missing-mass cut one needs to apply.

With the simulation performed we determine that in 100 days of a beamtime, around 60M $K_L p \rightarrow K^+ n$ events will be detected. A typical example of the expected statistics in comparison to previous data are shown in Fig. 68 (left). The highest flux is expected around $W = 3$ GeV, where we had to increase statistical uncertainties by a factor of 10 to make them visible (see Fig. 68 (right)).

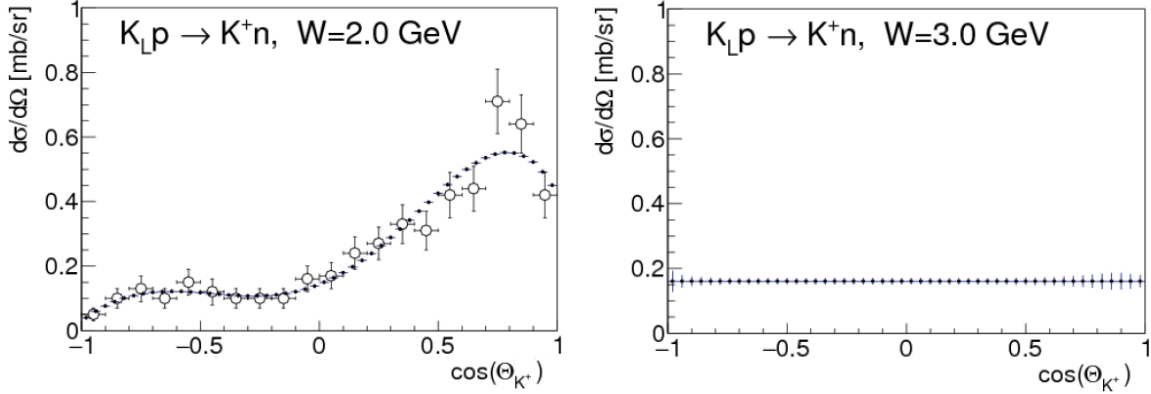


Figure 68: Left panel: Cross-section uncertainty estimates (statistical only) for $K_L p \rightarrow K^+ n$ reaction for the $W = 2$ GeV in comparison with data from Ref. [229]. Right panel: Same distribution for the $W = 3$ GeV. The error bars for the right plot were increased by factor of 10 to make them visible.

There are three major sources of background: $np \rightarrow K^+ nn$, $np \rightarrow \pi^+ nn$, and $K_L p \rightarrow K^+ \Xi^0$. Neutron flux drops exponentially with energy (see Fig. 6) for details) and generally the high-energy neutron flux is tiny.

$K_L p \rightarrow K^+ n$ background suppression: Due to its very high cross section, the $K_L p \rightarrow K^+ n$ reaction is essentially background free. Due to the extremely high statistics expected for this reaction our uncertainties will be dominated by systematics. We have identified three major sources of physical background: $np \rightarrow K^+ nn$, $np \rightarrow \pi^+ nn$, and $K_L p \rightarrow K^+ \Xi$ reactions.

Details on $K_L p \rightarrow K^+ n$ and $K_L p \rightarrow K^+ \Xi$ separation can be found in Appendix A5.6. For $W < 2.3$ GeV, these two reactions can be separated by a 3σ K^+ missing-mass cut. Above $W = 2.4$ GeV, one can use standard background suppression techniques - S-weights, Q-weights, NeuralNets, etc. . . . The main decay branch of Ξ is $\Xi^0 \rightarrow \pi^0 \Lambda \rightarrow \pi^0 \pi^- p$, which leads to several charged particles in the final state besides K^+ ; hence filtered out by a “one-charge-track-only” selection criterion. Another decay branch $\Xi^0 \rightarrow \pi^0 \Lambda \rightarrow \pi^0 \pi^0 n$ cannot be filtered out that easily; however, due to its smaller branching ratio combined with the small $K_L p \rightarrow K^+ \Xi$ production cross section, this channel only contributes at the level of 10^{-3} even without any background suppression techniques. Further suppression vetoing multiple neutral tracks and/or Q-weight should push this background far below 10^{-4} .

Neutron flux drops exponentially with energy and generally the high-energy neutron flux is small, but nonvanishing. If neutrons and K_L s have the same velocity, they cannot be separated by time

of flight. Neutron-induced reactions have high cross sections, which is why one needs to consider them as a possible source of background. In Fig. 69, one can see a comparison of kaon and neutron fluxes for the worse-case scenario when no neutron suppression is employed, similar to Fig. 17(right) in terms of β . Particles with the same β cannot be separated by time-of-flight. At $\beta = 0.95$ neutron and kaon fluxes become equal. This velocity corresponds to a neutron momentum of $p_n = 2.9 \text{ GeV}/c$ and kaon momentum of $p_K = 1.5 \text{ GeV}/c$.

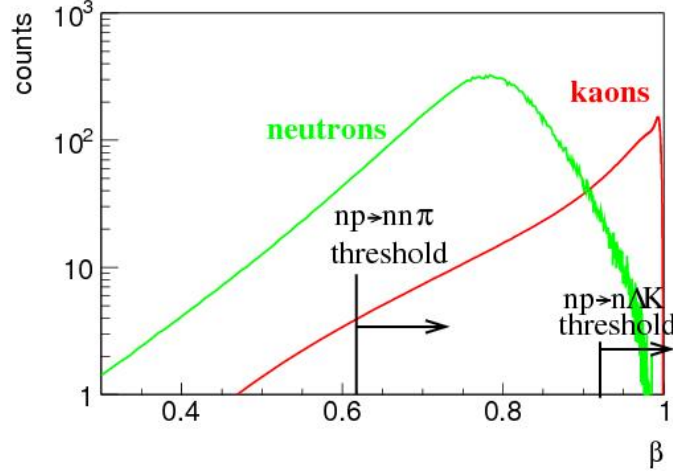


Figure 69: Neutron and K_L fluxes as a function of velocity β .

To evaluate the amount of background, we need to fold this flux with production cross section and reconstruction efficiency. Let's first consider the $np \rightarrow K^+ \Lambda n$ background. Unfortunately, this reaction is not very well measured, so we would use the $pp \rightarrow K^+ \Lambda p$ cross section parametrization together with the knowledge of $\frac{\sigma(pp \rightarrow K^+ \Lambda p)}{\sigma(np \rightarrow K^+ \Lambda n)} = 2$ from Ref. [230]. In Fig. 70, one can see the flux of K^+ s from kaon-induced $K_L p \rightarrow K^+ n$ reaction in comparison to a neutron-induced $np \rightarrow K^+ \Lambda n$ as a function of projectile velocities.

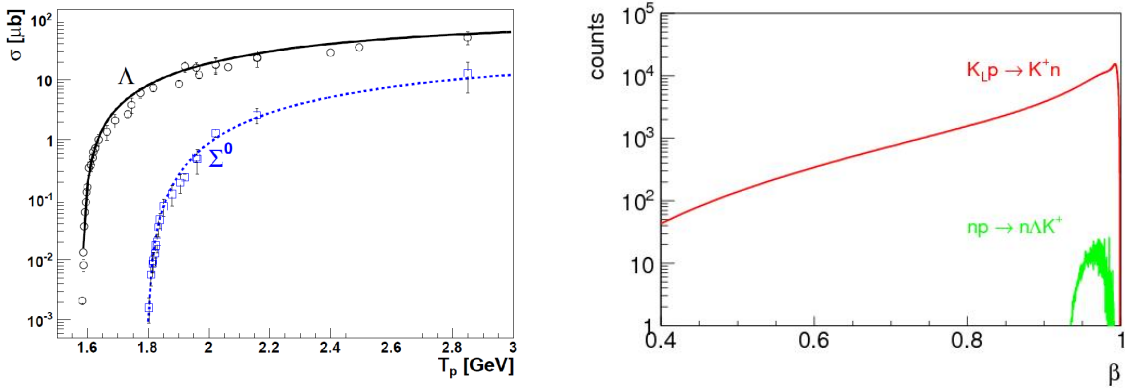


Figure 70: Left panel: $pp \rightarrow K^+ \Lambda p$ total cross section from Ref. [230]. Right panel: K^+ flux as a function of projectile velocity β for neutron-induced (green) and kaon-induced (red) reactions.

As one can see in Fig. 70, neutron-induced K^+ production contributes only in a very narrow range of energies. The contribution is also very small. One can further suppress this type of background by vetoing charged particles from Λ decay and performing a K^+ missing-mass cut. Altogether one can suppress this type of background below 10^{-4} .

The most dangerous type of neutron-induced background originates from the $np \rightarrow \pi^+ nn$ reaction with fast π^+ misidentification as K^+ . There are no measurements of $np \rightarrow \pi^+ nn$ reaction but due to isospin symmetry one can relate this reaction to an isospin symmetric case $np \rightarrow \pi^- pp$. The later reaction is known, see Ref. [231]. The total cross section for this reaction is about 2 mb. The $np \rightarrow \pi^+ nn$ reaction has a much lower threshold compared to $np \rightarrow K^+ \Lambda n$, so it can utilize an enormous flux of low-energy neutrons. However, low-energy neutrons predominately produce low-energy pions, which can be separated from kaons. The background needs to be considered only for $\beta > 0.8$; see Fig. 71. The background level looks much higher compared to Fig. 70, but it can be severely suppressed with the “ K^+ ” missing-mass cut since pion kinematics of the three-body $np \rightarrow \pi^+ nn$ reaction is very different from the $K_L p \rightarrow K^+ n$.

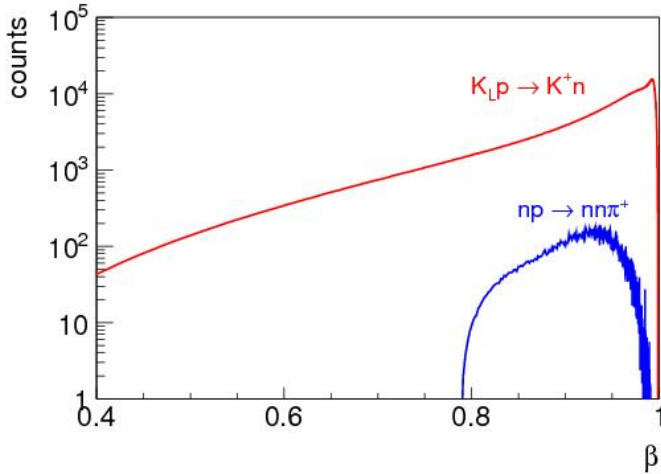


Figure 71: K^+ flux as a function of projectile velocity for the $np \rightarrow \pi^+ nn$ (green) and $K_L p \rightarrow K^+ n$ (red) reactions. Pion misidentification efficiency for the neutron-induced reaction is extracted from the full MC Geant simulation.

To summarize: Kaon particle identification together with a simple 3σ missing-mass cut and assumption of K_L beam can efficiently suppress all physical backgrounds of the $K_L p \rightarrow K^+ n$ reaction.

A6 $K\pi$ Study

A6.1 Simulation Study of $K_L p \rightarrow K^{*0} p \rightarrow K^+ \pi^- p$

To understand the behaviour of the P -wave $K\pi$ system at the proposed K_L facility we have performed a comprehensive simulation study, utilizing the Regge Model from Refs. [232, 233] by adapting it to the neutral kaon beam. The theoretical model showed a good agreement with existing charged kaon data produced with beam momenta between 2.1 and 10 GeV/ c and four momentum transfer up to 1 GeV². In our studies, we have assumed that the neutral exchange with charged kaon beam is similar to neutral kaon beam. The following reactions were simulated:

1. $K_L p \rightarrow K^{*0}(892)p \rightarrow K^+ \pi^- p$,
2. $K_L p \rightarrow \bar{K}^{*0}(892)p \rightarrow K^- \pi^+ p$,
3. $K_L p \rightarrow K^{*0}(892)p \rightarrow K_S \pi^0 p$,
4. $K_L p \rightarrow \bar{K}^{*0}(892)p \rightarrow K_S \pi^0 p$.

Fig. 72 (top left) shows the total cross section of $K^*(892)$ produced in reaction (a), and Figs. 72 (top right) and 72 (bottom) show the differential cross section $d\sigma/dt$ at $p_{K_L} = 5.5$ GeV/ c .

The two physical variables, beam momentum and four momentum transfer are essential for the study of the $K\pi$ production mechanism. Therefore we have performed a dedicated resolution and efficiency study to quantify the improvement that KLF facility can provide. The Fig. 73 (left) represents the relative resolution of the negative four momentum transfer $-t$ and the $K\pi$ invariant mass $m_{K^+\pi^-}$ (right). The relative resolution of $-t$ is very high, varying between 3 % and 5 % above 0.3 GeV² with slight increases close to the threshold. This behavior originates from the reconstruction of the slow recoil proton with momentum below 300 MeV/ c at GlueX. However, comparing to the experimental results and the binning resolution of t given in the studies [181, 234–237], a binning width of 0.02 GeV at low $-t$ is sufficient to increase the number of the data points and improve the precision for the study of the production mechanism. The $K\pi$ invariant mass resolution is very high - below 1.5 % over the full range of interest, see Fig. 73(right) for the details. This resolution is similar to the mass resolution of LASS Experiment [124].

An efficiency studies on the variables p_{K_L} , t and $m_{K\pi}$ were made to evaluate the improvement on the study of the $K\pi$ system with KLF. According to this simulation, the total integrated efficiency for the reaction $K_L p \rightarrow K^+ \pi^- p$ is found to be 14 %. Above $-t = 0.15$ GeV² the four momentum efficiency remains uniform around 16 %. The efficiency of $K^+ \pi^-$ invariant mass is uniform over the entire mass range [0.64, 1.2] GeV, see Fig. 74.

A6.2 $K^*(892)$ Production in KLF

Knowing the total acceptance with the cross section and expected luminosity, we can estimate the expected number of events for the $K^*(892)$ production in KLF. Almost 50 % of the neutral $K\pi$

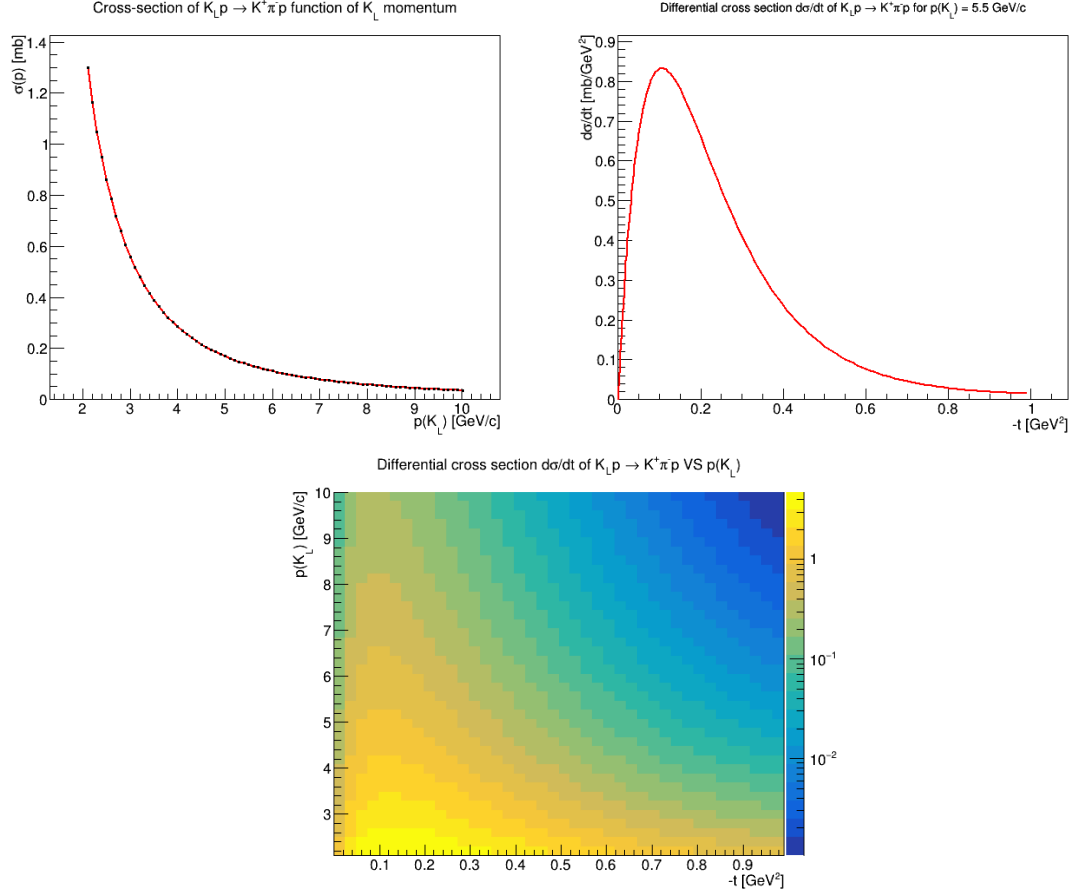


Figure 72: Top left panel: The total cross section in mb function of the beam momentum using Regge model in Ref. [232]. Top right panel: Differential cross section $d\sigma/dt$ for the process $K_L p \rightarrow K^{*0}(892)p \rightarrow K^+ \pi^- p$ at beam momentum $p = 5.5$ GeV/c using the production model in Ref. [232]. Bottom panel: Beam momentum versus the differential cross section for the process $K_L p \rightarrow K^{*0}(892)p \rightarrow K^+ \pi^- p$ using Regge model in Ref. [232].

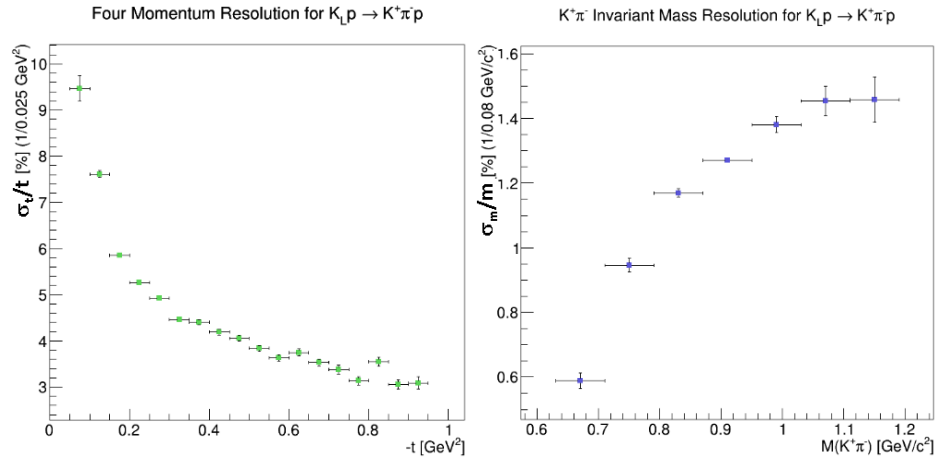


Figure 73: Left panel: Four momentum transfer relative resolution (σ_t/t) as a function of $-t$. Right panel: Invariant mass relative resolution (σ_m/m) as a function of $M(K\pi)$.

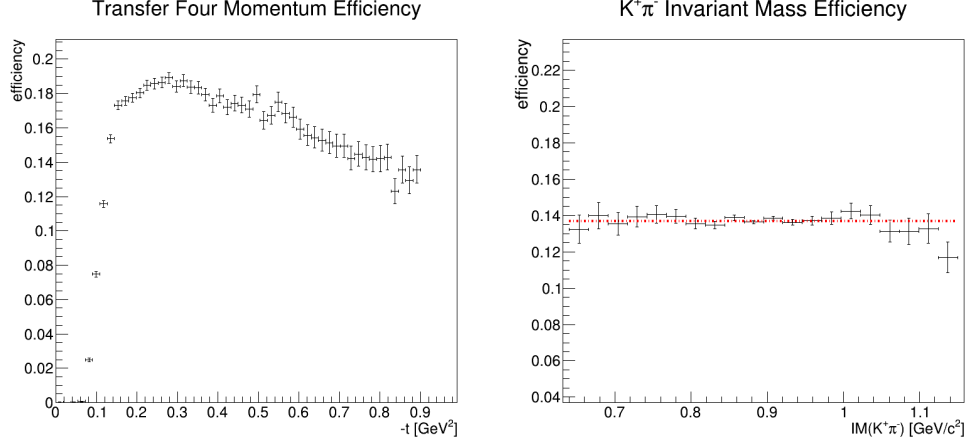


Figure 74: Reconstruction and selection efficiency of four momentum transfer (left plot) and $K^+\pi^-$ invariant mass (right plot).

P -wave are produced as $K_L p \rightarrow K^{*0}(892)p \rightarrow K^+\pi^-p$ and the rest as $K_L p \rightarrow \bar{K}^{*0}(892)p \rightarrow K^-\pi^+p$.

Fig. 75 (left) shows the expected number of $K^*(892)$ events produced in KLF during 100 days run with standard conditions (Tables 1 and 2), as a function of beam momentum p .

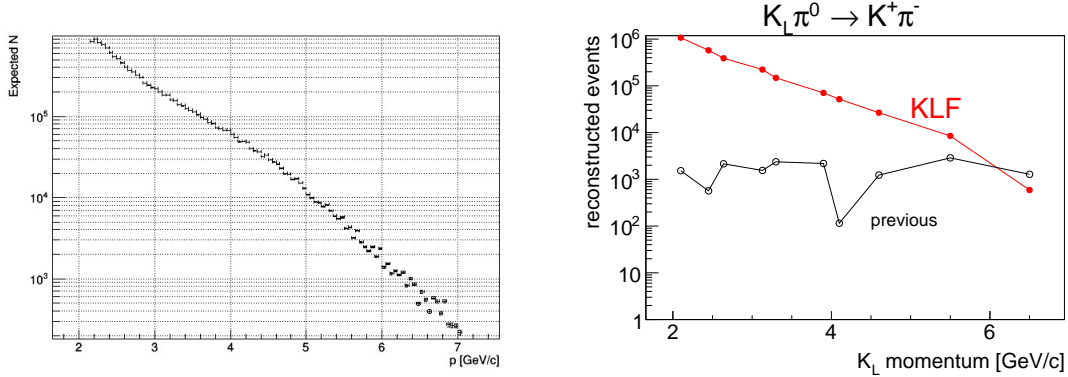


Figure 75: Left panel: Expected number of events of the reaction $K_L p \rightarrow K^{*0}(892)p$ function of beam momentum. Right panel: Events number of $K^*(892)$ production in former kaon beam experiment (only charged kaon) compared to the expected number of $K^*(892)$ produced by K_L facility with the same t - and W - cuts. Significant improvement of number of events expected in KLF specifically at low beam momenta. Previous data are from Refs. [181, 234, 235, 238–240] (Table 10).

The study of the strange mesons using kaon beam were performed in several experiments and mainly between the 1960s and 1980s. We expect three to four orders of magnitude improvement in $K^*(892)$ statistics in comparison to previously collected data [181, 234, 235, 237–239] (Fig. 75(right)).

Beam Momentum (GeV/c)	Experiment Reference	Number of events	Expected number of event by KLF during 100 days of run
2.1	[181]	1528	1071601
2.45	[181]	567	575225
2.64	[181]	2146	388781
3.13	[238]	1549	222877
3.30	[238]	2369	147978
3.9	[239]	2178	70640
4.1	[234]	115	51821
4.6	[239]	1233	26618
5.5	[234]	341	8479
5.5	[240]	2875	8479
6.5	[235]	1282	591

Table 10: Events Number of $K^*(892)$ production in former kaon beam experiment (only charged kaon) compared to the expected number of $K^*(892)$ produced by K_L facility (Fig. 75 (right)). Significant improvement of number of events expected in KLF specifically at low beam momenta.

A7 Current Hadronic Projects

Past measurements involving kaon scattering measurements were made at a variety of laboratories, mainly in the 1960s and 1980s when experimental techniques were far inferior to the standards of today (short summary is given in Appendix A2. It is important to recognize that current projects are largely complementary to the proposed Jlab KL hadron beam facility. We summarize the status of the FNAL, J-PARC, Belle, BaBar, \overline{P} ANDA, and COMPASS efforts here.

A7.1 Project X, USA

The status of Project X at FNAL [241–244] is as follows: First stage of Project X aims for neutrinos. Proposed K_L beam can be used to study rare decays and CP-violation [245]. It may be impossible to use the FNAL K_L beam for hyperon spectroscopy because of momentum range and n/K_L ratio (columns 4 and 6 at Table 11). In particular, the 31-yr old FNAL LoI addressed to the CP-violation study proposed to have a neutral kaon beam rate of $10^{10}/\text{hr}$ for high energies and very broad energy binning [246].

Project	Beam energy (GeV)	Target (λ_I)	$p(K_L)$ (MeV/c)	K_L/s (into 0.5 msr)	K_L/n ($E_n > 10$ MeV)
BNL AGS	24	1.1 Pt	300–1200	60×10^6	$\sim 1:1000$
Project X	3	1.0 C	300–1200	450×10^6	$\sim 1:2700$

Table 11: Comparison of the K_L production yield. The BNL AGS kaon and neutron yields are taken from RSVP reviews in 2004 and 2005. The Project X yields are for a thick target, fully simulated with LAQGSM/MARS15 into the KOPIO beam solid angle and momentum acceptance from Ref. [242].

A7.2 J-PARC, Japan

While J-PARC has a whole program of charged strange particle and hypernuclear reactions, the photon beam at KLF allows unique access to other channels. J-PARC provides separated secondary beam lines up to 2 GeV/c (Table 12). The operation of the Hadron Experimental Facility resumed in April of 2015 following a two-year suspension to renovate the facility after the accident that occurred in May 2013 [247]. The primary beam intensity is currently 50 kW, and can be upgraded to 85 kW. This will correspond to $\sim 10^9$ ppp (particles per pulse) for pion beam intensity and to $\sim 10^6$ ppp for negative kaon beam flux. The K/π ratio is expected to be close to 10, which is realized with double-stage electrostatic separators. One of the main problems in the K/π separation is a high duty-factor of the J-PARC Complex.

With K^- beams, currently there is no proposal specific for $S = -1$ hyperons, but the cascades will be studied in the early stage of E50 [249], hopefully in a few years. The beam momentum bite, $\Delta p/p$, is strongly depending on the configuration of the beam line spectrometer, but one can

Beamline	Particle	Momentum (GeV/c)	Number of particles per spill	Characteristics
K1.8	K^\pm, π^\pm	<2.0	$10^6 K^-$	separated
K1.8BR	K^\pm, π^\pm	<1.1	$10^5 K^-$	separated
KL	K_L	2.1 in ave.	$10^7 K_L$	to 16°
High-p	p π^\pm	<31	10^{10} p $10^7 \pi$	primary protons
K1.1	K^\pm, π^\pm	<1.2 0.7~0.8	$10^6 K^-$	separated lower momentum [K1.1BR]
HIHR	π^\pm	<2.0	$2.8 \times 10^8 \pi^-$	separated $\times 10$ better $\Delta p/p$
K10	K^\pm, π^\pm, \bar{p}	<10	$10^7 K^-$	separated
new KL	K_L	5.2 in ave.	$10^8 K_L$	to 5° n/ K_L optimized

Table 12: J-PARC beamlines in the Hadron Experimental Facility from Ref. [248]. Top part of Table gives information about beamlines in the present hall, while bottom part information is about new beamlines in the extended area.

determine beam momentum with the resolution of $\Delta p/p \sim 10^{-3}$ or 10^{-4} . One can think that the systematic study for $S = -1$ hyperons even with charged kaons is desirable and J-PARC folks think that such a study is definitely needed but currently there is no room to accept a new proposal to require a long beamline. J-PARC is focusing on hypernuclei physics [250].

There is no K_L beamline for hyperon physics at J-PARC. It is 100 % dedicated to the study of CP-violation. The momentum is spread out from 1 to 4 GeV/c, there is no concept of $\Delta p/p$ since the beam cannot be focused with EM devices.

A7.3 Belle, Japan

The Belle Collaboration at KEK has plenty of e^+e^- data, and people in Belle [Belle Nuclear Physics Consortium (Belle NPC)] are now extracting various charm-baryon decay processes, which can be used for cascade resonance spectroscopy, from those “raw” e^+e^- data [251, 252].

A7.4 BaBar, USA

The BaBar Collaboration at SLAC studied, for instance, properties of the $\Xi(1530)^0$ in the decay of $\Lambda_C^+ \rightarrow (\pi^+\Xi^-)K^+$ and $\Xi(1690)^0$ in the decay of $\Lambda_C^+ \rightarrow (\bar{K}^0\Lambda)K^+$ [253–255] (see, for instance, a recent overview by Ziegler [256]).

A7.5 \overline{P} ANDA, Germany

The \overline{P} ANDA experiment [257] will measure annihilation reactions of antiprotons with nucleons and nuclei in order to provide complementary and in part uniquely decisive information on a wide range of QCD aspects. The scientific scope of \overline{P} ANDA is ordered into several pillars: hadron spectroscopy, properties of hadrons in matter, nucleon structure and hypernuclei. Antiprotons are produced with a primary proton beam, collected and phase-space cooled in the CR (Collector Ring), and then transferred to the HESR (High Energy Storage Ring) where they are stacked, further phase-space cooled, and then directed onto an internal target located at the center of the \overline{P} ANDA detector. The facility will start with a luminosity of 10^{31} cm²/s and a momentum resolution of $\Delta p/p = 10^{-4}$, and later improve to 2×10^{32} and 4×10^{-5} , respectively. The large cross section into baryon-antibaryon final states (e.g., ~ 1 μ b for $\Xi\overline{\Xi}$ or 0.1 μ b for $\Omega\overline{\Omega}$) make spectroscopic studies of excited multi-strange hyperons a very compelling part of the initial program of \overline{P} ANDA, which is expected to commence by 2025 [258].

A7.6 COMPASS, CERN

COMPASS is thinking of the physics using an RF-separated beam of charged kaons. It is still in the discussion stage. The rates, which were presented as a very first guess by the CERN beamline group were very interesting for a strangeness physics program via diffractive production of strange resonances [259]. The cost of a RF-separated beam is high; however, something like this had been built in the past.

Charged kaons could be used to extend the χ PT investigations into the strangeness sector, e.g., to measure the polarizability of the kaon and for a spectroscopy program. At present, COMPASS filters out kaons in the COMPASS charged hadron beam via Cherenkov detectors but they make up only about 2.6 % of all beam particles. With an RF-separated kaon beam, they would aim for a more than 20x larger dataset compared to what has been measured so far. This would allow them to perform an analysis, similar to their analysis of pion-beam diffraction: $\pi^- p \rightarrow \pi^- \pi^- \pi^+ + p_{\text{recoil}}$ [260]. The energy of the kaon beam would probably be below 100 GeV but above 40 – 50 GeV. The latter number is defined by the stability of the power supplies for the beamline, which after all is about 1 km long.

At these high energies, diffractive production via Pomeron exchange is the dominant process and beam excitations can be well separated from target excitations. This would allow them to collect a clean data sample of kaon-beam diffraction.

A8 Additional Physics Potential with a K_L Beam

As stated in the summary of Mini-Proceedings of the Workshop on Excited Hyperons in QCD Thermodynamics at Freeze-Out (YSTAR2016) [261]: a very interesting further opportunity for the KL Facility is to investigate KL reactions on complex nuclei. By selecting events with the appropriate beam momentum together with a fast forward-going pion, events can be identified, in which a hyperon is produced at low relative momentum to the target nucleus or even into a bound state. Baryons with strangeness embedded in the nuclear environment, hypernuclei or hyperatoms, are the only available tool to approach the many-body aspect of the three-flavor strong interaction. Furthermore, appropriate events with a forward-going K^+ could deposit a double-strange hyperon into the remaining nucleus, potentially enabling searches for and studies of double- Λ hypernuclei.

Similarly, the scattering of kaons from nuclear targets could be a favorable method to measure the matter form factor (and, therefore, neutron skin) of heavy nuclei, with different and potentially smaller systematics than other probes. The character of the neutron skin, therefore, has a wide impact and the potential to give important new information on neutron star structure and cooling mechanisms [262–266], searches for physics beyond the standard model [267, 268], the nature of 3-body forces in nuclei [269, 270], collective nuclear excitations [271–274] and flows in heavy-ion collisions [275, 276]. Theoretical developments and investigations will be required to underpin such a program, but the science impact of such measurements is high.

Further potential exists to search for – or exclude – possible exotic baryonic states that cannot easily be described by the usual three-valence-quark structure. Recent results from LHCb provide tantalizing hints for the existence of so-called pentaquarks that include a charm valence quark; however, the interpretation of those results is under discussion. In contrast, elastic scattering of K_L with a hydrogen target gives unambiguous information on the potential existence of such states in the strange sector. With the given flux of K_L at the proposed facility, a clear proof of existence or proof of absence will be obtained within the integrated luminosity required for the excited hyperon spectroscopy program that forms the basis of this proposal.

There are two particles in the reaction $K_L p \rightarrow \pi Y$ and KY that can carry polarization: the target and recoil baryons. Hence, there are two possible double-polarization experiments: target/recoil. The total number of observables is three. The formalism and definitions of observables commonly used to describe the reaction $K_L p \rightarrow KY$ is given in Sec. 4. Although one cannot easily measure recoil polarization with GlueX, the self-analyzing decay of hyperons makes this possible. Double-polarization experiments, using, e.g., a polarized target like FROST [162], will however be left for future proposal(s).

The physics potential connected with studies of CP-violating decays of the K_L is very appealing; however, that topic is not currently the focus of this proposal, since a detailed comparison with the competition from existing and upcoming experiments is needed in order to identify the most attractive measurements that could be done at the proposed KL Facility at JLab.

References

- [1] A. Ali *et al.* [GlueX Collaboration], *Future Physics in Hall D with the GlueX Detector*: https://halldweb.jlab.org/DocDB/0038/003870/011/gluex_future.pdf
- [2] A. Aprahamian *et al.*, *Reaching for the Horizon: The 2015 Long Range Plan for Nuclear Science*: <http://science.energy.gov/np/nsac/>.
- [3] M. Tanabashi *et al.* [Particle Data Group], Phys. Rev. D **98**, no. 3, 030001 (2018).
- [4] B. M. K. Nefkens, πN Newslett. **14**, 150 (1998).
- [5] R. Koniuk and N. Isgur, Phys. Rev. Lett. **44**, 845 (1980).
- [6] H. Al Ghouli *et al.* [GlueX Collaboration], Phys. Rev. C **95**, no. 4, 042201 (2017).
- [7] A. AlekSejevs *et al.* [GlueX Collaboration], arXiv:1305.1523 [nucl-ex].
- [8] Y. Qiang, Y. I. Azimov, I. I. Strakovsky, W. J. Briscoe, H. Gao, D. W. Higinbotham, and V. V. Nelyubin, Phys. Lett. B **694**, 123 (2011).
- [9] W. J. Briscoe, M. Döring, H. Haberzettl, D. M. Manley, M. Naruki, I. I. Strakovsky, and E. S. Swanson, Eur. Phys. J. A **51**, no. 10, 129 (2015).
- [10] Web page of the Workshop on *Physics with Neutral Kaon Beam at JLab* (KL2016), JLab, Newport News, VA, USA, Feb. 2016: <https://www.jlab.org/conferences/kl2016/> contains presentations.
- [11] Web page of the Workshop on *Excited Hyperons in QCD Thermodynamics at Freeze-Out* (YSTAR2016), JLab, Newport News, VA, USA, Nov. 2016: <https://www.jlab.org/conferences/YSTAR2016/> contains presentations.
- [12] Web page of the Workshop on *New Opportunities with High-Intensity Photon Sources* (HISP2017), CUA, Washington, DC, USA, Feb. 2017: <https://www.jlab.org/conferences/HIPS2017/> contains presentations.
- [13] Web page of the Workshop on *Pion-Kaon Interactions* (PKI2018), JLab, Newport News, VA, USA, Feb. 2018: <https://www.jlab.org/conferences/pki2018/> contains presentations.
- [14] M. Amarian, U.-G. Meißner, C. Meyer, J. Ritman, and I. Strakovsky, eds., Mini-Proceedings, *Workshop on Physics with Neutral Kaon Beam at JLab* (KL2016); arXiv:1604.02141 [hep-ph].
- [15] *Physics opportunities with secondary K_L beam at JLab*, Spokesperson: M. Amarian [GlueX Collaborations], JLab LoI12–15–001, Newport News, VA, USA, 2015.
- [16] *Strange hadron spectroscopy with a secondary KL beam at GlueX*, Spokespersons: M. J. Amarian, M. Bashkanov, J. Ritman, J. R. Stevens, and I. I. Strakovsky [GlueX Collaboration], JLab Proposal PR12–17–001, Newport News, VA, USA, 2017; arXiv:1707.05284 [hep-ex].

- [17] *Photoproduction of the very strangest baryons on the proton target in CLAS12*, Spokespersons: L. Guo, M. Dugger, J. Goetz, E. Pasyuk, I.I. Strakovsky, D.P. Watts, N. Zachariou, and V. Ziegler [Very Strange Collaboration for CLAS Collaboration], JLab Proposal E12–11–005A, Newport News, VA, USA, 2013.
- [18] *Nucleon resonance structure studies via exclusive KY electroproduction at 6.6 GeV and 8.8 GeV*, Spokespersons: D.S. Carman, R. Gothe, and V. Mokeev [CLAS Collaboration], JLab E12–16–010A, Newport News, VA, USA, 2016.
- [19] M. Amaryan, E. Chudakov, K. Rajagopal, C. Ratti, J. Ritman, and I. Strakovsky, eds., Mini-Proceedings, *Workshop on Excited Hyperons in QCD Thermodynamics at Freeze-Out* (YSTAR2016); arXiv:1701.07346 [hep-ph].
- [20] T. Horn, C. Keppel, C. Munoz-Camacho, and I. Strakovsky, eds., Mini-Proceedings, *Workshop on High-Intensity Photon Sources* (HIPS2017); arXiv:1704.00816 [nucl-ex].
- [21] M. Amaryan, C. Meyer, U.-G. Meißner, J. Ritman, and I. Strakovsky, eds., Mini-Proceedings, *Workshop on Pion-Kaon Interactions* (PKI2018); arXiv:1804.06528 [hep-ph].
- [22] C. Amsler, S. Eidelman, T. Gutsche, C. Hanhart, S. Spanier, and N. A. Törnqvist, in: Ref. [23].
- [23] C. Patrignani *et al.* [Particle Data Group], Chin. Phys. C **40**, no. 10, 100001 (2016).
- [24] S. Descotes-Genon and B. Moussallam, Eur. Phys. J. C **48**, 553 (2006).
- [25] N. Isgur and M. B. Wise, Phys. Rev. Lett. **66**, 1130 (1991).
- [26] R. Aaij *et al.* [LHCb Collaboration], Phys. Rev. Lett. **119**, no. 11, 112001 (2017).
- [27] R. Aaij *et al.* [LHCb Collaboration], Phys. Rev. Lett. **121**, no. 16, 162002 (2018).
- [28] R. Aaij *et al.* [LHCb Collaboration], Phys. Rev. Lett. **121**, no. 7, 072002 (2018).
- [29] R. Aaij *et al.* [LHCb Collaboration], Phys. Rev. Lett. **118**, no. 18, 182001 (2017).
- [30] R. G. Edwards *et al.* [Hadron Spectrum Collaboration], Phys. Rev. D **87**, no. 5, 054506 (2013).
- [31] M. Luscher, Nucl. Phys. B **354**, 531 (1991).
- [32] K. Rummukainen and S. A. Gottlieb, Nucl. Phys. B **450**, 397 (1995).
- [33] S. Aoki *et al.* [CP-PACS Collaboration], Phys. Rev. D **76**, 094506 (2007).
- [34] X. Feng, K. Jansen, and D. B. Renner, Phys. Rev. D **83**, 094505 (2011).
- [35] J. J. Dudek *et al.* [Hadron Spectrum Collaboration], Phys. Rev. D **87**, no. 3, 034505 (2013); Erratum: [Phys. Rev. D **90**, no. 9, 099902 (2014)].
- [36] D. Guo, A. Alexandru, R. Molina, and M. Döring, Phys. Rev. D **94**, no. 3, 034501 (2016).

- [37] C. Alexandrou *et al.*, Phys. Rev. D **96**, no. 3, 034525 (2017).
- [38] J. Bulava, B. Fahy, B. Hz, K. J. Juge, C. Morningstar, and C. H. Wong, Nucl. Phys. B **910**, 842 (2016).
- [39] C. B. Lang, D. Mohler, S. Prelovsek, and M. Vidmar, Phys. Rev. D **84**, no. 5, 054503 (2011); Erratum: [Phys. Rev. D **89**, no. 5, 059903 (2014)].
- [40] R. Brett, J. Bulava, J. Fallica, A. Hanlon, B. Hz, and C. Morningstar, arXiv:1802.03100 [hep-lat].
- [41] P. Guo, J. Dudek, R. Edwards, and A. P. Szczepaniak, Phys. Rev. D **88**, no. 1, 014501 (2013).
- [42] R. A. Briceno and Z. Davoudi, Phys. Rev. D **88**, no. 9, 094507 (2013).
- [43] U.-G. Meißner, G. Rios, and A. Rusetsky, Phys. Rev. Lett. **114**, no. 9, 091602 (2015); Erratum: [Phys. Rev. Lett. **117**, no. 6, 069902 (2016)].
- [44] C. Liu, X. Feng, and S. He, Int. J. Mod. Phys. A **21**, 847 (2006).
- [45] M. Lage, U.-G. Meißner, and A. Rusetsky, Phys. Lett. B **681**, 439 (2009).
- [46] C. Morningstar, J. Bulava, B. Singha, R. Brett, J. Fallica, A. Hanlon, and B. Hz, Nucl. Phys. B **924**, 477 (2017).
- [47] M. Döring, U. G. Meißner, E. Oset, and A. Rusetsky, Eur. Phys. J. A **47**, 139 (2011).
- [48] M. Döring and U. G. Meißner, JHEP **1201**, 009 (2012).
- [49] M. Döring, U. G. Meißner, E. Oset, and A. Rusetsky, Eur. Phys. J. A **48**, 114 (2012).
- [50] D. J. Wilson, R. A. Briceno, J. J. Dudek, R. G. Edwards, and C. E. Thomas, Phys. Rev. D **92**, no. 9, 094502 (2015).
- [51] D. J. Wilson, J. J. Dudek, R. G. Edwards, and C. E. Thomas, Phys. Rev. D **91**, no. 5, 054008 (2015).
- [52] J. J. Dudek *et al.* [Hadron Spectrum Collaboration], Phys. Rev. Lett. **113**, no. 18, 182001 (2014).
- [53] R. A. Briceno, J. J. Dudek, R. G. Edwards, and D. J. Wilson, Phys. Rev. D **97**, no. 5, 054513 (2018).
- [54] R. A. Briceno, J. J. Dudek, R. G. Edwards, and D. J. Wilson, Phys. Rev. Lett. **118**, no. 2, 022002 (2017).
- [55] R. G. Edwards, J. J. Dudek, D. G. Richards, and S. J. Wallace, Phys. Rev. D **84**, 074508 (2011).
- [56] G. P. Engel *et al.* [BGR Collaboration], Phys. Rev. D **87**, no. 7, 074504 (2013).

- [57] J. J. Dudek and R. G. Edwards, Phys. Rev. D **85**, 054016 (2012).
- [58] C. W. Andersen, J. Bulava, B. Hz, and C. Morningstar, Phys. Rev. D **97**, no. 1, 014506 (2018).
- [59] R. Brower, N. Christ, C. DeTar, R. Edwards, and P. Mackenzie, EPJ Web Conf. **175**, 09010 (2018).
- [60] G. Höhler and H. Schopper, Numerical Data And Functional Relationships In Science And Technology. Group I: Nuclear And Particle Physics. Vol. 9: Elastic And Charge Exchange Scattering Of Elementary Particles. B: Pion Nucleon Scattering. Pt. 2: Methods And Results Of Phenomenological Analyses (Landolt-Börnstein. New Series, I/9B2) (Springer, Berlin, Germany, 1983) 601 P.
- [61] R. A. Arndt, W. J. Briscoe, I. I. Strakovsky, and R. L. Workman, Phys. Rev. C **74**, 045205 (2006).
- [62] Z. W. Liu, J. M. M. Hall, D. B. Leinweber, A. W. Thomas, and J. J. Wu, Phys. Rev. D **95**, no. 1, 014506 (2017).
- [63] J. A. Oller and U.-G. Meißner, Phys. Lett. B **500**, 263 (2001).
- [64] A. Cieplý, M. Mai, U.-G. Meißner, and J. Smejkal, Nucl. Phys. A **954**, 17 (2016).
- [65] K. Moriya *et al.* [CLAS Collaboration], Phys. Rev. C **87**, no. 3, 035206 (2013).
- [66] M. Mai and U.-G. Meißner, Eur. Phys. J. A **51**, no. 3, 30 (2015).
- [67] W. Kamleh, J. M. M. Hall, D. B. Leinweber, B. J. Menadue, B. J. Owen, A. W. Thomas, and R. D. Young, PoS CD **15**, 037 (2016).
- [68] R. Molina and M. Döring, Phys. Rev. D **94**, no. 5, 056010 (2016); Addendum: [Phys. Rev. D **94**, no. 7, 079901 (2016)].
- [69] N. N. Scoccola, H. Nadeau, M. A. Nowak, and M. Rho, Phys. Lett. B **201**, 425 (1988); Erratum: [Phys. Lett. B **220**, 658 (1989)].
- [70] C. G. Callan, Jr., K. Hornbostel, and I. R. Klebanov, Phys. Lett. B **202**, 269 (1988).
- [71] K. F. Liu, Int. J. Mod. Phys. E **26**, no. 01n02, 1740016 (2017).
- [72] L. Y. Glozman and D. O. Riska, Phys. Rept. **268**, 263 (1996).
- [73] K. F. Liu, Y. Chen, M. Gong, R. Sufian, M. Sun, and A. Li, PoS LATTICE **2013**, 507 (2014).
- [74] H. Zhang, J. Tulpan, M. Shrestha, and D. M. Manley, Phys. Rev. C **88**, no. 3, 035204 (2013).
- [75] H. Zhang, J. Tulpan, M. Shrestha, and D. M. Manley, Phys. Rev. C **88**, no. 3, 035205 (2013).
- [76] W. J. Briscoe, M. Döring, H. Haberzettl, I. I. Strakovsky, and R. L. Workman, Institute of Nuclear Studies of The George Washington University Database; <http://gwdac.phys.gwu.edu>.

- [77] D. M. Manley, in: *Workshop on Physics with Neutral Kaon Beam at JLab: mini-Proceedings*, arXiv:1604.02141 [hep-ph] (February, 2016), p. 42.
- [78] H. Kamano, S. X. Nakamura, T.-S. H. Lee, and T. Sato, Phys. Rev. C **90**, no. 6, 065204 (2014).
- [79] H. Kamano, S. X. Nakamura, T.-S. H. Lee, and T. Sato, Phys. Rev. C **92**, no. 2, 025205 (2015); Erratum: [Phys. Rev. C **95**, no. 4, 049903 (2017)].
- [80] B. C. Jackson, Y. Oh, H. Haberzettl, and K. Nakayama, Phys. Rev. C **91**, no. 6, 065208 (2015).
- [81] J. K. Hassall *et al.*, Nucl. Phys. B **189**, 397 (1981).
- [82] M. Mai and U.-G. Meißner, Nucl. Phys. A **900**, 51 (2013).
- [83] P. C. Bruns, M. Mai, and U.-G. Meißner, Phys. Lett. B **697**, 254 (2011).
- [84] Y. Ikeda, T. Hyodo, and W. Weise, Nucl. Phys. A **881**, 98 (2012).
- [85] Z. H. Guo and J. A. Oller, Phys. Rev. C **87**, no. 3, 035202 (2013).
- [86] A. Cieplý and J. Smejkal, Nucl. Phys. A **881**, 115 (2012).
- [87] S. Godfrey and J. Napolitano, Rev. Mod. Phys. **71**, 1411 (1999).
- [88] S. Narison, Nucl. Phys. Proc. Suppl. **96**, 244 (2001).
- [89] R. J. Crewther and L. C. Tunstall, Phys. Rev. D **91**, no. 3, 034016 (2015).
- [90] V. Bernard, N. Kaiser, and U. G. Meißner, Nucl. Phys. B **357**, 129 (1991).
- [91] V. Bernard, N. Kaiser, and U. G. Meißner, Nucl. Phys. B **364**, 283 (1991).
- [92] V. Bernard, N. Kaiser, and U. G. Meißner, Phys. Rev. D **43**, 2757 (1991).
- [93] J. Bijnens, P. Dhonte, and P. Talavera, JHEP **0405**, 036 (2004).
- [94] Z. H. Guo and J. A. Oller, Phys. Rev. D **84**, 034005 (2011).
- [95] A. Dobado and J. R. Pelaez, Phys. Rev. D **47**, 4883 (1993).
- [96] A. Gomez Nicola and J. R. Pelaez, Phys. Rev. D **65**, 054009 (2002).
- [97] M. Jamin, J. A. Oller, and A. Pich, Nucl. Phys. B **587**, 331 (2000).
- [98] J. Nebreda and J. R. Pelaez., Phys. Rev. D **81**, 054035 (2010).
- [99] J. R. Pelaez, Phys. Rept. **658**, 1 (2016).
- [100] R. L. Jaffe, Phys. Rev. D **15**, 267 (1977).
- [101] T. Barnes, Phys. Lett. **165B**, 434 (1985).

- [102] E. van Beveren, T. A. Rijken, K. Metzger, C. Dullemond, G. Rupp, and J. E. Ribeiro, Z. Phys. C **30**, 615 (1986).
- [103] J. A. Oller, E. Oset, and J. R. Pelaez, Phys. Rev. Lett. **80**, 3452 (1998); Phys. Rev. D **59**, 074001 (1999); Erratum: [Phys. Rev. D **60**, 099906 (1999)]; Erratum: [Phys. Rev. D **75**, 099903 (2007)].
- [104] D. Black, A. H. Fariborz, F. Sannino, and J. Schechter, Phys. Rev. D **58**, 054012 (1998); Phys. Rev. D **59**, 074026 (1999).
- [105] J. A. Oller and E. Oset, Phys. Rev. D **60**, 074023 (1999).
- [106] F. E. Close and N. A. Tornqvist, J. Phys. G **28**, R249 (2002).
- [107] J. R. Pelaez, Phys. Rev. Lett. **92**, 102001 (2004).
- [108] J. R. Pelaez, Mod. Phys. Lett. A **19**, 2879 (2004).
- [109] R. Jaffe and F. Wilczek, Eur. Phys. J. C **33**, S38 (2004).
- [110] P. Büttiker, S. Descotes-Genon, and B. Moussallam, Eur. Phys. J. C **33**, 409 (2004).
- [111] J. R. Pelaez and A. Rodas, Phys. Rev. D **93**, no. 7, 074025 (2016).
- [112] S. R. Beane et al., Phys. Rev. D **74**, 114503 (2006).
- [113] J. M. Flynn and J. Nieves, Phys. Rev. D **75**, 074024 (2007).
- [114] Z. Fu, Phys. Rev. D **85**, 074501 (2012).
- [115] K. Sasaki *et al.* [PACS-CS Collaboration], Phys. Rev. D **89**, no. 5, 054502 (2014).
- [116] J. R. Batley *et al.* [NA48-2 Collaboration], Eur. Phys. J. C **70**, 635-657 (2010).
- [117] P. Masjuan, J. Ruiz de Elvira, and J. J. Sanz-Cillero, Phys. Rev. D **90**, no. 9, 097901 (2014).
- [118] J. R. Pelaez, A. Rodas, and J. Ruiz de Elvira, Eur. Phys. J. C **77**, no. 2, 91 (2017).
- [119] S. M. Roy, Phys. Lett. **36B**, 353 (1971).
- [120] F. Steiner, Fortsch. Phys. **19**, 115 (1971).
- [121] D. Aston *et al.*, Nucl. Phys. B **292**, 693 (1987).
- [122] D. Aston *et al.*, Nucl. Phys. B **296**, 493 (1988).
- [123] B. R. Martin, D. Morgan, and G. Shaw, Pion Pion Interactions in Particle Physics (Academic press, London, 1976).
- [124] P. Estabrooks, R. K. Carnegie, A. D. Martin, W. M. Dunwoodie, T. A. Lasinski, and D. W. G. S. Leith, Nucl. Phys. B **133**, 490 (1978).

- [125] C. B. Lang, Fortsch. Phys. **26**, 509 (1978).
- [126] P. del Amo Sanchez *et al.* [BaBar Collaboration], Phys. Rev. D **83**, 072001 (2011).
- [127] D. Epifanov *et al.* [Belle Collaboration], Phys. Lett. B **654**, 65 (2007).
- [128] D. R. Boito, R. Escribano, and M. Jamin, JHEP **1009**, 031 (2010).
- [129] M. Antonelli *et al.* [FlaviaNet Working Group on Kaon Decays], Eur. Phys. J. C **69**, 399 (2010).
- [130] F. Niecknig and B. Kubis, JHEP **1510**, 142 (2015).
- [131] B. Adeva *et al.* [DIRAC Collaboration], Phys. Rev. D **96**, 052002 (2017).
- [132] C. B. Lang, L. Leskovec, D. Mohler, and S. Prelovsek, Phys. Rev. D **86**, 054508 (2012).
- [133] S. Prelovsek, L. Leskovec, C. B. Lang, and D. Mohler, Phys. Rev. D **88**, no. 5, 054508 (2013).
- [134] R. Yamartino *et al.*, Phys. Rev. D **10**, 9 (1974); Ph. D Thesis, SLAC Stanford University, 1974; SLAC-R-0177, SLAC-R-177, SLAC-0177, SLAC-177.
- [135] S. Abrahamyan and B. Wojtsekhowski, *WACS Experiment with NPS and SBS*, https://wiki.jlab.org/cuawiki/images/3/32/Sergey_Abrahamyan_WACS_NPS_2014_update.pdf
P. Degtyarenko and B. Wojtsekhowski, "Compact Photon Source Conceptual Design;"
B. Wojtsekhowski and G. Niculescu, arXiv:1712.06419 [physics.acc-ph];
V. Bellini, F. Tortorici, E. Cisbani, F. Mammoliti, G. Nicolescu, C. M. Suter, G. M. Urciuoli,
and B. Wojtsekhowski, PoS INPC **2016**, 311 (2017);
The NPS web page: https://wiki.jlab.org/cuawiki/index.php/High_Intensity_Photon_Source
- [136] A. D. Brody *et al.*, Phys. Rev. Lett. **22**, 966 (1969).
- [137] M. G. Albrow *et al.*, Nucl. Phys. B **23**, 509 (1970).
- [138] I. I. Strakovsky, M. J. Amarian, W. J. Briscoe, P. Degtyarenko, A. Somov, J. R. Stevens, and T. Whitlatch, Preprint GlueX-doc-3601, 2018.
- [139] GlueX wiki: <https://halldweb.jlab.org/wiki/images/d/df/CollimatorElevationSept08.png> ;
S. Worthington, private communication, 2018.
- [140] F. Barbosa, C. Hutton, A. Sitnikov, A. Somov, S. Somov, and I. Tolstukhin, Nucl. Instrum. Meth. A **795**, 376 (2015).
- [141] M. Bashkanov, D. P. Watts, N. Zachariou, E. Chudakov, M. Amarian, J. Ritman, J. Stevens, and I. Strakovsky, Preprint GlueX-doc-3603, 2019.
- [142] J. Grames, private communication, April 2018.
- [143] R. Kazimi, private communication, April 2018.

- [144] D. Androic *et al.* [G0 Collaboration], Nucl. Instrum. Meth. A **646**, 59 (2011).
- [145] We used a modified version of the Pythia package for the GlueX Collaboration at JLab Hall D, <http://home.thep.lu.se/torbjorn/Pythia.html> .
- [146] A. I. Titov and T. S. H. Lee, Phys. Rev. C **67**, 065205 (2003).
- [147] G. McClellan, N. B. Mistry, P. Mostek, H. Ogren, A. Osborne, J. Swartz, R. Talman, and G. Diambrini-Palazzi, Phys. Rev. Lett. **26**, 1593 (1971).
- [148] A. I. Titov and B. Kampfer, Phys. Rev. C **76**, 035202 (2007).
- [149] T. Mibe *et al.* [CLAS Collaboration], Phys. Rev. C **76**, 052202 (2007).
- [150] G. W. Brandenburg *et al.*, Phys. Rev. D **7**, 708 (1973).
- [151] I. Larin, in: *Workshop on Physics with Neutral Kaon Beam at JLab: mini-Proceedings*, arXiv:1604.02141 [hep-ph] (February, 2016), p. 198.
- [152] T. Goorley *et al.*, Nucl. Tech. **180**, 298. (2012); <https://mcnp.lanl.gov/> .
- [153] L. Keller, private communication, 2015.
- [154] J. Allison *et al.*, Nucl. Instrum. Meth. A **835**, 186 (2016).
- [155] ICRP 116 Publication, *Conversion Coefficients for Radiological Protection Quantities for External Radiation Exposures*, Annals of the ICRP, **40**, No 2-5 (2010).
- [156] Y. Qiang, C. Zorn, F. Barbosa, and E. Smith, Nucl. Instrum. Meth. A **698**, 234 (2013).
- [157] E. Pooser *et al.*, Nucl. Instrum. Meth. A **927**, 330 (2019).
- [158] P. Degtiarenko, A. Fass, G. Kharashvili, and A. Somov, Preprint JLAB-TN-11-005, 2011.
- [159] T. D. Beattie *et al.*, Nucl. Instrum. Meth. A **896**, 24 (2018).
- [160] A. Somov, Preprint GlueX-doc-1646, 2011.
- [161] E. Pooser, Ph.D. Thesis, Florida International University (2016).
- [162] C. Keith, in: *Workshop on Physics with Neutral Kaon Beam at JLab: mini-Proceedings*, arXiv:1604.02141 [hep-ph] (February, 2016), p. 223.
- [163] D. Meekins, TGT-CALC-401-007: *Hall D Cryogenic Target: General calculations for relief of the LH₂ target*.
- [164] H. Al Ghouli *et al.* [GlueX Collaboration], AIP Conf. Proc. **1735**, 020001 (2016).
- [165] P. Capiluppi, G. Giacomelli, G. Mandrioli, A. M. Rossi, P. Serra-Lugaresi, and L. Zitelli, IFUB-81-25.
- [166] D. A. Sharov, V. L. Korotkikh, and D. E. Lansky, Eur. Phys. J. A **47**, 109 (2011).

- [167] C. M. Jenkins *et al.*, Phys. Rev. Lett. **51**, 951 (1983).
- [168] D. Cline, J. Penn, and D. D. Reeder, Nucl. Phys. B **22**, 247 (1970).
- [169] P. Bajllon *et al.*, Nucl. Phys. B **134**, 31 (1978).
- [170] A. V. Sarantsev, EPJ Web Conf. **199**, 01009 (2019).
- [171] M. A. Matveev and A. Sarantsev, PoS Hadron **2017**, 069 (2018).
- [172] I. G. Alekseev *et al.* [EPECUR Collaboration], Phys. Rev. C **91**, no. 2, 025205 (2015).
- [173] A. V. Anisovich and A. V. Sarantsev, Phys. Lett. B **413**, 137 (1997).
- [174] J. A. Oller and E. Oset, Nucl. Phys. A **620**, 438 (1997); Erratum: [Nucl. Phys. A **652**, 407 (1999)].
- [175] C. Cawfield *et al.* [CLEO Collaboration], Phys. Rev. D **74**, 031108 (2006).
- [176] R. Delbourgo and M. D. Scadron, Int. J. Mod. Phys. A **13**, 657 (1998).
- [177] M. D. Scadron, F. Kleefeld, G. Rupp, and E. van Beveren, Nucl. Phys. A **724**, 391 (2003).
- [178] Z. Y. Zhou and H. Q. Zheng, Nucl. Phys. A **775**, 212 (2006).
- [179] E. M. Aitala *et al.* [E791 Collaboration], Phys. Rev. Lett. **89**, 121801 (2002).
- [180] J. Z. Bai *et al.* [BES Collaboration], hep-ex/0304001.
- [181] J. H. Friedman and R. R. Ross, Phys. Rev. Lett. **16**, 485 (1966).
- [182] V. Bernard, JHEP **1406**, 082 (2014).
- [183] G. Bonvicini *et al.* [CLEO Collaboration], Phys. Rev. D **78**, 052001 (2008).
- [184] D. V. Bugg, Phys. Lett. B **572**, 1 (2003); Erratum: [Phys. Lett. B **595**, 556 (2004)]; Phys. Rev. D **81**, 014002 (2010).
- [185] J. R. Pelaez and A. Rodas, in preparation.
- [186] R. Bellwied, S. Borsanyi, Z. Fodor, S. D. Katz, and C. Ratti, Phys. Rev. Lett. **111**, 202302 (2013).
- [187] S. Borsanyi *et al.* [Wuppertal-Budapest Collaboration], JHEP **1009**, 073 (2010).
- [188] A. Bazavov *et al.* [HotQCD Collaboration], Phys. Rev. D **90**, 094503 (2014).
- [189] M. Floris, Nucl. Phys. A **931**, 103 (2014).
- [190] L. Adamczyk *et al.* [STAR Collaboration], Phys. Rev. Lett. **112**, 032302 (2014).
- [191] L. Adamczyk *et al.* [STAR Collaboration], Phys. Rev. Lett. **113**, 092301 (2014).

- [192] P. Alba, W. Alberico, R. Bellwied, M. Bluhm, V. Mantovani Sarti, M. Nahrgang, and C. Ratti, Phys. Lett. B **738**, 305 (2014).
- [193] J. Adam *et al.* [ALICE Collaboration], Nature Phys. **13**, 535 (2017).
- [194] R. Dashen, S. K. Ma, and H. J. Bernstein, Phys. Rev. **187**, 345 (1969).
- [195] R. Venugopalan and M. Prakash, Nucl. Phys. A **546**, 718 (1992).
- [196] F. Karsch, K. Redlich, and A. Tawfik, Phys. Lett. B **571**, 67 (2003).
- [197] A. Tawfik, Phys. Rev. D **71**, 054502 (2005).
- [198] R. Hagedorn, Prog. Sci. Culture **1**, 395 (1976).
- [199] S. Capstick and N. Isgur, Phys. Rev. D **34**, 2809 (1986).
- [200] D. Ebert, R. N. Faustov, and V. O. Galkin, Phys. Rev. D **79**, 114029 (2009).
- [201] A. Majumder and B. Muller, Phys. Rev. Lett. **105**, 252002 (2010).
- [202] A. Bazavov *et al.*, Phys. Rev. Lett. **113**, no. 7, 072001 (2014).
- [203] P. Alba *et al.*, Phys. Rev. D **96**, no. 3, 034517 (2017).
- [204] M. M. Giannini and E. Santopinto, Chin. J. Phys. **53**, 020301 (2015).
- [205] C. Amsler *et al.* [Particle Data Group], Phys. Lett. B **667**, 1 (2008).
- [206] E. Santopinto and J. Ferretti, Phys. Rev. C **92**, no. 2, 025202 (2015).
- [207] The Durham HEP Reaction Data Databases (UK) (Durham HepData): <http://durpdg.dur.ac.uk/hepdata/reac.html> .
- [208] M. Albrow, in: *Workshop on Physics with Neutral Kaon Beam at JLab: mini-Proceedings*, arXiv:1604.02141 [hep-ph] (February, 2016), p. 5.
- [209] S. D. Drell and M. Jacob, Phys. Rev. **138**, B1313 (1965).
- [210] H. Osmanović *et al.*, Phys. Rev. C **97**, no. 1, 015207 (2018).
- [211] Y. Wunderlich, A. Švarc, R. L. Workman, L. Tiator, and R. Beck, Phys. Rev. C **96**, no. 6, 065202 (2017).
- [212] A. Švarc, Y. Wunderlich, H. Osmanović, M. Hadžimehmedović, R. Omerović, J. Stahov, V. Kashevarov, K. Nikonov, M. Ostrick, L. Tiator, and R. Workman, Phys. Rev. C **97**, no. 5, 054611 (2018).
- [213] G. Höhler, π N Newslett. **9**, 1 (1993).
- [214] N. G. Kelkar and M. Nowakowski, Phys. Rev. A **78**, 012709 (2008); and references therein.

- [215] G. F. Chew and S. Mandelstam, Phys. Rev. **119**, 467 (1960).
- [216] S. Ceci, J. Stahov, A. Švarc, S. Watson, and B. Zauner, Phys. Rev. D **77**, 116007 (2008).
- [217] A. Švarc, M. Hadžimehmedović, H. Osmanović, J. Stahov, L. Tiator, and R. L. Workman, Phys. Rev. C **88**, no. 3, 035206 (2013).
- [218] A. Švarc, M. Hadžimehmedović, R. Omerović, H. Osmanović, and J. Stahov, Phys. Rev. C **89**, no. 4, 045205 (2014).
- [219] A. Švarc, M. Hadžimehmedović, H. Osmanović, J. Stahov, L. Tiator, and R. L. Workman, Phys. Rev. C **89**, no. 6, 065208 (2014).
- [220] A. Švarc, M. Hadžimehmedović, H. Osmanović, J. Stahov, and R. L. Workman, Phys. Rev. C **91**, no. 1, 015207 (2015).
- [221] A. Švarc, M. Hadžimehmedović, H. Osmanović, J. Stahov, L. Tiator, and R. L. Workman, Phys. Lett. B **755**, 452 (2016).
- [222] M. Hazewinkel: Encyclopaedia of Mathematics (Springer, 31. 8. 1990) Vol.6, pg. 251.
- [223] S. Ciulli and J. Fischer, Nucl. Phys. **24**, 465 (1961).
- [224] I. Ciulli, S. Ciulli, and J. Fisher, Nuovo Cimento **23**, 1129 (1962).
- [225] E. Pietarinen, Nuovo Cim. A **12**, 522 (1972).
- [226] E. Pietarinen, Nucl. Phys. B **107**, 21 (1976).
- [227] R. L. Workman, M. W. Paris, W. J. Briscoe, and I. I. Strakovsky, Phys. Rev. C **86**, 015202 (2012).
- [228] H. Seraydaryan *et al.* [CLAS Collaboration], Phys. Rev. C **89**, no. 5, 055206 (2014).
- [229] J. C. M. Armitage *et al.*, Nucl. Phys. B **123**, 11 (1977).
- [230] Y. Valdau *et al.*, Phys. Rev. C **84**, 055207 (2011).
- [231] P. Adlarson *et al.* [WASA-at-COSY Collaboration], Phys. Lett. B **774**, 599 (2017).
- [232] G. V. Dass and C. D. Froggatt, Nucl. Phys. B **10**, 151 (1969).
- [233] G. V. Dass and C. D. Froggatt, Nucl. Phys. B **19**, 611 (1970).
- [234] F. Schweingruber *et al.*, Phys. Rev. **166**, 1317 (1968).
- [235] S. Toaff *et al.*, Phys. Rev. D **23**, 1500 (1981).
- [236] M. Aderholz *et al.*, Nucl. Phys. B **5**, 567 (1968).
- [237] S. Goldhaber *et al.* Phys. Rev. Lett. **15** 737 (1965).

- [238] A. G. Clark, L. Lyons, and D. Radojicic, Nucl. Phys. B **54**, 432 (1973).
- [239] M. Aguilar-Benitez, R. L. Eisner, and J. B. Kinson, Phys. Rev. D **4**, 2583 (1971).
- [240] R. Engelmann, B. Musgrave, F. Schweingruber, H. Yuta, B. Forman, N. Gelfand, and H. Schulz, Phys. Rev. D **5**, 2162 (1972).
- [241] *Project X Physics Study*, <https://indico.fnal.gov/event/projectxps12>.
- [242] S. D. Holmes *et al.*, arXiv:1306.5022 [physics.acc-ph].
- [243] A. S. Kronfeld *et al.*, arXiv:1306.5009 [hep-ex].
- [244] D. M. Asner *et al.*, arXiv:1306.5024 [physics.acc-ph].
- [245] C. Quigg, private communication, 2015.
- [246] B. Winstein *et al.*, *High precision, high intensity K^0 physics at the main injector*, FNAL LoI 0804, 1988.
- [247] *Summary of the Report from the Working Group for The External Expert Panel on the Radioactive Material Leak Accident at the Hadron Experimental Facility of J-PARC*; http://j-parc.jp/en/topics/HDAccident20130827_02.p
- [248] H. Fujioka *et al.*, arXiv:1706.07916 [nucl-ex].
- [249] H. Noumi *et al.*, *Charmed baryon spectroscopy experiment at J-PARC*, J-PARC Proposal E50, 2012.
- [250] M. Naruki, private communication, 2015.
- [251] K. Abe *et al.* [Belle Collaboration], Phys. Lett. B **524**, 33 (2002).
- [252] T. Lesiak *et al.* [Belle Collaboration], Phys. Lett. B **605**, 237 (2005); Erratum: [Phys. Lett. B **617**, 198 (2005)].
- [253] B. Aubert *et al.* [BaBar Collaboration], Phys. Rev. D **78**, 034008 (2008).
- [254] B. Aubert *et al.* [BaBar Collaboration], Phys. Rev. Lett. **97**, 112001 (2006).
- [255] B. Aubert *et al.* [BaBar Collaboration], Phys. Rev. Lett. **95**, 142003 (2005).
- [256] V. Ziegler, in: *Workshop on Physics with Neutral Kaon Beam at JLab: mini-Proceedings*, arXiv:1604.02141 [hep-ph] (February, 2016), p. 113.
- [257] M. F. M. Lutz *et al.* [PANDA Collaboration], arXiv:0903.3905 [hep-ex].
- [258] J. Ritman, invited talk at *Excited Hyperons in QCD Thermodynamics at Freeze-Out Workshop*, see Ref. [11].
- [259] S. Paul, private communication, 2016.

- [260] C. Adolph *et al.* [COMPASS Collaboration], Phys. Rev. D **95**, no. 3, 032004 (2017).
- [261] J. Goity, P. Huovinen, J. Ritman, and A. Tang, in: *Workshop on Excited Hyperons in QCD Thermodynamics at Freeze-Out: mini-Proceedings*, arXiv:1701.07346 [hep-ph], (November, 2016) p. 158.
- [262] A. W. Steiner, M. Prakash, J. M. Lattimer, and P. J. Ellis, Phys. Rept. **411**, 325 (2005).
- [263] C. J. Horowitz and J. Piekarewicz, Phys. Rev. Lett. **86**, 5647 (2001).
- [264] J. Xu, L. W. Chen, B. A. Li, and H. R. Ma, Astrophys. J. **697**, 1549 (2009).
- [265] A. W. Steiner, J. M. Lattimer, and E. F. Brown, Astrophys. J. **722**, 33 (2010).
- [266] B. G. Todd-Rutel and J. Piekarewicz, Phys. Rev. Lett. **95**, 122501 (2005).
- [267] D. H. Wen, B. A. Li, and L. W. Chen, Phys. Rev. Lett. **103**, 211102 (2009).
- [268] S. J. Pollock and M. C. Welliver, Phys. Lett. B **464**, 177 (1999).
- [269] M. B. Tsang *et al.*, Phys. Rev. C **86**, 015803 (2012).
- [270] K. Hebeler, J. M. Lattimer, C. J. Pethick, and A. Schwenk, Phys. Rev. Lett. **105**, 161102 (2010).
- [271] M. Centelles, X. Roca-Maza, X. Vinas, and M. Warda, Phys. Rev. Lett. **102**, 122502 (2009).
- [272] A. Carbone, G. Colo, A. Bracco, L. G. Cao, P. F. Bortignon, F. Camera, and O. Wieland, Phys. Rev. C **81**, 041301 (2010).
- [273] L. W. Chen, C. M. Ko, B. A. Li, and J. Xu, Phys. Rev. C **82**, 024321 (2010).
- [274] A. Tamii *et al.*, Phys. Rev. Lett. **107**, 062502 (2011).
- [275] B. A. Li, L. W. Chen, and C. M. Ko, Phys. Rept. **464**, 113 (2008).
- [276] M. B. Tsang, Y. Zhang, P. Danielewicz, M. Famiano, Z. Li, W. G. Lynch, and A. W. Steiner, Phys. Rev. Lett. **102**, 122701 (2009).